DETERMINATION OF DENSITY AND MOMENTUM DEPENDENCE OF NUCLEAR SYMMETRY POTENTIALS WITH ASYMMETRIC HEAVY ION REACTIONS

By

Rachel Hodges Showalter

A DISSERTATION

Submitted to
Michigan State University
in partial fulfillment of the requirements
for the degree of

Department of Physics – Doctor of Philosophy

2015

ABSTRACT

DETERMINATION OF DENSITY AND MOMENTUM DEPENDENCE OF NUCLEAR SYMMETRY POTENTIALS WITH ASYMMETRIC HEAVY ION REACTIONS

By

Rachel Hodges Showalter

The nuclear symmetry energy, which is important for asymmetric nuclear systems including rare isotopes and neutron stars, has been studied through both experimental and theoretical approaches, spanning a range of densities from below and above normal nuclear matter density. In the past decade, significant constraints on the density dependence have been obtained in the subsaturation density region, from Heavy Ion Collision (HIC) experiments as well as experiments probing nuclear structure. On the other hand, very little has been determined about the symmetry energy at suprasaturation densities; experimentally, this density region is only accessible in HICs. It is therefore important to understand how to extract nuclear symmetry energy information from HIC at high energies where high density nuclear matter is created in a very brief instant.

Symmetry energy constraints from HICs are determined by comparing experimental observables with those calculated using transport models. The goals of this dissertation are to identify the observables most sensitive to the symmetry energy strength, the effective mass splitting, and the in-medium nucleon-nucleon cross sections, σ_{NN}, at the region just above saturation density which can be created with heavy ion beams available at NSCL. With better constraints in place, the predictive power of transport models will improve. Recent constraints from HIC experiments have relied on symmetric systems, which are predicted to be sensitive to both the density- and the momentum-dependence of the symmetry potentials.

In the study of the nuclear equation of state, asymmetric systems have proven to be more effective at low energy in exploring sensitivities to nucleon-nucleon collisions, which is an important input to any transport model.

In this work, particles that were emitted from Ca+Sn systems, with a ^{48}Ca beam impinging on ^{112}Sn or ^{124}Sn targets are measured. The experimental data were compared to predictions from the Improved Molecular Dynamics model with Skyrme interactions (ImQMD-Sky). Four Skyrme parameter sets were chosen that span current constraints on the density dependence of the symmetry energy and on the nucleon effective mass splitting, $m_n^* \neq m_p^*$, which results from the momentum dependent interaction potentials. ImQMD-Sky calculations were repeated using an alternate form for σ_{NN}.

The yields and ratios of both free and coalescence invariant experimental spectra, constructed as a function of the transverse momentum, were contrasted to those simulated by ImQMD-Sky. To select the overlap region between beam and target nuclei, a mid-rapidity cut was taken in the analysis. The parameter sets included in this analysis did not show a significant sensitivity to the symmetry energy strength, but do suggest that the neutron-to-proton ratio bears a large sensitivity both to the nucleon effective mass splitting and the σ_{NN} forms used in the calculations.

Comparison to the measured coalescence invariant spectra suggests a better agreement with calculations employing effective masses that are greater for neutrons than for protons and a set of isospin-dependent σ_{NN}. The results in this analysis for the asymmetric Ca+Sn reaction are compared with previous results for a symmetric Sn+Sn reaction at 120 AMeV, which shows an opposite conclusion for low energy particles.

For Darin

ACKNOWLEDGMENTS

conversation about sci-fi TV shows. Dan paved the way for my own neutron analysis and in the process taught me many finer details of programming, data organization, and electronics logic. From Mike I learned about how our detectors work, how to maintain our hardware, and how to solder.

As a constant member of the analysis group, Jack Winkelbauer provided an important perspective through every step of this work. There are many times he asked exactly the right question to make me stop and think about my data in a new way. His jokes lightened many days of experimental preparations. I would also like to thank the other members of the HiRA group–Jon Barney, Justin Estee, Juan Manfredi, Sean Sweany and Suwat Tangwancharoen– for the opportunity to refine my ideas. At times each has asked a challenging question that forced me to reexamine my analysis procedures or find new words to better explain scientific principles.

Without our post-docs, very little would be accomplished. I am indebted to Dr. Zibi Chajecki for our many conversations about my experimental data, for his insightful obser- vations, and for his clever solutions to a wide variety of problems from electronics to data presentation. Dr. Bec Shane was forever friendly, approachable, and available. From her I learned many details of both mechanical design and project management. Our many hours of gluing proved her perseverance.

NSCL runs on the work provided by the Mechanical Shop, the Beam Operators and Accelerator Physicists, the Vacuum Team, the Computing Department, the Design Group, and the Facilities Group. I especially want to thank John Yurkon for the use of the Detector Lab, for his advice concerning damaged detectors and the best conductive silver epoxy, and for the uncountable times I have borrowed his equipment.

Our experiment at the Radioactive Isotope Beam Factory in Japan would not have been

successful without the army of help I enjoyed from our local collaborators. The guidance and expertise of Dr. TadaAki Isobe facilitated the entire run. A very special thank you goes to Noritsugu Nakatsuka, who co-led the setup. I could not have navigated my way around the lab without his help. His friendship and advice on Japanese culture during my visit were more help than I could have expected.

Through the physics courses at Michigan State University I relied on my officemate, Dr. Ragnar Stroberg, and my office neighbor, Dr. Jenna Smith. At first we spent hours working mathematics problems on our whiteboard, correcting one another's errors and providing the next step in the calculation. Through time I depended on both for their insights both within physics and outside of it, sharing ideas and jokes as we worked side by side.

Lastly, I could not have accomplished any of this without Darin Showalter's patience and steady support through every obstacle and adventure. He remained a constant through the dynamic, changing years of my graduate career. Thank you.

TABLE OF CONTENTS

LIST OF TABLES

LIST OF FIGURES

xviii

Chapter 1

Introduction

Nuclear physics as a discipline has advanced greatly in the last 100 years, starting with the discovery of atomic nuclei in 1907 by Ernest Rutherford, along with Hans Geiger and Ernest Marsden [6]. Rutherford's original picture of the nucleus was a small, dense collection of positively-charged particles and a smaller number of electrons as required to match the measured value of electric charge. That picture evolved when James Chadwick discovered the neutron in 1932 [7]. The interplay of neutrons and protons composing a nucleus compelled the introduction of the quantum number isospin, I, by Werner Heisenberg in 1932 to explain the similarities between the two particles as two different species of nucleons [8], where the neutron has an isospin projection $I_Z = -\frac{1}{2}$ and the proton has isospin projection $I_Z = +\frac{1}{2}$. In this picture, the nucleons act almost identically under the influence of the strong force. Soon after, Hideki Yukawa formulated a meson to explain the binding of nucleons through the strong force [9]; his description of the binding potential for nuclear matter is known as the Yukawa potential and continues to be used in many theoretical models today.

The original picture of random arrangement of nucleons in nuclear matter changed in the late 1940's into the early 1950's when Maria Goeppert Mayer [10] and J. Hans D. Jensen [11] independently proposed nuclear shell structures to explain the so-called 'magic numbers' observed, where nuclei with 2, 8, 20, 28, 50, 82, and 126 protons or neutrons were observed to be more naturally abundant. When all possible quantum numbers for a particular neutron orbital were occupied, that neutron shell was considered 'filled', and the same was true for

protons in proton shells.

By the 1960's, quarks were proposed by Murray Gell-Mann [12] and George Zweig [13], suggesting that the foundation of nuclear matter is not as simple as it first appeared. The search for these fundamental particles progressed through the emerging field of particle physics, discovering more and more subatomic particles as the Standard Model developed to describe fundamental particles and their interactions. Modern day low-energy nuclear physics, on the other hand, has remained primarily devoted to studying the properties of nuclear matter: nuclear structure and nuclear reactions, as well as discovering new exotic isotopes and studying bound and unbound nuclei at the fringes of stability.

In response to requests from funding agencies for guidance in allocating resources, the US nuclear physics community meets every 5-10 years to agree upon the priorities in their studies. The next Long Range Plan (LRP) is currently being discussed; the last LRP was agreed upon in 2007 with three research areas featured as the most prominent in the community [14]:

1. Quantum Chromodynamics: focusing on interactions of strongly-interacting matter, from quarks and gluons to pions and nucleons, and their relation to the fundamental forces.

2. Nuclei and Nuclear Astrophysics: examining of nuclear forces and nuclear matter, from stable nuclei and rare isotopes to stellar nucleosynthesis and evolution.

3. Fundamental Symmetries and Neutrinos: discovering properties of neutrinos and explaining how the distribution of matter has changed through the evolution of the universe.

This work relates to the second focus of the LRP. Here I examine the effect from excesses of proton or neutron number on the binding energy of nuclear matter. The effect is especially prominent in neutron stars, the hot, dense remnants formed after a supernova event where the neutron excess can reach 90% or more.

1.1 Symmetry Energy

The nuclear liquid drop model, proposed by George Gamow, treats nuclei as incompressible drops of nuclear fluid held together by the strong force. Even though it was already known that nuclei were composed of individual neutrons and protons, the model accurately described experimental results in which the density of nuclei appeared to be relatively constant and the shape of most nuclei appeared to be basically spherical. The liquid drop model also ignores structural effects of nuclei and is most applicable to systems with large nucleon number, A. It can be extended to describe applications of nuclear matter, an idealized collection of infinite nucleons in infinite volume rather than bound in the form of a nucleus, but still modeled well as an incompressible fluid of nucleons.

Leading off from the liquid drop model, Carl Friedrich von Weizsäcker developed the semi-empirical mass formula to describe observed binding energies, E_B, of isotopes with total number of nucleons A, proton number Z, and neutron number N,

$$E_B = a_V A - a_s A^{2/3} - a_C \frac{Z^2}{A^{1/3}} - a_A \frac{(N-Z)^2}{A} + \ldots \tag{1.1}$$

The volume term (a_V) is a constant for binding energy per nucleon and the surface term $\left(-a_S A^{2/3}\right)$ depends only on the total number of nucleons, roughly proportional to the number of nucleons expected to be on the surface of the nucleus. The surface term is analogous to the surface tension in a drop of water. The Coulomb term $\left(-a_C \frac{Z^2}{A^{1/3}}\right)$ describes the repulsion between protons. The remaining term is the symmetry term $\left(-a_A \frac{(N-Z)^2}{A}\right)$, describing the energy cost of an excess in protons or neutrons in the nucleus. This excess in the proton or neutron number, $\frac{N-Z}{A}$, is called the isospin asymmetry, δ. In nuclear matter it is more generally expressed as the difference between the neutron and proton densities (ρ_n

and ρ_p, respectively)

$$\delta = \frac{\rho_n - \rho_p}{\rho_n + \rho_p} \tag{1.2}$$

As in many other branches of science, the physical traits of nuclear matter can be described using state variables, so named because they describe the collective state of a macroscopic system. State variables include pressure, temperature, energy, and density of the system, which can be related to one another in an equation of state (EOS). A common example of an equation of state is the ideal gas law, applicable for a gas that does not have interactions between its constituent particles:

$$PV = nRT \tag{1.3}$$

where the pressure and volume, P and V respectively, of an ideal gas can be related with a constant, R, to the number of molecules in n moles and the system temperature, T. All four variables describe the macroscopic state of the ideal gas.

The nuclear EOS can be written as the energy per nucleon of nuclear matter, $\epsilon = \frac{E_B}{A}$, in terms of density ρ and asymmetry δ

$$\epsilon(\rho, \delta) = \epsilon(\rho, \delta = 0) + S(\rho)\delta^2 + O(\delta^4) \tag{1.4}$$

Here $\epsilon(\rho, \delta = 0)$ are the energy contributions for symmetric matter, and the asymmetry dependence is expressed in terms of the density dependence of the symmetry energy, $S(\rho)$. Comparing to Equation 1.1, one can see that $S(\rho)$ is analogous to the semi-empirical coefficient $-a_A$, but with an explicit density dependence. Some mass formulas include this density dependence by splitting $-a_A$ into a volume asymmetry term, where $\rho \approx \rho_0$, and

a surface asymmetry term, where $\rho < \rho_0$. Equation 1.4 allows for a finer treatment of the density dependence that is smooth with changing ρ. Higher order terms $O(\delta^4)$ are expected to be small. Only even-powered terms are included since it is the difference between the nucleons that pushes the system towards equal densities of protons and neutrons; odd-powered terms would favor systems that are either pure neutron or pure proton matter. The density dependence of the symmetric energy term $\epsilon(\rho, \delta = 0)$ is relatively well-constrained, while the asymmetric term has only been constrained recently at near and below saturation density.

A simple and common parameterization for the density dependence of $S(\rho)$ takes the form

$$S(\rho) = S_{\text{kin}} \left(\frac{\rho}{\rho_0} \right)^{2/3} + S_{\text{int}} \left(\frac{\rho}{\rho_0} \right)^{\gamma} \tag{1.5}$$

where S_{kin} is the Thomas-Fermi kinetic energy and S_{int} is an interaction energy. The kinetic energy depends on the square of the Fermi momentum $(k_F{}^2)$, which can then be reexpressed in terms of the density; for a Fermi gas at zero temperature, in which the lowest available energy states are occupied, this relationship is $k_F{}^3 \propto \rho$. The density dependence of S_{int} is frequently modeled as a power law with factor γ, where the extremes of γ are typically 0.5 and 2.0; this description works well near the saturation density, ρ_0. At subsaturation densities, $\rho < \rho_0$, values of the symmetry energy with $\gamma < 1$ will be larger than those with $\gamma > 1$. The opposite is true at suprasaturation densities. This leads to the nomenclature of 'soft' symmetry energy for $\gamma < 1$, where the strength of the symmetry energy turns over at suprasaturation densities, whereas symmetry energies with $\gamma > 1$ are called 'stiff' and continue to increase with density.

The symmetry energy can play an important role for systems with large asymmetries. Because δ can reach 0.9 or higher in neutron stars, the symmetry energy plays a very impor-

tant factor in governing most of their physical properties, including their radii, maximum masses, cooling rates, and vibrational frequencies [15, 16], as well as possible structures from an inner core to an outer crust and including the possibility of a 'pasta phase' of crystalline arrangement of the nuclear matter located in the inner crust [17, 18]. The symmetry energy also influences the explosion mechanisms of core-collapse supernovae [19]. Because of this, a better constraint on the nuclear EOS is critical for an accurate neutron star model. Similarly, observations of the masses and radii of neutron stars could also improve symmetry energy constraints.

Neutron skins are phenomena particular to heavy nuclei with large excesses of neutrons. In the environment of such a large isospin asymmetry, the energy cost is minimized by locating the 'extra' neutrons on the surface of the nucleus, where the total nuclear density is less and subject to lower strengths of the symmetry energy [20]. Therefore the proton radius could be measurably smaller than the neutron radius for neutron-rich isotopes such as ^{208}Pb and ^{132}Sn [21–23]. An accurate determination of the neutron skins of such neutron-rich nuclei could help to constrain the nuclear EOS, as the difference between the neutron and proton radii is predicted to have a strong relationship to the slope of the symmetry energy, L. This is because it is the relative difference in the symmetry energy strengths between the core of the nucleus at $\rho = \rho_0$ and near the surface of the nucleus at subsaturation density $\rho < \rho_0$, that competes with the increase in surface tension of bringing the excess neutrons to the surface [20]. A stiffer symmetry energy will have a larger increase with density and result in a thicker neutron skin. A measurement of the neutron skin thickness of ^{208}Pb is ongoing at Jefferson Laboratory using polarized electrons to measure the neutron radius.

Many other experimental constraints have been placed at subsaturation densities ($\rho < \rho_0$), with many fewer constraints at suprasaturation densities ($\rho > \rho_0$). Those from $\rho < \rho_0$

include Giant Dipole Resonance (GDR) [24], Pygmy Dipole Resonance (PDR) [25,26], isospin fractionation [27, 28], and more recently from alpha decay [29]. Heavy ion collision (HIC) experiments can also be used to examine many other observables that provide information from the low density region, including isospin diffusion, isoscaling, and particle ratios [30–34]. Pion production in HIC reactions is one of the few observables that examine $\rho > \rho_0$ regions [35].

HIC experiments typically employ systems with large mass that can support systems with both a large and small neutron excess. Reactions of this type include Ca, Sn, Au, or Ni isotopes that have a number of stable isotopes with varying neutron numbers and large natural abundancies; typical experiments with stable beams have a beam intensity of $\sim 10^7$ particles per second and a thick target of ~ 5 mg/cm^2 to minimize statistical errors by increasing the beam-target collision rate. For mid-peripheral collisions at low excitation energy, those that have normalized impact parameters of about 0.5, a low-density neck region forms between the two nuclei, which is one of the best laboratory settings to study matter at subsaturation nuclear density. In central collisions, the two nuclei more quickly compress and subsequently expand to sub-saturation density, leading to earlier emissions of nucleons and small fragments through multifragmentation. The detected nucleons often have higher energies and are less contaminated by secondary decay processes of the residues remaining in the reaction.

1.2   Transport Models

A limiation of HIC experiments is the need to compare to theoretical models. Calculations performed with transport models have enjoyed great success in describing observables such

as differential cross sections [36], isoscaling ratios [37], and elliptic flow [38]. The individual nucleon equations of motion within these models are too complex to be solved directly, so they are treated by simulating the collision of the two nuclei [20].

Typically, the calculation employs a parameterization for the density dependence of the symmetry energy that contains or lies within the current empirical constraints. In addition to the symmetry energy, other factors are at play during the collision, including the Coulomb force, in-medium nucleon-nucleon cross sections (σ_{NN}) that describe how two nucleons interact in a collision, and a momentum dependence of the mean-field potential used to propagate the nucleons; these last two effects will be discussed in greater detail later in this Section.

In the transport models, the beam and target nuclei are each assigned an initial configuration that resembles the ground state of a Thomas-Fermi nucleus and are then propagated through many discrete time steps [36]. At each time step, the phase space of the nucleons is evaluated from Hamilton's equations of motion, including a potential energy term with user input variables. Common options for potential energy terms include a Coulomb term, a Skyrme force term, a Yukawa potential term, and a term describing momentum dependence, all of which are motivated by experimental observations. Because the potentials are felt by every nucleon and are constructed from the relative positions and momenta of every other nucleon, the calculation of the potential can be very intensive. To lower the necessary computing power and allow for a realistic depiction of the interactions, a mean-field potential is constructed at each time step rather than a full set of N-body potentials.

At the end of each time step, after the individual nucleons have been propagated as influenced by the mean-field potential, the transport model checks for any pairs of nucleons that approach within a narrow position window [39,40]. Every identified nucleon pair is then considered for the possibility of a collision, with an interaction probability calculated from

8

in-medium nucleon-nucleon cross sections, σ_{NN}. In many cases, both elastic and inelastic scattering pathways are allowed. Several forms of σ_{NN} are adapted from measurements of free scattering, selected from one of multiple standards in the calculations. As a realistic 'default' setting, a common set of σ_{NN} are used in which the isospin components of σ_{nn} and σ_{pp} (the neutron-neutron and proton-proton interactions, respectively) are identical since both describe isospin-symmetric interactions, but σ_{np} (neutron-proton interaction) differs since it describes an isospin asymmetric collision.

If two nucleons do end within the position window specified, their final states after collision are calculated from σ_{NN} and are typically checked for Pauli-blocking. Some calculations use wavefunctions with explicit antisymmetrization included in their construction as is the case for FMD (Fermionic Molecular Dynamics) and AMD (Antisymmetrized Molecular Dynamics) type models. If the two final states are not forbidden, then the new trajectories and momenta are adopted, otherwise the two nucleons will be treated in the next step as if a collision did not occur [41].

From there, the mean-field potential is calculated from the new positions and momenta of all nucleons and the process repeats until the end time defined by the user, which is generally long enough for the beam and target nuclei to separate once again and the desired observables to become stable. As described in Section 4.2, the effects of the momentum dependence in the mean-field potentials can be simplified in the calculations by introducing an effective mass, m^*. In this simplification, the nucleons propagate through the mean-field as if their mass were smaller; typically $m^*/m \approx 0.7$ is used. In principle, neutrons and protons, as different species of nucleons, could feel different effects from the momentum-dependent mean-fields. This phenomenon is represented as having different effective masses. It is therefore possible that $m_n^* < m_p^*$ or that $m_n^* > m_p^*$ depending on the form of the

potentials used. In this work we attempt to constrain the sign and magnitude of the nucleon effective masses with empirical data.

Because the transport models are quite complex, they require a number of inputs that can be varied by the user. Generally speaking, the calculations are run with a set of standard values that have been determined from previous comparisons to data.

To make for the best comparisons and to control the number of variables at play, only a few inputs are varied from one set of calculations to another to gain physics insights. In this case, the majority of terms relating to the dynamics of the nuclei, the propagation of the nucleons, and the defined collision window are held constant, while a select few parameters are varied to examine physics variables of interest. In this analysis, a localized Skyrme interaction is used because it has successfully described both the reaction dynamics in HICs as well as nuclear structure effects. Even these inputs are not chosen 'at random' by the user, but are selected from a variety of standard sets. In the Improved Quantum Molecular Dynamics (ImQMD-Sky) calculations used in this work, four distinct parameter sets are used to examine the effects of the symmetry energy strength and the effects of the mean-field potential on the nucleons. The four sets span the current constraints created by past experiments, including the value of the symmetry energy coefficient S_0 and the effective mass m^*/m, and yield similar descriptions of other observables, including ground-state properties of nuclei like the incompressibility K_0 [1].

Many transport models have enjoyed a great success in modeling systems. The Particle and Heavy Ion Transport code System (PHITS) is a Monte-Carlo transport code developed by the Japan Atomic Energy Agency (JAEA), in collaboration with the Research Organization for Information Science and Technology (RIST) and the High Energy Accelerator Research Organization (KEK) in Japan, to model the transport of all particles including

nucleons, nuclei, mesons, photons, and electrons over a wide range of energies [42]. PHITS has been applied to a wide range of applications, from accelerator design and cosmic ray research to medical and radiation protection [43].

Another example of a very successful transport model is that used in this work to calculate the neutron detection efficiency, SCINFUL-QMD, which was also developed at JAEA. SCINFUL-QMD models the light output of the organic scintillating material NE-213 used in the neutron detectors for this experiment. First the model calculates the transport of neutrons with specified kinetic energy from a source to the scintillating material, then their transport within the material. For a reaction probability that can be chosen from several different models for different cases, a light output is produced in the code to match experimental data of deexcitations by charged particles. Options are also available for the user to include or to exclude signatures of charged particles that do not stop in the scintillating material, to better align with experimental setup and analysis, or the method of conversion from particle kinetic energy to light output. Further details can be found in Section 3.2.3.4. SCINFUL-QMD has successfully modeled the light response to neutrons with kinetic energies ranging from 10 MeV$<E_{kin}<$80 MeV and 150 MeV$<E_{kin}<$1 GeV [44].

However, both PHITS and SCINFUL-QMD are not suitable to examine the physics insights of the different variables as the programs are not developed for such a purpose. Instead, models are used that were developed by theorists who are actively studying symmetry energy. In the ImQMD-Sky model used in this work, the uncertainties of the constraints on the slope of the symmetry energy and the effects of the mean-field potentials could be improved further; the current constraints were obtained from recent comparisons of Sn+Sn reactions at incident energy of 50 AMeV. Observables calculated from these differing parameter sets can be compared to observables constructed from experimental data in an attempt to select the

11

best set of parameters and thereby improve the transport model. This is exactly the process used in the current attempt to constrain the density dependence of the symmetry energy, the effects of the mean-field potential, and the form of the in-medium nucleon-nucleon cross sections [20, 45]. Additionally, transport model calculations have played a critical role in predicting systems and observables that should demonstrate a sensitivity to the parameters used. In this way, the comparison between experimental data and calculations is often an iterative process. Observations of nuclear collisions can help to constrain model parameters and in turn transport models calculations can help predict experimental observables or reaction systems that should demonstrate sensitivity to the model parameters used.

To make the best comparison between the experimental data and the calculations, many analysis cuts are shared. The impact parameters of the nucleus-nucleus collisions are selected to be comparable. In this analysis, both central and mid-peripheral reactions were examined. Peripheral reactions were not studied, since the physics of these collisions probe different questions than the ones at the heart of this analysis. Likewise, analysis cuts were taken to select the overlap region of the two colliding nuclei. This allows for an examination of symmetry energy effects at subsaturation density, where soft symmetry energy parameterizations have larger values of the symmetry energy strength than stiff parameterizations. Because asymmetric systems are examined, this overlap region is also predicted to be sensitive to the momentum-dependent effects of mean-field potentials and the forms of σ_{NN} used. Thus by constructing observables as discussed in the next Section, and comparing to the values predicted by transport model calculations, an improvement on the constraints on key input parameters can be attempted.

1.3 Experimental Observables

Under the influence of the symmetry energy in Equation 1.4, an asymmetric system will evolve towards a minimum energy configuration, in the direction of $\delta = 0$. For a neutron-rich system, that means we would expect to see an increased emission of neutron-rich matter from the neutron-rich collision with high beam energy. If the symmetry energy strength is larger, the relative increase in emission of neutrons or neutron-rich particles would likewise increase, because the symmetry energy increases with the square of the asymmetry, $E_{sym} = S(\rho)\delta^2$. This is true for all densities of nuclear matter.

This phenomenon motivates the construction of ratios of neutron to proton spectra, called n/p ratios, as an observable to probe the strength of the symmetry energy.

$$R(n/p) = \frac{Y(n)}{Y(p)} \tag{1.6}$$

where Y(x) is the differential yield of that nucleon from a single beam-target combination and a shared region of phase space. One expects that both nucleon types will be ejected from a collision, so constructing a ratio of the two should enhance the effect of symmetry energy, which has potentials of opposite sign for protons and neutrons, unlike other isoscalar strong potentials. However systematic effects, such as errors in the detection efficiencies or the Coulomb potential felt by protons but not neutrons, can influence just one part of the n/p ratio and would not be cancelled.

Recent work from comparisons of calculations with experimental Sn+Sn data [1] [2] show a comparative lack of sensitivity in $R(n/p)$ to the symmetry energy for symmetric reactions. However, both studies do demonstrate a larger sensitivity in n/p ratios to the nucleon effective mass, discussed in more detail in Section 4.2. The system examined in this

work, Ca+Sn, is asymmetric and may show a different sensitivity in the n/p ratios compared to that observed in the symmetric reactions studied.

Additionally, asymmetric reactions are predicted to be very sensitive to the form of σ_{NN} used in the model calculations. Asymmetric reactions like the Ca+Sn reactions examined here can have very different N/Z ratios in the beam and target nuclei, leading to a sensitivity in the observables to the relative differences of σ_{nn} and σ_{pp} compared to σ_{np}. The number of p-n collisions differ between the ^{48}Ca+^{124}Sn and ^{48}Ca+^{112}Sn reactions while the number of target protons remains constant, allowing for a "subtraction" of reactions with target protons, leading to a strong sensitivity to the reactions with target neutrons. Predictions for ^{40}Ca+^{100}Zn suggest a strong sensitivity in the calculations to the σ_{NN} forms used [46]. This is in contrast to symmetric systems, which have shown little sensitivity to the cross sections.

Single-particle ratios, also called isoscaling ratios, can be constructed to examine the relative emission of a single nucleon between two different beam-target combinations. For a nucleon x, the isoscaling ratio is

$$R_{21}(x) = \frac{Y_2(x)}{Y_1(x)} \tag{1.7}$$

for two reactions 1 and 2, which have different N/Z compositions and should therefore have different contributions from the symmetry energy. By convention, reaction 2 is chosen to be the more neutron-rich reaction. Like $R(n/p)$, systematic effects may persist in the isoscaling ratios, especially analytic errors made in one reaction but not the other. An example of one such reaction effect is the spectral normalization by total event number, which remains a constant within a single beam-target combination.

Finally, the double n/p ratio, $DR(n/p)$, can be constructed

$$DR(n/p) = \frac{R_2(n/p)}{R_1(n/p)} = \left(\frac{Y_2(n)}{Y_2(p)}\right)\left(\frac{Y_1(p)}{Y_1(n)}\right) = \frac{R_{21}(n)}{R_{21}(p)} \tag{1.8}$$

which is used to cancel multiple sources of errors or uncertainties that may remain in either $R(n/p)$ or $R_{21}(x)$. Since $DR(n/p)$ uses two different particle spectra that are compared between two beam-target combinations with differing values of N/Z, we expect to see a sensitivity to the symmetry energy but with larger statistical error bars.

For neutron-rich HICs, one would expect $R(n/p){>}1$, $R_{21}(n){>}1$, $DR(n/p){>}1$ and $R_{21}(p){<}1$. Generally, a greater enhanced emission of particles from one system corresponds to a larger symmetry energy strength. With the help of the models, the magnitude of the ratios can help constrain the strength of the symmetry energy.

In this work, I examine emission of neutrons and protons from two HIC reactions: ^{48}Ca+^{124}Sn and ^{48}Ca+^{112}Sn. The ^{48}Ca beam had a kinetic energy of 140 AMeV for both reactions. As the two reactions have different values of isospin asymmetry δ, comparing the nucleon spectra between the two reactions should be correlated to the strength of the symmetry energy and the momentum dependence of the symmetry potentials.

1.4 Organization of Dissertation

This dissertation will be organized as follows. The experimental setup will be presented in Chapter 2 along with detailed descriptions of the detectors. Chapter 3 will focus on the calibrations performed on the detector systems and the determinations of various efficiencies applied to the data. The calculations obtained in the ImQMD-Sky transport model will be

shown and summarized in Chapter 4. The experimental data obtained from the analysis will be displayed in Chapter 5 and compared to the ImQMD-Sky calculations. Finally, Chapter 6 will summarize the findings and present the future outlook for this area of nuclear physics.

Chapter 2

Experimental Setup

2.1 Introduction

There were five detector systems used in this experiment, each with a distinct function and a unique analysis procedure. The detectors were either positioned inside or around the S2 thin-walled scattering chamber in the configuration seen in Figure 2.1. In the diagram, the beam enters the chamber from the lower right to impinge on the target at the center. The beam used in this experiment was a primary ^{48}Ca beam with kinetic energy of 140 AMeV. Two targets were used, ^{112}Sn and ^{124}Sn, with thicknesses of 4.98 mg/cm^2 and 5.41 mg/cm^2 respectively, for a total of two possible Ca-Sn reactions.

Wrapped around the target was the Miniball (MB) Array, described in Section 2.2, a 4π detector used to determine the centrality of each reaction event. Downstream of the target, to beam right, were the LASSA telescopes, described in Section 2.7, which were used to measure the positions and energies of emitted charged particles. Also downstream of the target, a ring of CsI detectors called the Forward Array (FA) was placed to mark the start time from fast, light emitted charged particles, described in Section 2.4. The FA was not a complete ring so as to avoid shadowing the LASSA detectors.

At the far side of the experimental vault at beam left, two walls of scintillating material, called the Neutron Wall Array (NW Array), were erected to measure neutrons. The NW Array is further discussed in Section 2.3. Finally, a set of thin scintillator paddles were
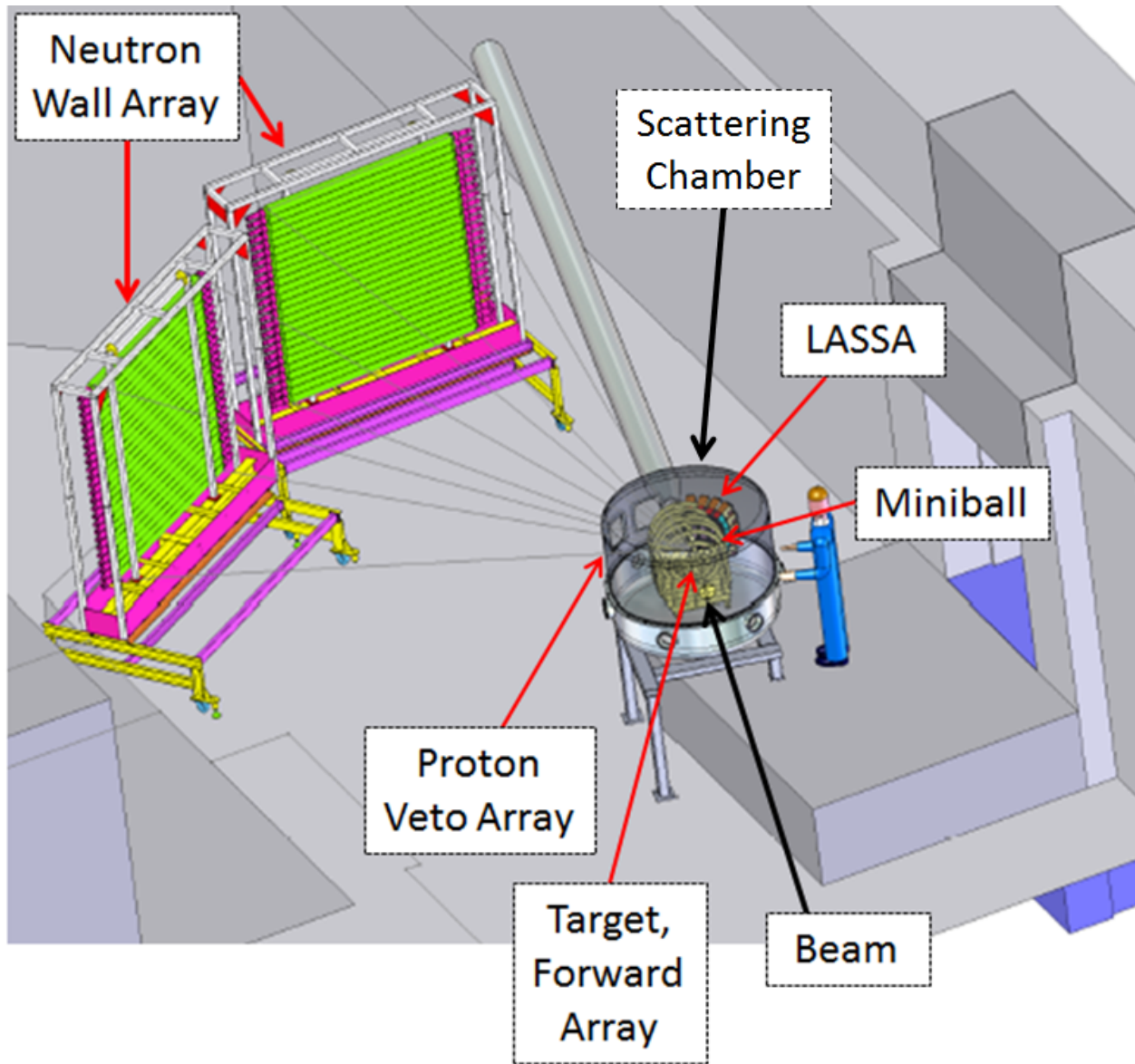
Figure 2.1: Schematic of the detectors in the experiment. The beam enters the scattering chamber from the bottom right. A person (in blue) is included in the schematic to provide a sense of scale. See the text for a full description of detector placement and purpose.
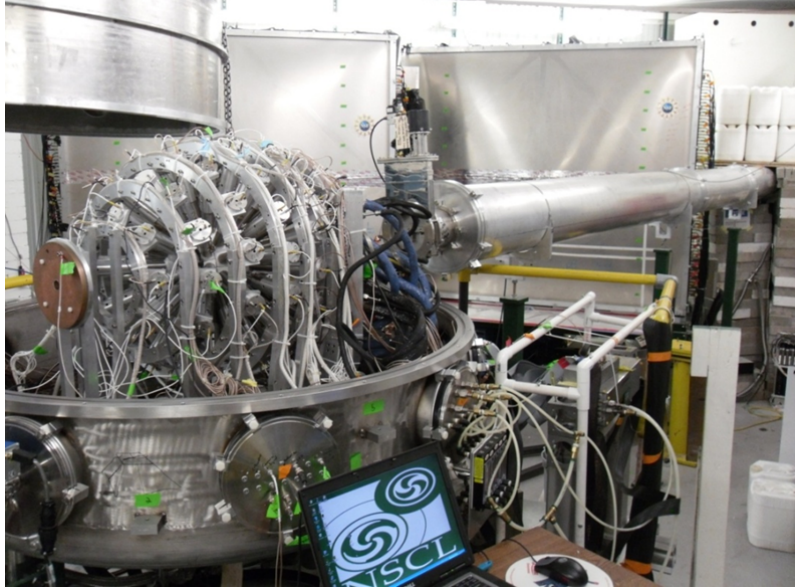
Figure 2.2: A photo of the experimental setup just prior to data taking. The Miniball Array dominates the foreground; the beam would enter the array through the copper beamstop on the left and exit through the beampipe to the right. The two neutron walls are visible in the background of the image.

placed on the outside of the chamber in an arrangement to shadow the Neutron Wall Array behind it, as described in Section 2.5. Called the Proton Veto Array (PV Array), the paddles detected emitted charged particles so that their counts could be subtracted from the NW Array spectra. The emitted neutrons were analyzed by combining the information from the FA, PV Array, and NW Array. A photo of the experimental setup just prior to data-taking is shown in Figure 2.2.

2.2 Miniball

The Miniball Array in its full configuration is a set of 188 telescopes all pointing at a central point reserved for the target location. Together, the telescopes can cover about 89% of the solid angle around the target, with very forward and very backward angles open for the beam to enter and exit the array without interfering with the detectors. The configuration used

Table 2.1: A summary of the detectors used in the Miniball Array, organized by ring. The columns list the number of telescopes used in each ring (out of the full complement), the fractional solid angle covered, the polar and azimuthal angle spans, and the distance from the target to the front face of each crystal.

Ring	Detector	$\Delta\Omega$ (msr)	θ (deg)	$\Delta\theta$ (deg)	$\Delta\phi$ (deg)	d (mm)
5	15(24)	30.8	45	10	15	140
6	14(20)	64.8	57.5	15	18	90
7	19(20)	74.0	72.5	15	18	90
8	16(18)	113.3	90	20	20	70
9	13(14)	135.1	110	20	25.7	70
10	11(12)	128.3	130	20	30	70
11	8(8)	125.7	150	20	45	70

for this experiment utilized detectors from the back half of the array, a total of 96 telescopes placed at polar angles from 40° to 160°. The front faces of the detectors were from 7 to 14 cm away from the target. The telescopes used are summarized in Table 2.1. Two detectors were removed from Ring 8 to allow for the target support rod. To avoid shadowing the NW Array, 6 detectors were removed from Ring 5 from azimuthal angles 232.5° to 322.5° and 3 telescopes were removed from Ring 6 from azimuthal angles 241° to 297°. To avoid shadowing the LASSA telescopes, 3 telescopes were removed from Ring 5 from azimuthal angles 67.5° to 112.5° and 3 telescopes were removed from Ring 6 from 63° to 117°. A photo of the backward half of the Miniball Array is shown in Figure 2.3; rings 9-11 are shown.

Each telescope in the Miniball Array comprises a fast plastic scintillator in front, a 40 μm piece of Bicron BC-498X plastic scintillator spun in-house, backed by a 2 cm thick CsI(Tl) crystal. Every CsI crystal is attached to a C83062E PMT (photomultiplier tube) using two pieces of UVT Plexiglas. The thin scintillator was covered with aluminized mylar foil to protect the detector assembly and to keep it light tight. A 5 mg/cm^2 Sn-Pb foil was used to suppress electrons. The combined information from the fast plastic and the CsI crystal can be used for particle identification (PID). The fast plastic scintillator has a decay time

20
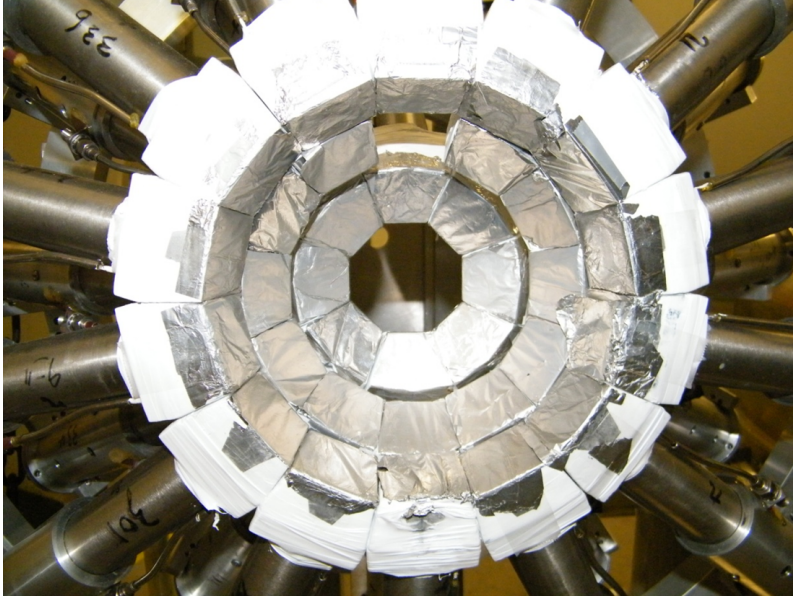
Figure 2.3: The backward rings of the Miniball Array. The beam enters from the center of the ring.

of 2.4 ns and the CsI(Tl) has two major decays on the order of hundreds of ns and a few μs [2]; the resulting signals are labeled as fast, slow, and tail energy signals, respectively. By comparing each of these signals, elemental (up to Z=18) of detected particles is possible as well as isotopic identification for hydrogen and helium particles. In this experiment, only the "fast" signal from the fast plastic scintillator was used to construct the multiplicity in the Miniball. Further details on the multiplicity calculation are discussed in Section 3.1.

2.2.1   Miniball Electronics

The Miniball provided one of the triggers for most of the experiment. Because we were interested more in collecting information from central collisions, data resulting from peripheral events were avoided by requiring a multiplicity of at least four hits within the MB Array. The multiplicity outputs of all Miniball discriminators were set to provide a linear signal with an amplitude of 50 mV; these outputs were summed linearly. Then a discriminator on

Figure 2.4: Electronics diagram for the Miniball subsystem [2,3].
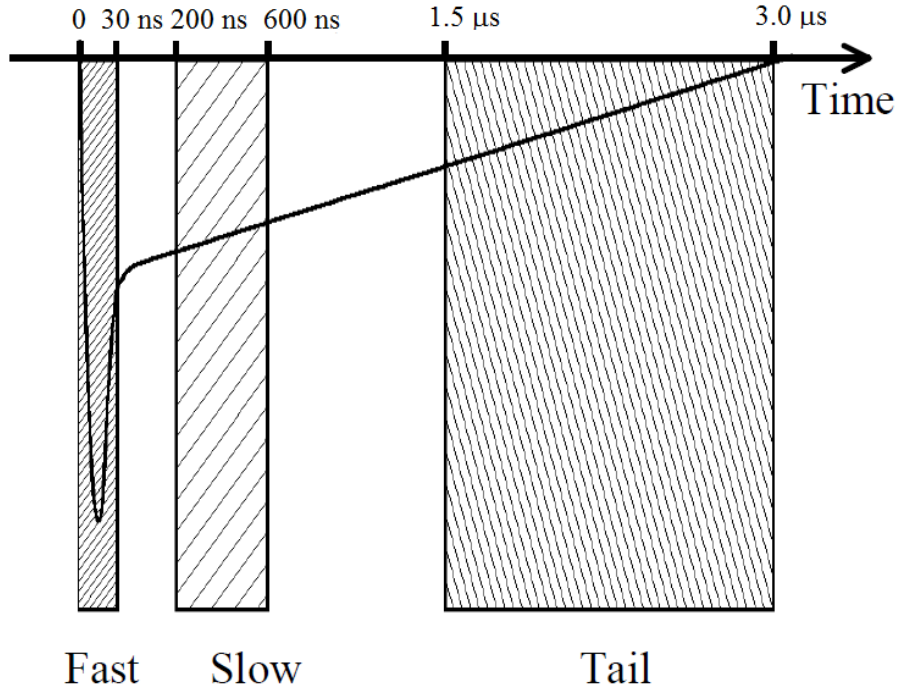
Figure 2.5: Diagram of a MB pulse as split by the timing gates and integrated to form the three pulse height signals.

the multiplicity sum pulse the system was set to trigger at a voltage greater than 200 mV, which corresponded to a minimum MB Array multiplicity of four.

The full layout of the Miniball electronics is shown in Figure 2.4. The signals from the PMTs were sent to specially designed Miniball splitter modules. In the case of Rings 8, 9, 10, and 11, the signals were amplified before being sent to the splitter modules. The splitter passively splits the signals into outputs with different amplitudes: fast, slow, or tail, as labeled in Figure 2.5. The portions of the energy signal were integrated with lengths of 30 ns for the fast, 400 ns for the slow, and 1.5 μs for the tail, which allows for the integrated charge to be roughly the same for all three signals. A fourth output is sent to a Phillips 7106 discriminator to provide the timing of the signal.

The Miniball subsystem busy is 1.5 μs long, to prevent retriggering while the QDC (Charge-to-Digital Converter) shapes and integrates the energy signals, and is set to fast

clear if no master trigger is received within 500 ns. Because of the length of time required, the MB subsystem triggers itself and forms part of the basis of the master trigger, further discussed in Section 2.8.

2.3   Neutron Wall Array

The neutrons were detected in the Neutron Wall Array (NW Array), comprising 2 walls of 25 long scintillator bars each. A schematic of one wall is shown in Figure 2.6. Each Pyrex glass bar measures 2m in length, 7.62 cm in height, and 6.35 cm in depth [5], and is filled with NE-213, a liquid scintillator material produced by NE America [5]. The Pyrex cell wall is 3mm thick and additional space is allowed for the stainless-steel support structure, giving the total spacing between bars of 8.6 cm and an inactive area of 11% . The total height of each wall is 2m, for a total area of 2m x 2m per wall. The walls were placed approximately 5m and 6m away from the target, with the center of the walls at polar angles 19° and 48° from the beam direction. The full angular coverage in the lab frame is shown in 2.7. Both arrays were mounted on aluminum frames and covered with aluminum plates painted black on the inside to make each wall light-tight [5]; in this way the bars did not have to be made light-tight individually. Additionally, black strips of paper were laid between each cell to prevent cross-talk between bars [5]. The front and back aluminum plates are only 0.8 mm thick, so they should not be a significant source of neutron scattering [5].

The liquid scintillator detects neutrons when they collide with a nucleus of the scintillating material and impart some fraction of their kinetic energy. The impacted nucleus then recoils and deposits that same amount of energy into the detector, by exciting the scintillating material. The S_1 state of the NE-213 is populated first. From there, the material can either
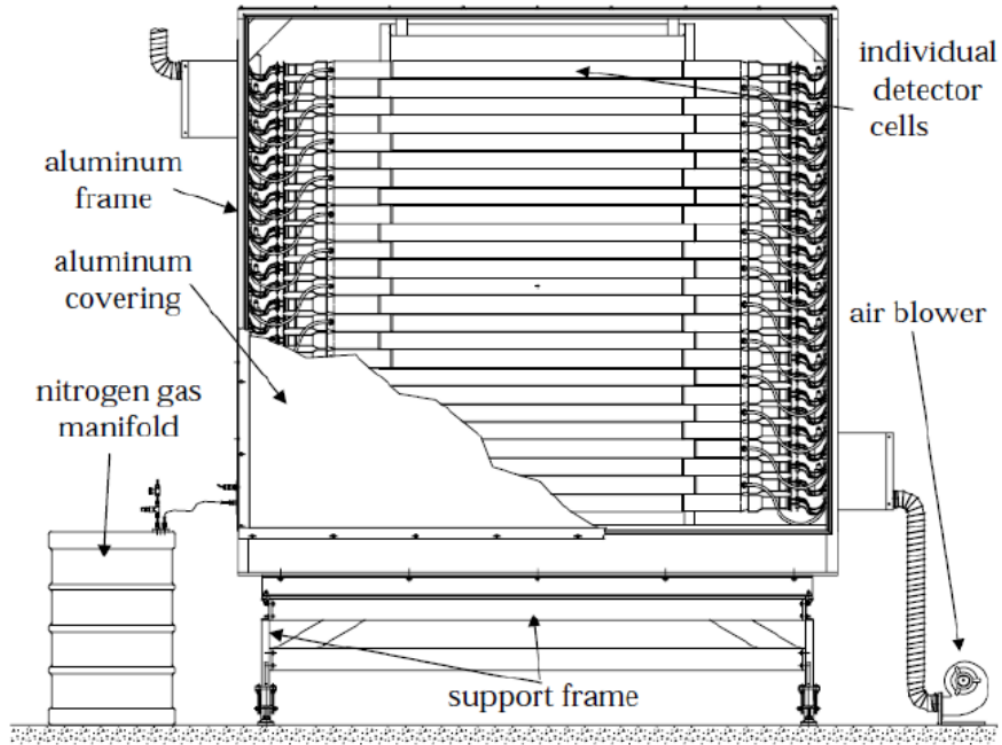
Figure 2.6: A schematic of the inside of one wall in the NW Array [4].
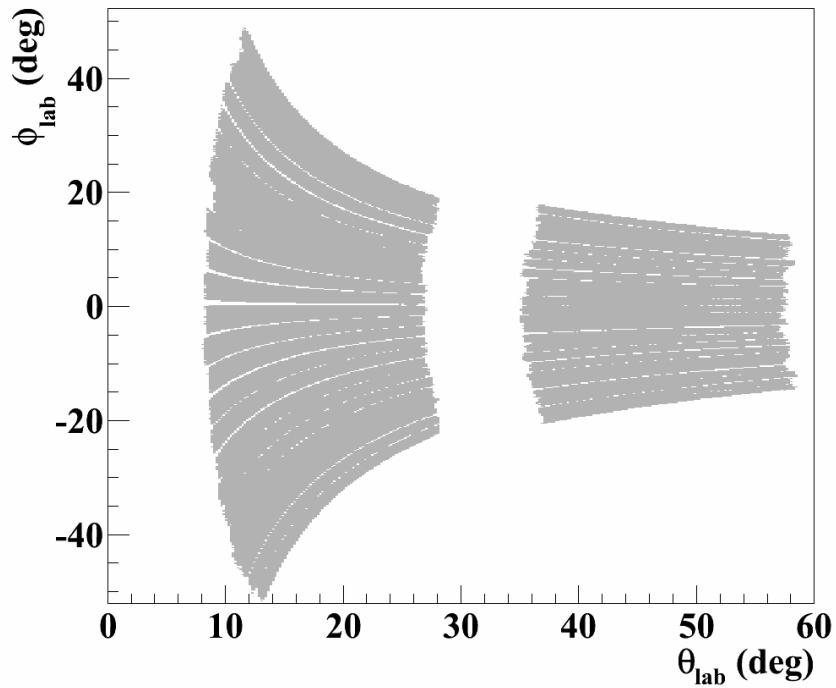
Figure 2.7: The angular coverage of the NW Array in this experiment.

deexcite through prompt fluorescence with a decay time of 32 ns, or it can transition to the T_1 excited state and undergo phosphorescence with a decay time of 230 ns. Either the fluorescent or phosphorescent processes release the energy in the form of light.

A Phillips Photonics model XP4312B/04 PMT is located at each end of the bar to detect the light produced. The Pyrex cells are not treated with a reflective coating, so the scintillated light can only reach the ends of the bar due to total internal reflection [5]. In a Monte Carlo simulation, it was found that 20% of the light generated from a neutron hit reaches each PMT, while 60% of the light escapes the cell [5]. Because the neutron deposits a fraction of its kinetic energy into the scintillating material, and only a fraction of the deposited energy is converted to scintillation light, we cannot directly convert the pulse height of the PMT signal to the neutron kinetic energy; instead we rely on the measured neutron time-of-flight (TOF) to determine the velocity of the particle and therefore its energy. The NW Array sets the end time in the TOF, the start time is provided by the Forward Array, which measures charged particle times in coincidence with the neutron; this time measurement is discussed further in Section 3.2.1.1.

The NW Array has time resolution of about 1 ns, as evidenced by the width of the prompt gamma peak seen at the beginning of the NW time spectrum in Figure 2.8. The time resolution depends on a few factors, the most important of which are the rise time of the light pulse produced by the scintillating material, the time resolution of the electronics, and the intensity of the scintillated light [5]. Because most photons reach the PMTs by scattering off the cell walls, there is an inherent uncertainty in the flight path which affects the uncertainty in the start time of the pulse [5]. The time resolution also depends on the thickness of the cell, as a thicker cell translates to worsened time resolution but gains increased neutron detection efficiency since there is more NE-213 material for a potential

26
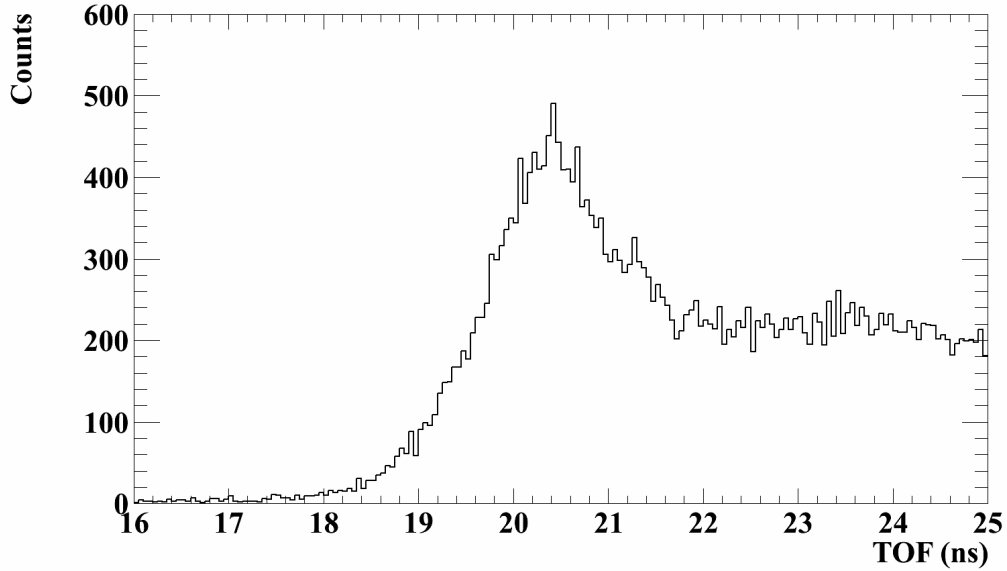
Figure 2.8: The prompt gamma peak at the beginning of the NW timing spectrum determines the timing resolution.

interaction [5].

The position resolution on the bar is 7.65 cm, roughly the same as the bar height. The hit position on the bar was determined as the time difference between the two PMTs [5]. The total light output of the bar was measured as the geometric mean of both integrated PMT signals.

The NW Array was chosen not only for its excellent time resolution and dynamic energy range, but also for its ability to discriminate particles based on the shape of the pulse produced. Just as neutrons can interact with the scintillating material and create light, gammas that pass through the scintillating material can also cause the cascade of scintillating material detectable by the PMTs. These background gammas introduce a continuous background that is not removable in the TOF method used to determine the neutron energy [5]. NE-213 has a useful property not found in the more common solid scintillator: gammas and neutrons produce signals with different pulse shapes. This property is commonly called pulse shape

27
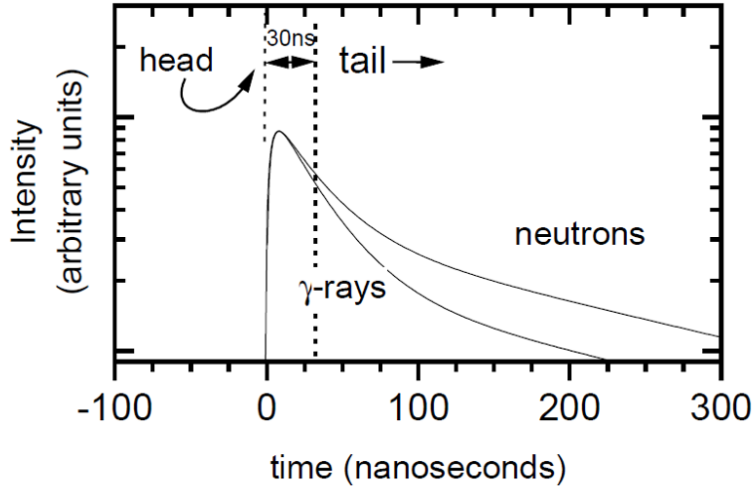
Figure 2.9: Pulse shapes for neutrons and gammas incident on a Neutron Wall Bar, normalized so that the initial pulse height is the same [5]. The integral of first 30 ns of the pulse is called the fast signal, the full integral is the total signal.

discrimination (PSD). In general, neutrons have a large total signal compared to gammas with the same initial pulse height, as seen in Figure 2.9. This is caused by a much faster decay time for reactions with gammas, which lightly ionize the scintillating material to primarily undergo fluorescent decays through the S_{10} excited state with a characteristic decay time of 32.3 ns. On the other hand, proton recoil events from neutron scattering reactions are more heavily ionizing and therefore have a large component of phosphorescent decay through the T_{10} state, with a longer lifetime of 270 ns. Therefore, by comparing the integrated signal from an initial 30 ns time window, called the "fast" signal, to the total integrated signal in the two PMTs, we can discriminate between gammas and neutrons. An example of this comparison is shown in Figure 2.10.

Because the NW Array does not have precise position resolution, especially position tracking or angle of incidence information, we cannot discriminate between neutrons that travel directly to the NW Array or those that arrive after scattering off of other materials. These scattered neutrons contribute to the background of detected particles. In order to
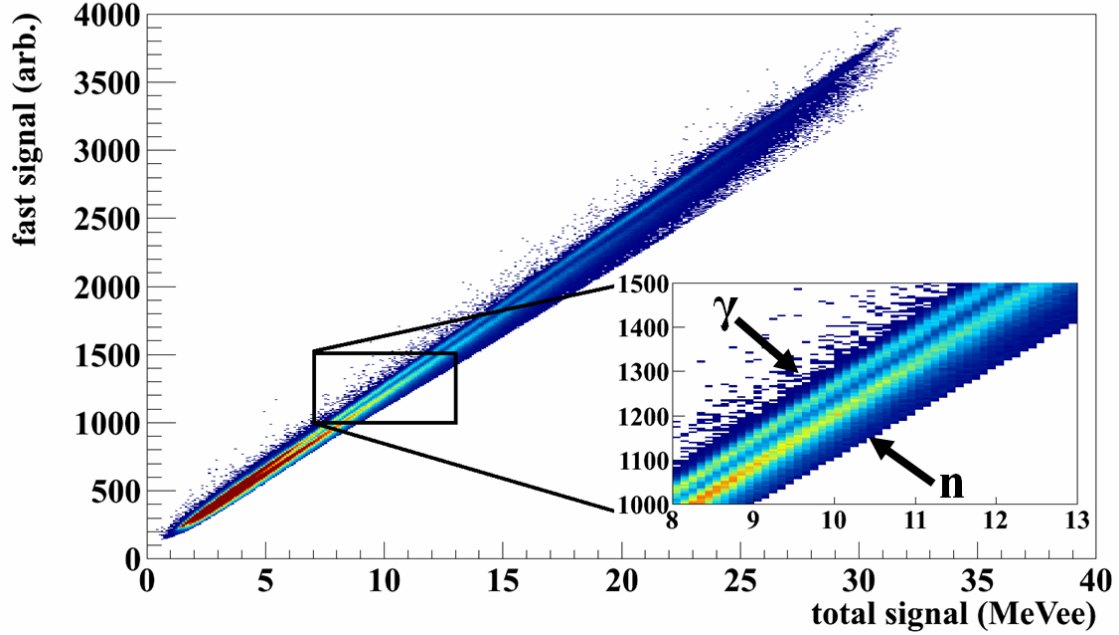
Figure 2.10: Pulse shape discrimination for the NW Array is constructed by comparing the fast signal to the total signal. The inset shows a zoomed in view of the middle section of the PSD.

determine the proportion of scattered particles, a mount was constructed to hold 30 cm thick brass bars called shadowbars between the target and the NW Array, with five potential shadowbar locations per wall. The shadowbars are thick enough to prevent neutrons emitted from the reaction of interest from being transmitted to the NW locations directly behind them, so the only neutrons detected in one of those locations must have been scattered into it. These bars were set in one of four configurations throughout the experiment in front of both wall. One of the positions is shown in Figure 2.11 in front of the forward wall. As viewed from the target, the four positions were: upper left and lower right corners, upper right and lower left corners, center positions, or completely removed. The information from each of these shadowbar locations was used to determine the contribution of the scattered background to the neutron spectra across position and TOF information.

Figure 2.11: Brass shadowbars placed in one of four position configurations used during the experiment. One neutron wall is immediately behind the shadowbar mount. The outgoing beampipe is seen on the right of the photo.

2.3.1 Neutron Wall Electronics

The dynode signal from the PMT was processed through a CFD (constant fraction discriminator) to get the timing signal from the event and to start the NW subsystem shown as the schematic in Figure 2.12.

In order to achieve the signals needed for the NW Array PSD, the anode signal from the PMT was resistively split into two outputs with different attenuation. In addition, a signal from the last dynode was sent to an inverting fast amplifier then to a LeCroy CFD. The total charge of the anode signal was integrated in a common gated QDC; all the discriminator signals corresponding to the total charge signals for the various channels in a single QDC were ORed together to make the logic condition for the start of the common gate with the output broadened to a 340 ns width so as to overlap them. Similarly, the "fast" signal was

Figure 2.12: Electronics diagram for NW Array subsystem [2, 3].

integrated in individual gated QDCs (IGQDCs); each channel of the IGQDC was gated by the corresponding logic signal from the dynode being generated in the individual discriminator. These discriminator outputs were broadened to make a 60 ns gate and timed to select the first 30 ns of the charge; the charge in the first 30 ns becomes the fast signal.

For this setup, 3 common gated QDCs were used. The gates for the three QDCs were ORed together to form the NW submaster signal. Logically, this was equivalent to an overall OR of all NW phototubes. The common gates could be vetoed by a local self veto, to prevent refiring during digitization, or by a global busy, which kept the NW subsystem from processing data when another subsystem was busy or while the DAQ (data acquisition) was collecting data. A fast clear was used, because the charge integration process needed to start before the global master trigger could arrive, so the NW subsystem needed to be able to clear the data from its modules if the global master was not received within a certain time window. Because the TDC (Time-to-Digital Converter) stores information in a buffer, it can read out events that were stored earlier than the trigger's time of arrival, so the TDC does not need to be fast cleared.

2.4 Forward Array

The purpose of the Forward Array (FA) is to provide a start time for the NW Array wall timing information. It consisted of 16 NE-110 scintillators centered around the beam axis in a ring formation with an inner diameter of 1.0" and an outer diameter of 4.5". The FA was located 10 cm downstream of the target to cover enough of the forward solid angle to obtain a high enough multiplicity in the FA so that the start time from fast emitted particles is reasonably precise. A 72° slice was removed at beam right to avoid shadowing the LASSA
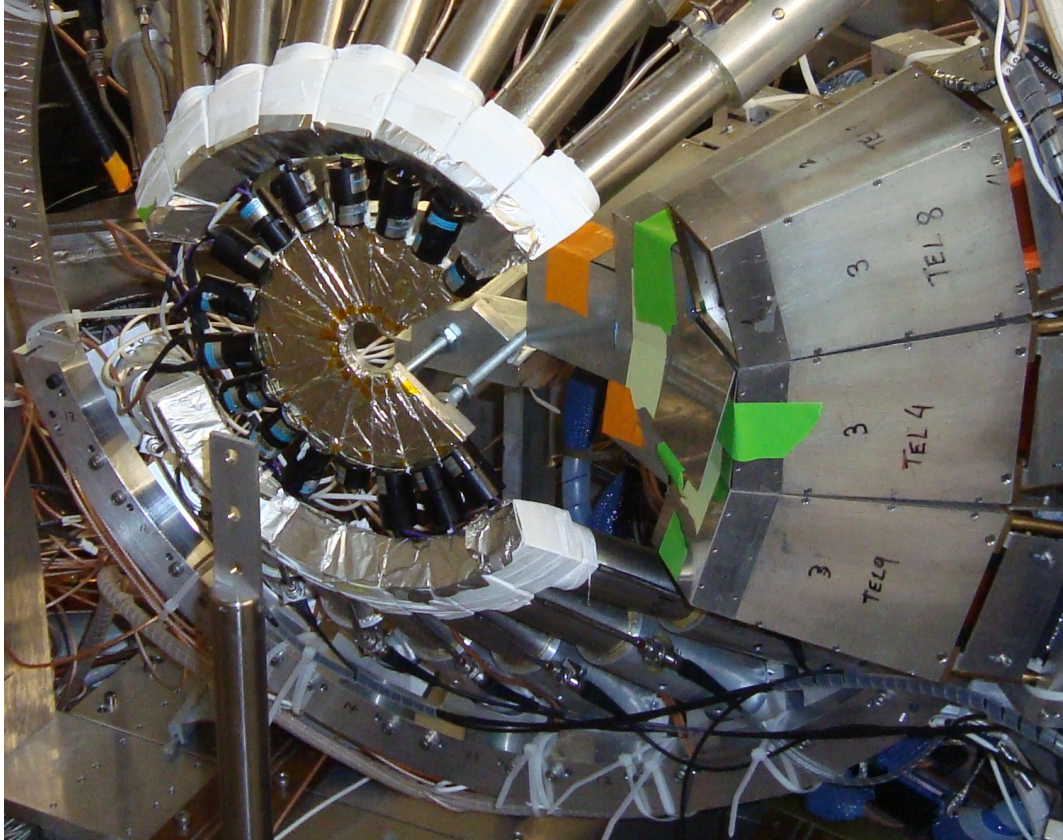
Figure 2.13: Photo of the detectors located forward of the target, which would be placed on the cylindrical rod at the foreground of the picture. The detectors wrapped in white are Ring 5 of the Miniball. The FA is in the very center of the photo. To the right are the six LASSA telescopes.

telescopes. A photo of the FA is shown in Figure 2.13.

Hamamatsu R5600U PMTs were attached to the FA crystals along the outer diameter of the ring by optical epoxy. A E5780 base was used with each PMT. Each crystal wedge was painted with Bicron BC-620 reflective paint to improve transmission of scintillated light and wrapped in aluminized mylar to prevent external light contamination and cross-talk between FA elements. The wedges were mounted to an aluminum plate of the same dimensions, with the aluminum plate downstream of the scintillators. No detectors were shadowed by the FA elements, the PMTs, or the aluminum support.

FA subsystem
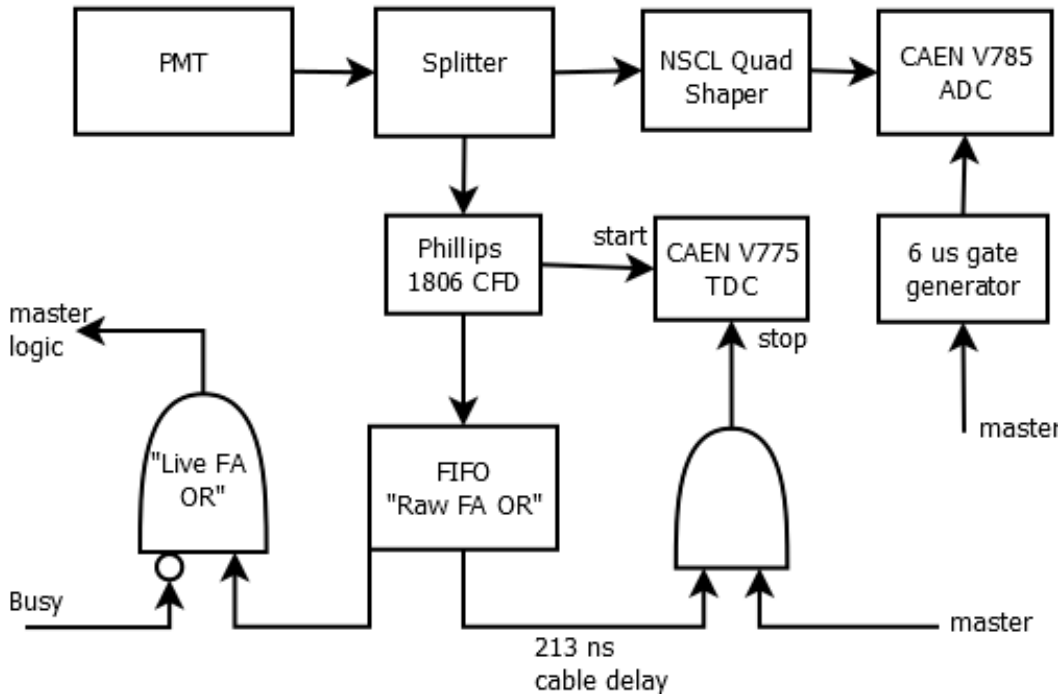
Figure 2.14: Electronics diagram for the FA subsystem [2, 3].

2.4.1 Forward Array Electronics

A diagram of the FA subcircuit is shown in Figure 2.14. The FA signals were split into time signals and pulse height signals; the times were sent to the TDC and the pulse heights were shaped and sent to the ADC (Analog-to-Digital Converter).

The FA time was the start time for the entire system: the TDC for the FA was therefore self-timing and could be set to a common stop from the FA time OR. This subsystem was enabled by the master and therefore did not require a fast clear circuit and was relatively simple. Because the FA time served as a reference time for the entire experimental setup, the FA OR was sent to the NW and Miniball TDCs as a time reference.

34

2.5   Proton Veto Array

As neutrons can interact with the scintillating material in the Neutron Wall (NW) Array, so too can the charged particles produced from the reaction. Charged particles have a higher detection efficiency in NE-213 than neutrons, since they can interact with the scintillating material via the Coulomb force as well as through elastic collisions. Because hydrogen atoms ionize the scintillating material to a similar degree as neutron-hydrogen collisions in NE-213, it is not possible to discriminate between hydrogens and neutrons in the PSD analysis (similarly, interactions of helium atoms with the scintillating material ionize to the same degree as neutron-carbon collisions in NE-213). It is therefore very difficult to remove charged particle signals from the neutron spectra in the NW Array. To help aid this endeavor, we constructed an array of thin plastic scintillator paddles called the Proton Veto (PV) Array. We used a set of 10 paddles, each made of 3/8" thick Bicron BC-408 coupled to a UVT light guide and a PMT. The area of each PV paddle was 16 cm by 16 cm. All paddles were polished to maximize the amount of light transmitted and wrapped in black plastic to prevent outside light contamination and optical cross-talk between paddles. The PV Array was mounted on the outside of the experimental chamber as shown in Figure 2.15 in a configuration to shadow the NW Array. Four PV paddles shadowed the forward wall located 6 m away from polar angles 8° to 30° and six PV paddles shadowed the backward wall 5 m away from polar angles 35° to 60°. Because the backward wall was located closer to the target, it subtended a larger portion of the solid angle, and therefore more paddles were needed to fully shadow the region.

Ideally, any charged particle that hit the NW Array would first pass through the PV Array and its energy would be registered on at least one of the paddles. The empirical
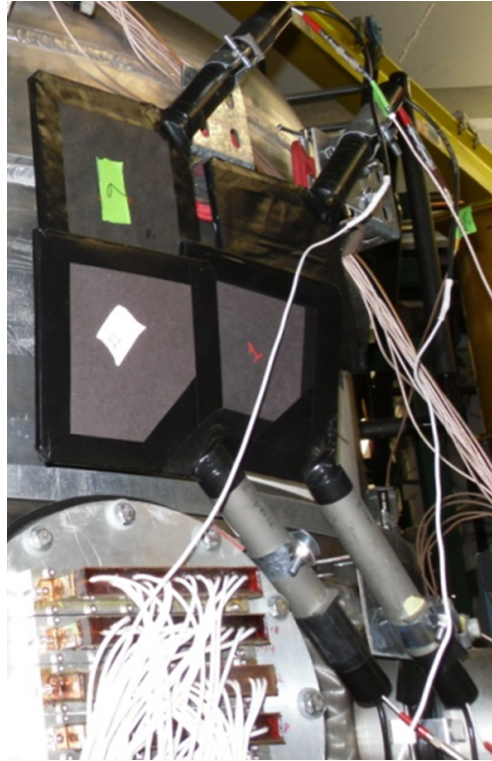
Figure 2.15: Four of the ten PV paddles used in this experiment. These were mounted to the outside of the chamber wall.
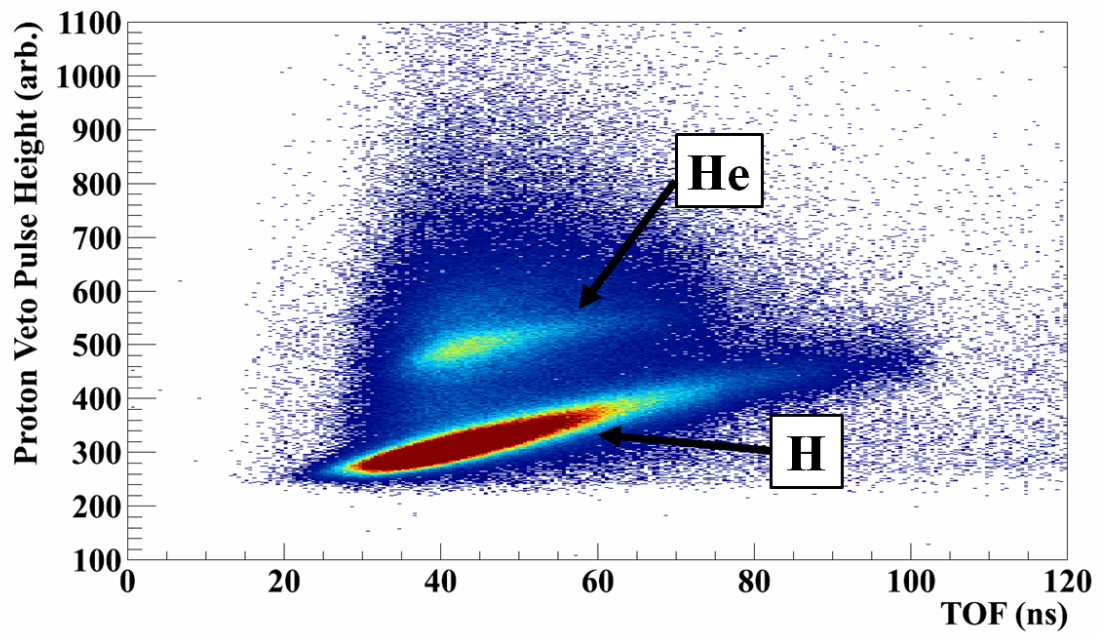
Figure 2.16: Hydrogen and helium particle identification bands in the PV Array. The hydrogen PID band lies at lower pulse heights.

PV subsystem
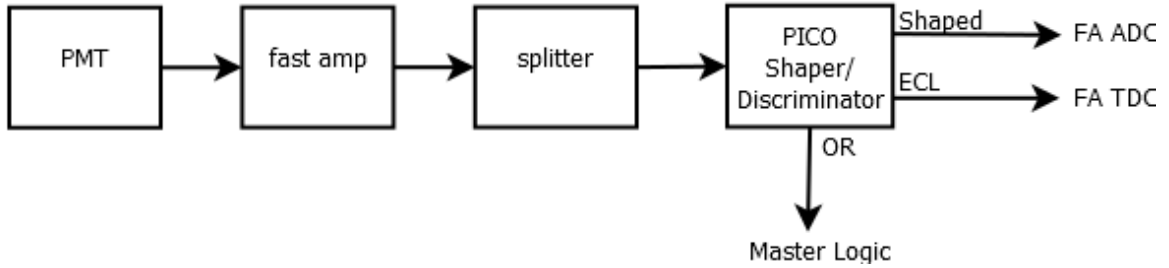
Figure 2.17: Electronics diagram for the PV Array subsystem [2,3].

detection efficiency for hydrogen and helium particles was approximately 80%-90% in the PV Array, as discussed in Section 3.2.3.1, while neutrons are very unlikely to be detected. To further improve the discriminatory abilities of the PV Array between charged particles and neutrons or gammas, hits were identified within particle identification (PID) bands constructed by comparing the pulse height of the PV paddle against the TOF to the NW Array. Hydrogen and helium atoms each lie within a distinctive band seen in Figure 2.16. In order to achieve sharp PID lines in the PV Array, the light output for each paddle was scaled based on the distance of the hit from the PMT base as determined from the NW Array location.

2.5.1   Proton Veto Electronics

The PV time and pulse height signals were sent to the same TDC and ADC as the FA signals. Therefore the signal processing is very similar to that found in Section 2.4.1. The subsystem is depicted in Figure 2.17.

2.6 Neutron Wall Particle Identification

The PV Array was used to identify only charged particle hits. For this to be the case, two conditions had to be met. First, the PV hit was required to fall in either the hydrogen or helium band in the PV PID spectra constructed by comparing the PV pulse height against NW TOF, after the electronic cross-talk was removed from the PV spectra. Second, the position of the NW hit had to be located in the region shadowed by the corresponding PV paddle. If both conditions were met, then the NW hit was tagged as either a hydrogen or a helium, depending on the PV Array PID band. The remaining NW hits were either neutrons or gamma events and could be distinguished by PSD.

Because of the low segmentation of the PV Array, there were many events for which a PV hit corresponded to more than one NW hit in the shadowed region, in which case it could not be uniquely determined which NW hit corresponded to the charged particle and all hits in the event were removed for ambiguity. Due to the relatively low multiplicities seen in both the NW Array and the PV Array, the ambiguity in particle matching resulted in removing only about 10% of particles in the forward wall and about 3% of particles in the backward wall.

2.7 Large Area Silicon Strip Detector Array (LASSA)

The LASSA array was designed for the detection of light charged particles with very high position and energy resolution. Each LASSA telescope comprises a double-sided silicon strip detector (DSSD) backed by four thallium-doped cesium iodide crystals (CsI(Tl)). The DSSD is 500 μm thick and has 16 Si strips on each side; a photo of one DSSD is shown in Figure 2.18. The front strips are arranged vertically as seen from the target and the back strips are
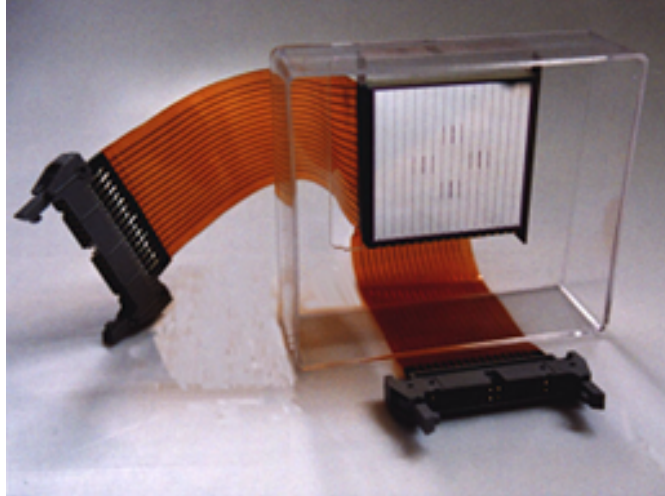
Figure 2.18: A LASSA DSSD.

arranged horizontally, forming 256 pixels on the face of each telescope. Each strip is 3 mm wide with a gap of 100 μm between. At the distance of 20 cm from the target, a single pixel can provide an angular position resolution of 0.89°. The 20 cm target distance is chosen by the design of the CsI crystals, which are tapered so the front of the crystal is narrower than the back, thus subtending the same fractional coverage throughout the crystal length when placed 20 cm from the target.

The CsI crystals are 6 cm in length, with 2.5 cm x 2.5 cm area at the front and 3.5 cm x 3.5 cm area at the back, that covers a quadrant of the Si detector in front. A cartoon depicting the arrangement of the DSSD and CsI crystals is shown in Figure 2.19. CsI(Tl) was chosen because it is a relatively inexpensive scintillation material, and can be machined into a variety of shapes as necessary for the experimental application. Each CsI crystal is connected to a light guide and then to a photodiode, which is read out by the LASSA electronics discussed in Section 2.7.1.

The 6 cm crystal length corresponds to a proton punchthrough energy of 147 MeV, meaning that protons with energy less than 147 MeV will be stopped by the material and
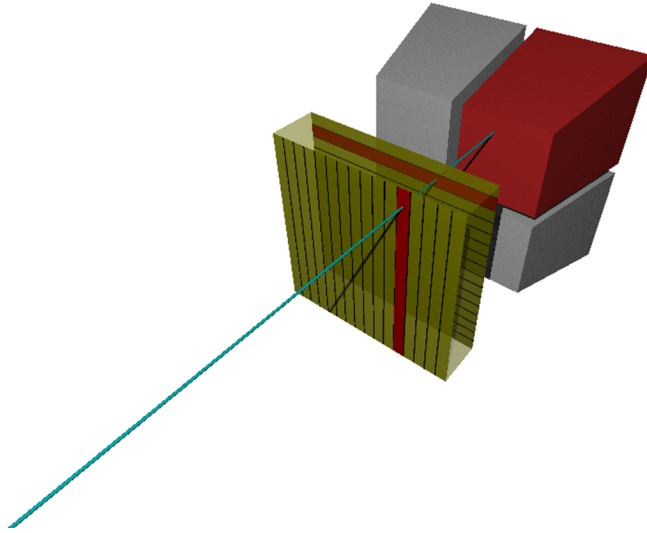
Figure 2.19: A cartoon of the silicon dE detector in front of the CsI E detector that comprise a LASSA telescope. The image shows a pixel hit, formed by both sides of the silicon detector.

deposit their full kinetic energy, while protons with larger energies will not be stopped in the material and will deposit only some fraction of their kinetic energy. Thus, only protons with measured energies up to 147 MeV can be analyzed using the LASSA telescopes.

The LASSA telescopes contain several layers of materials that cause the charged particles to lose energy. Each CsI crystal is wrapped with aluminized mylar on the front and inner sides to prevent light from escaping from the crystal without detection, either from the front of the crystal or between neighboring crystals. The front of the DSSD also has a Si dead layer which does not measure energy. Finally, a 0.018 mm thick SnPbSb foil (39% Sn, 60% Pb, 1% Sb) was placed in front of the detector to protect it from electrons. These layers contribute to energy losses in detected particles that must be accounted for in the analysis.

In this experiment, six LASSA telescopes were used and were arranged in a configuration to approximate the angular coverage of the NW Array. A photo of the setup is shown in Figure 2.13, with the LASSA telescopes on the right side of the photograph. Together the six telescopes covered a range in the lab frame from polar angle 8° to 55° and azimuthal
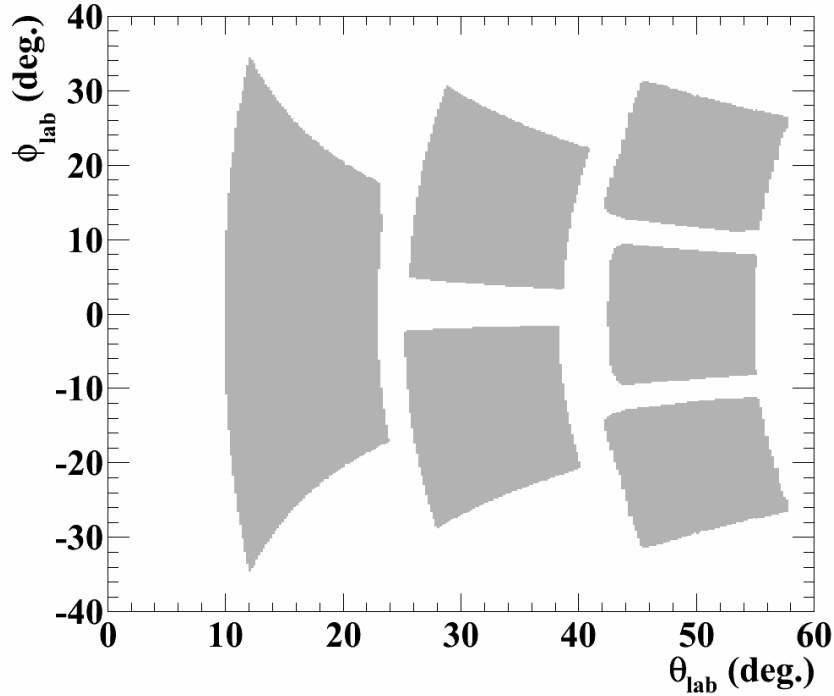
Figure 2.20: The angular coverage of the LASSA telescopes in this experiment.

angle -35° to 35°, as shown in Figure 2.20.

Particle identification (PID) in the LASSA telescopes follows the dE-E method. The particle energy deposited in the DSSD provides the dE while the CsI crystal measures the E. When the signals are compared, curved bands are formed as seen in Figure 2.21. The relationship of energy loss in the DSSD to the energy remaining in the CsI for a particle with charge Z and energy E follows the Bethe formula:

$$-\frac{dE}{dx} = \frac{4\pi}{m_e c^2} \frac{nZ^2}{\beta^2} \left(\frac{e^2}{4\pi\epsilon_0}\right)^2 \left(\ln\left(\frac{2m_e c^2 \beta^2}{I(1-\beta^2)}\right) - \beta^2\right) \tag{2.1}$$

where n is the electron number density and I is the excitation potential. The PID cannot be uniquely determined for particles that do not stop in the CsI, so these events are removed in the analysis.
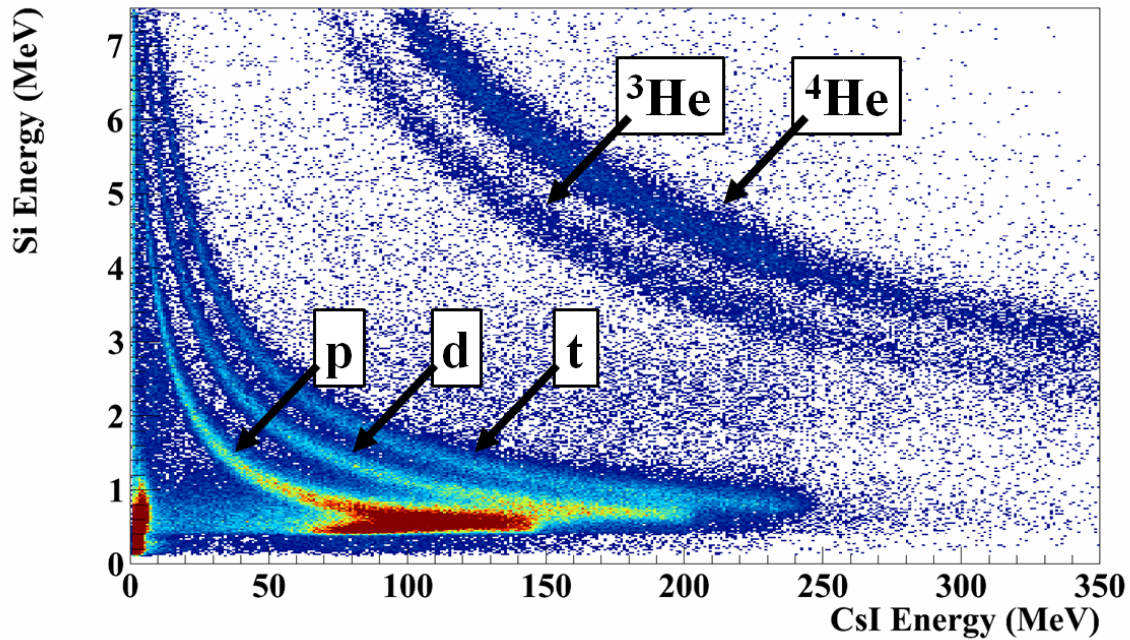
Figure 2.21: An example PID plot from LASSA. The lowest band are protons, followed by deuterons and tritons. Partial helium bands are seen in the upper right of the plot.

2.7.1 LASSA Electronics

The signals from the Si and the CsI detectors are read separately. The CsI subsystem, shown as a schematic in Figure 2.22, was relatively simple because it has few channels and the times are not digitized. The light produced in an event is collected in a photodiode and amplified in the preamps contained within the telescope. The signals are then split into two paths to determine the time and energy of the hit: the time signal creates a raw OR that is passed to the master logic while the energy signal is shaped and digitized in an ADC. The processing in the ADC is started by the master trigger.

The Si subsystem uses ASIC electronics because they can treat the many individual Si channels in a compact, cost-effective manner. A schematic of the ASIC subsystem is shown in Figure 2.23. The Si signals from the LASSA telescopes were processed in a HINP16C
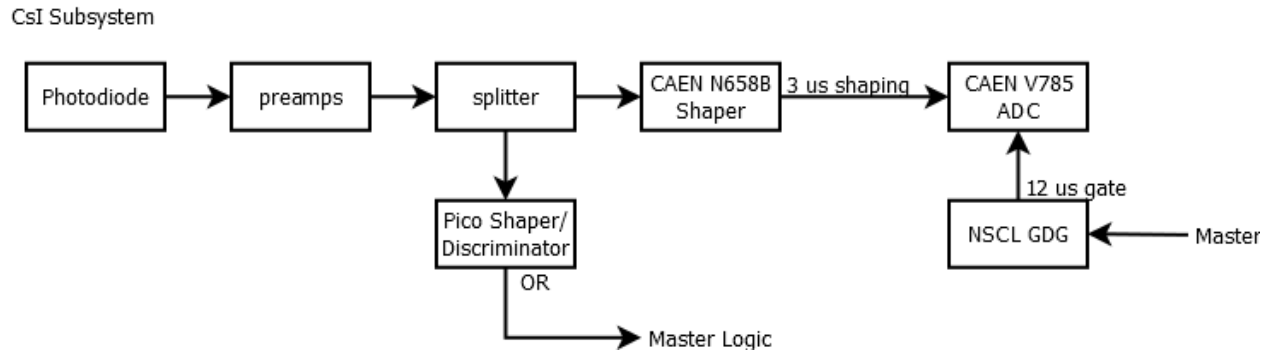
Figure 2.22: Electronics diagram for CsI subsystem [2,3].
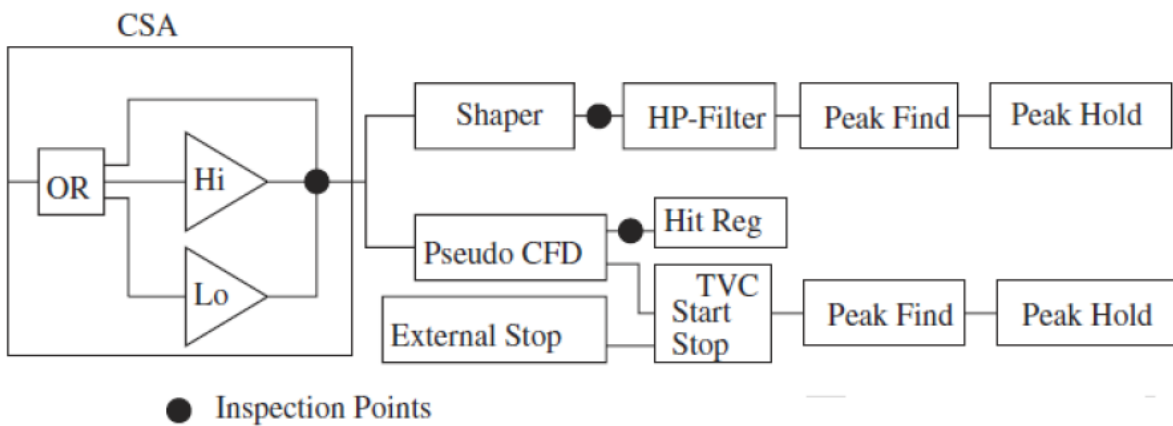
Figure 2.23: Electronics diagram for ASIC logic used to process the Si signals [2].

chip [47] which was developed to use with the Si of the HiRA telescopes, a very similar array of Si-CsI telescopes. Each Si strip is treated individually rather than within a group of channels.

First the signal from the Si detector is processed through a charge sensitive amplifier (CSA), which has two internal gain stages, though we elected to use external pre-amplifiers in their place. The amplified signal is then split. One split signal is then processed by a Nowlin psuedo constant fraction discriminator (CFD), to determine if that particular strip has a hit, and then by a time-to-voltage converter (TVC). The second signal is shaped within about 1 μs. Both the time and energy signals are stored for data readout. As with other fast cleared subsystems, if a trigger is not received within the set time window the data is cleared to allow for the next hit to be processed, but if a trigger is received, the data is read out.

One advantage of the Si electronics is the inclusion of the inspection points seen as the black circles in Figure 2.23. The signals can be monitored remotely and the settings for individual channels changed, for example to adjust the thresholds online during data-taking. Another gain to using the ASIC electronics is that channels that are noisy on either the detector end or the electronics end will not hang up the entire system, as long as the Si strips are not included in the trigger. Unfortunately, the dead time cannot be measured through scaler information, so it is difficult to determine the Si detector efficiency. This is discussed further in Section 3.3.3.2.

Also included on the chipboard are the electronics that distribute the bias voltage to the Si strips and a logic unit that controls the logic on the chip. The chipboards are powered by a motherboard, which can hold up to 16 chipboards, though only six chipboards were used for this experiment. The motherboard also contains a field programmable gate array

(FPGA) that serves as the point of communication between the chips and the data acquisition system. The motherboard has two linear outputs which send the recorded energy and time information from the ASIC channels to a SIS3301 flash ADC. A JTEC XLM module serves as the point of communication between the Si subsystem and the master logic, accepting the master trigger, telling the computer when the Si data is ready to be read out, and storing the address of the channel that was just read.

2.8 Electronics Summary

For standard data runs, the master trigger was set to coincidence between the FA and MB submasters, with all other systems run as a slave. The FA subsystem was required to get timing information for each event. The MB subsystem required a minimum charged particle multiplicity to reduce peripheral events, which are not of interest for the analysis. In principle, anything included in the dashed box in Figure 2.24 could be included as part of the trigger. Some calibration runs were acquired using special triggers to get the desired information.

The submaster trigger had an output with a 20 μs time length that was sent to all subsystems to avoid retriggering the system during data processing. The master begins the latch, which starts the computer busy signal. Data was read in through the NSCL DAQ system. When the DAQ finished reading an event, a signal from an I/O module clears the computer busy latch and signals that it is ready to read the next event.

Master Logic

NW Live OR | FA Live OR | MB live submaster | Si OR | CsI Raw OR | PV Live OR

GDG "FA Wide"

GDG "MB Wide"

GDG "MB Really Wide"

GDG "delayed CsI"

350 ns gate   300 ns gate   5 us gate   130 ns delay

Busy

FA + MB

CsI Live OR

LASSA + !MB

Master OR

subsystems

busy

subsystem self-vetos

start

GDG "master"

GDG "resolving time delay"

Lecroy 222 latch "comp busy"

GDG "digitization delay"

20 us gate

subsystems

stop

comp trig

20 us delay start

LASSA XLM clear

comp ready

CAEN V262 VME I/O

acq. ack.

Lecroy 222 latch "trigger latch"

stop

Figure 2.24: Electronics diagram for the Master trigger [2,3].

46

Chapter 3

Analysis

All analysis processes described here have three important phases. The first is calibration: correlating the signal received in the electronics channels to a physics observable such as time, energy, or position. Next, some selection is applied to determine which events are physically interesting: which ones can be correlated to the theory calculations. Finally, corrections are applied to account for detector efficiencies, geometric coverage, and other factors that limit particle detection. Of primary interest for this analysis is to extract proton and neutron energies and transverse momenta.

3.1   Miniball Analysis

The data from the Miniball was used to calculate the charged particle multiplicity for each event, which was then correlated to the centrality of the reaction. First, the charged particle multiplicity (N_c) was counted as the total number of particles detected in the Miniball array above the hardware threshold. For most of the Miniball elements the fast signal was used, as this was the most reliable signal throughout the experiment. In two cases, the fast signal was not read in properly so the time signal for those elements was used instead.

The charged particle multiplicity can be related to the reaction cross section σ

$$\sigma(N_c) = \frac{I_r(N_c)}{I_i N} \tag{3.1}$$

where $I_r(N_c)$ is the current of charged particles produced in the reaction with at least that value of N_c, I_i is the incident current of beam particles, and N is the density of target atoms per unit surface area. The relation is best calculated for minimum-bias runs, triggered off of the Miniball array only, with the other detector systems not recording any data. If a geometric cross section is assumed, it can be used to calculate the impact parameter, b.

$$\sigma(N_c) = \pi b^2 \tag{3.2}$$

In this relationship, smaller values of N_c are correlated to larger cross sections and therefore larger impact parameters corresponding to peripheral collisions. Similarly, larger values of N_c are correlated to smaller cross sections and smaller impact parameters which correspond to central collisions. In order to calculate an absolute value for the impact parameter, a precise determination of the beam current is required; despite attempting to measure the beam current through multiple methods, a precise determination was not achieved for this experimental data, so only the relative impact parameter can be calculated. We write this as $\hat{b}$ to indicate that all impact parameters are written as a fraction of the largest impact parameter measured for a particular beam-target combination

$$\hat{b} = \frac{b(N_c)}{b(N_{min})} \tag{3.3}$$

For this experiment, the data acquisition was triggered off a minimum multiplicity of 4 in the combined Miniball and Forward Array system. Therefore we use the impact parameter corresponding to $b(N_c = 4)$ as $b(N_{min})$. The distributions of $\hat{b}(N_c)$ vs N_c for both the $^{48}\text{Ca}+^{124}\text{Sn}$ and the $^{48}\text{Ca}+^{112}\text{Sn}$ reaction are shown in Figure 3.1.
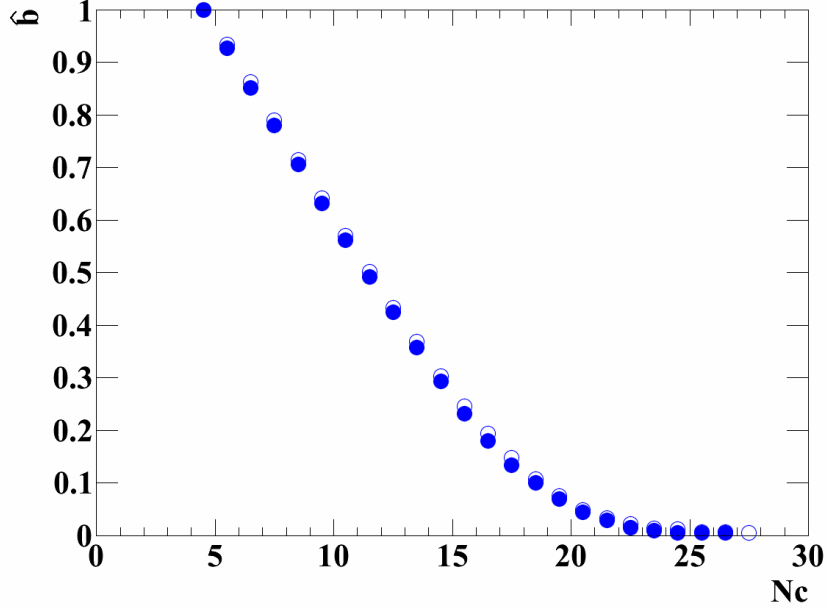
Figure 3.1: The calculated values of $\hat{b}$ corresponding to each charged particle multiplicity N_c for the ^{48}Ca beam. The ^{124}Sn target data are shown as solid circles and the ^{112}Sn target data are shown as open circles.

Central collision data are selected by $\hat{b}<0.3$. This cut corresponds to $14 \leq N_c$ for both reactions. Mid-peripheral collision data are selected by $0.3<\hat{b}<0.6$, which corresponds to $10 \leq N_c < 14$ for both reactions.

3.2   Neutron Wall Analysis

The Neutron Wall (NW) Array was analyzed together with the Forward Array (FA) and the Proton Veto (PV) Array. The FA was used to set the start time for an accurate determination of the neutron time-of-flight (TOF). The PV Array was used to remove charged particles from the neutron spectrum. Multiple corrections were applied to the neutron spectrum to account for losses and efficiencies.

3.2.1 Detector Calibrations

3.2.1.1 Time Calibrations

Neutrons that interact with the scintillating material in the NW detectors only impart a portion of their kinetic energy in the elastic collision, so correlating the incoming neutron kinetic energy to the resulting pulse height is difficult. A much more accurate measure of the neutron kinetic energy is the measured TOF, so a precise calibration of the timing elements is critical.

Because the data for this experiment were taken within a few months of experiment E09042, analyzed by Dan Coupland, with few changes made to the NW Array electronics or readout system between the two experiments, many of the calibrations obtained for the E09042 data could be applied to the present analysis. The E09042 timing was calibrated from data taken with an Ortec 462 time pulser. This time pulser can be programmed to output start and stop signals that produce peaks at evenly-spaced time intervals of a known length. The peaks in the pulsed TDC channel can be used to determine the correlation between the TDC channel and the time; in the E09042 calibration the relation was found to be linear. This method allows for a precise calculation of the slope of the TDC calibration; for both experiment E09042 and the present experiment, the correlation was about 100 ps per TDC channel for the NW Array and about 85 ps per TDC channel for the FA. However, information from the time pulser can not determine the offset of the time calibration, which is greatly affected by the trigger conditions and the structure of the data acquisition electronics. The final offset in the timing calibration is chosen so that the prompt gamma peak seen at the beginning of the TOF spectrum (Figure 3.2) travels the measured distance between the target and the center of the wall at the speed of light.
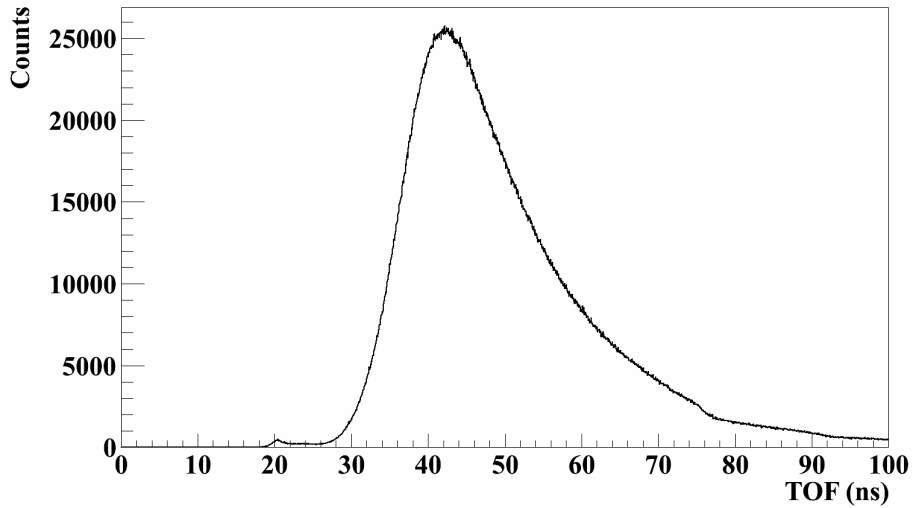
Figure 3.2: The NW TOF for the forward wall. The small peak at the beginning of the TOF spectrum, near 20 ns, is from prompt gammas. Later NW counts are from delayed gammas and massive particles.
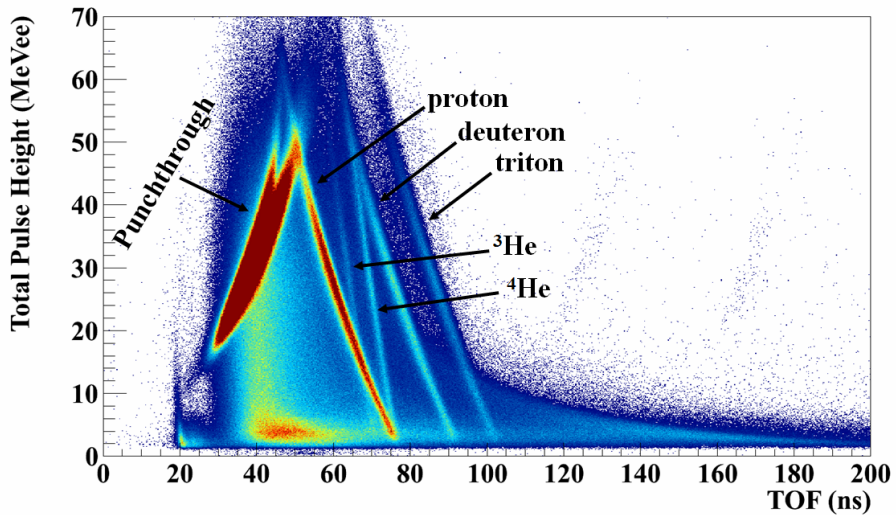
Figure 3.3: The NW particle identification (PID) plot for the forward wall. The time and pulse height are calibrated, but no corrections are made to the spectrum. The neutrons are visible at all times across the spectrum. Sharp stopping lines are observed for light charged particles from 50 ns to 100 ns. The broad sweep at low times and large pulse heights are hydrogen isotopes that punch through the detector and do not deposit their full kinetic energy.

The process of checking that the E09042 time calibrations could be applied to the NW-FA timing information began with the NW PID plots. As seen in Figure 3.3 the prompt gamma and the hydrogen and helium lines are easy to pick out on the broad spectrum of neutrons. First all bars within a wall were matched by checking the times of the prompt gamma, proton, deuteron, and triton lines at low pulse heights. The timing calibration deviated from the E09042 calibration for only the top eight bars in each wall, because one electronics module was switched between experiments: these bars were matched to the bottom bar of each wall.

The NW Array provided the time of neutron detection, which is the endpoint of the TOF calculation, but a start time is needed to determine the neutron TOF. During the experiment the FA OR signal provided the start to the clock, but the timing of the FA signals relative to the NW Array could vary depending on which FA element hit was registered in the discriminator first. FA timing differences could arise due to different cable lengths or to delays inherent to the discriminator module. To correct for timing differences between FA elements, first the self-timing peaks at the beginning of the FA time spectra were matched. Then the slopes of the FA element times were calibrated using the time pulser, as described earlier in this Section. A simple routine was followed to determine which of the 16 FA elements was hit first, therefore determining which element triggered the start of the FA OR signal, then that initial time was subtracted from the NW Array time. Because both the NW time and the FA time are measured relative to the FA OR signal, this procedure cancels out the FA OR time from both arrays and the result is the difference between the NW and FA times for the detected particle. An additional offset was added to the FA times so that the NW-FA prompt gamma peaks remained lined up for all bars. If no FA hit was recorded for an event, no time correction could be made, and the hit was removed from analysis.

3.2.1.2 Position Calibrations

The process of calibrating the NW positions was started by applying the calibrations for the E09042 experiment. The position matching between bars was checked using data runs taken during the experiment with an AmBe source. The AmBe source emits gamma rays with a Compton edge of 4.2 MeV that were detected along the length of each bar: there was a broad distribution of gamma events in the center of the bar with sharp fall-offs corresponding to either end. The length of each bar was calculated from the difference in the edges seen in the position spectra, while the center was calculated as the average of the two positions. The center and length of each bar were lined up and matched to the known experimental positions of the walls as recorded using a laser measurement system [48]. As with the time signals, only the positions of the upper 8 bars of each wall needed to be adjusted after applying the E09042 calibration data.

Experimental data with the shadowbars in place were used to verify the positions determined from the AmBe runs. The shadowbar locations were also accurately measured with the laser system as seen in Figure 3.4; the angles subtended by each brass shadowbar were calculated and then projected on to the Neutron Wall to determine the wall positions that would be shadowed in each configuration. An example of one such projection is shown in Figure 3.5. The shadowed spots varied by no more than 2 cm, well within the 7 cm position resolution available.

Information from the PV Array was also used to check the NW positions. The PV paddles were not measured precisely with the laser positioning system, so they were used to check position matching rather than as a calibration point. By selecting particles in the NW Array that were registered in a particular PV paddle, one can see a relatively sharp projection of

Figure 3.4: Dave Sanderson measured the shadowbar locations using a laser measurement system. The NW Array is seen behind the shadowbar mount.
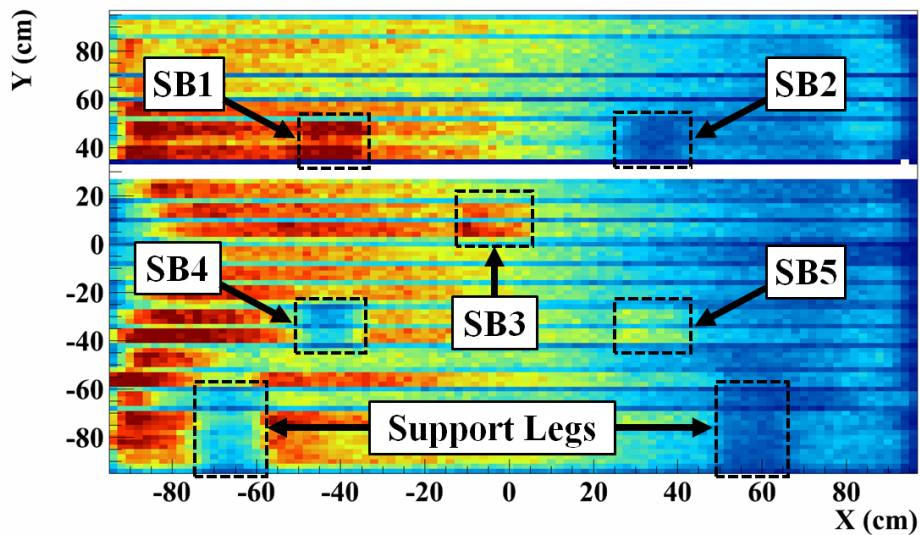
Figure 3.5: Position spectrum of the forward NW with shadowbars in place. The distances are measured from the center of the wall. Shadowbars are in place at SB2 and SB4, which are displayed as more blue than surrounding areas, representing fewer counts. Locations SB1, SB3, and SB5 are not at all shadowed in this configuration while the surrounding area is somewhat shadowed by the aluminum shadowbar mount. The outline of the shadowbar support legs can be seen in the lower third of the Figure.

54
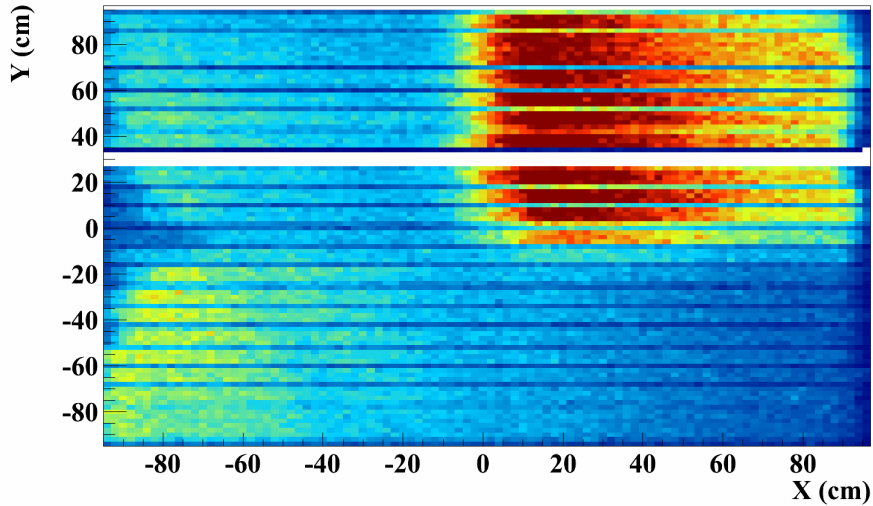
Figure 3.6: Position spectrum of the forward NW in coincidence with one element of the PV Array. The distances are measured from the center of the wall.

the paddle on the wall. The vertical edges that result on the NW position spectrum were used to check the matching between bars; one such example is shown in Figure 3.6. As with the data from the shadowbar runs, the events selected by PV paddle were found to line up within 2 cm.

One bar in the forward wall was removed due to poor position resolution across the bar.

3.2.1.3 Pulse Height Calibration

As with the time and position calibrations, the initial NW Array pulse height calibration was applied from the E09042 analysis. However, the pulse height information was found to differ significantly between the two experiments, so a new calibration was performed for the present data.

First, calibration data using two sources was examined. One set of data was taken using the AmBe source, which emits gammas with a Compton edge of 4.2 MeV, and the other with the ^{60}Co source, which emits gammas with a Compton edge of 1.1 MeV. These two

points, along with the zero point set by the pedestal value, allow for a precise calibration for low values of the total pulse height into units of MeVee, where 1 MeVee is the kinetic energy of an electron stopped in the NE-213 material that produces a light output pulse height equivalent to that created by a 1 MeV heavy particle stopped in the same material. To check the calibration at large pulse heights, the proton PID stopping lines were compared between the present experiment and E09042, as the NW bars should have identical light responses to incoming protons with the same TOF.

The data from the AmBe source demonstrated a position dependence for the detected pulse height. The Compton edge of the AmBe source was determined for 10 position bins across each bar; it registered at a lower pulse height in the center of the bar and higher at the edges. A position correction on the pulse height was therefore applied to every bar to account for the position dependence, so that particles with the same kinetic energy cause pulses of the same height independent of the position in the bar. The largest effect of the position dependence was at large pulse heights: correcting for the position effect therefore improved the detector resolution at large pulse heights, as could be seen in the sharpening of the charged particle stopping lines in the PID spectra in Figure 3.3.

With the total pulse height signals matched between NW bars and precisely calibrated, the last step was to match the fast signals. The fast signal is critical to construct the PSD in the NW Array and thereby separate neutrons from gammas, but a calibration is not necessary. To aid this endeavor, the fast signals for all bars were matched to the bottommost bar of each wall using the gamma line in the PSD plots constructed from the AmBe runs.

To the first order, only events that were read by both PMTs of a NW bar were analyzed. This removes hits from particles that deposited a very small amount of energy, resulting in a small pulse in the closest PMT but one not large enough to hit above the discriminator

threshold on the opposite side. It also removes particle hits that deposit a large amount of energy, large enough to overflow the QDC in the nearest side but low enough to be read by the farther PMT. The events in the latter group can be reconstructed to determine what the total pulse height would have been if the closest side had not overflowed. First, events with signals in both PMTs were used to determine how a single pulse height from one PMT compared to the total signal measured from both as a function of position. An example for the total pulse signals from one side of the forward wall is shown in Figure 3.7. The position dependence was fit with a simple exponential. That fit could then be applied to events where only the left signal was read in, to reconstruct what the combined signal would have been if the opposite side had not overflowed. Most of the events that were reconstructed using this method were located near the vertical edges of the NW Array and had large pulses. This process was repeated for both sides of the bars and for both the fast and total signals. An additional matching routine was required to bring the reconstructed fast signals in line with the lower-energy gamma line in the PSD spectrum. As a result of the reconstruction, the total number of non-gamma events available for analysis almost doubled.

3.2.1.4   Pulse Shape Discrimination

The Pulse Shape Discrimination (PSD) is constructed by comparing the integral of the initial 30 ns of the pulse generated in the NW bar, called the fast signal, to the integral of the total signal for the same event. For both the fast and the total signals, the geometric mean of the values recorded in the left and right sides of the bars is used in the analysis. The geometric mean is used because it removes some of the position-dependence of the signals. An example of a PSD is seen in Figure 3.8.

To facilitate analysis of the PSD spectrum, a flattened PSD is created by subtracting a
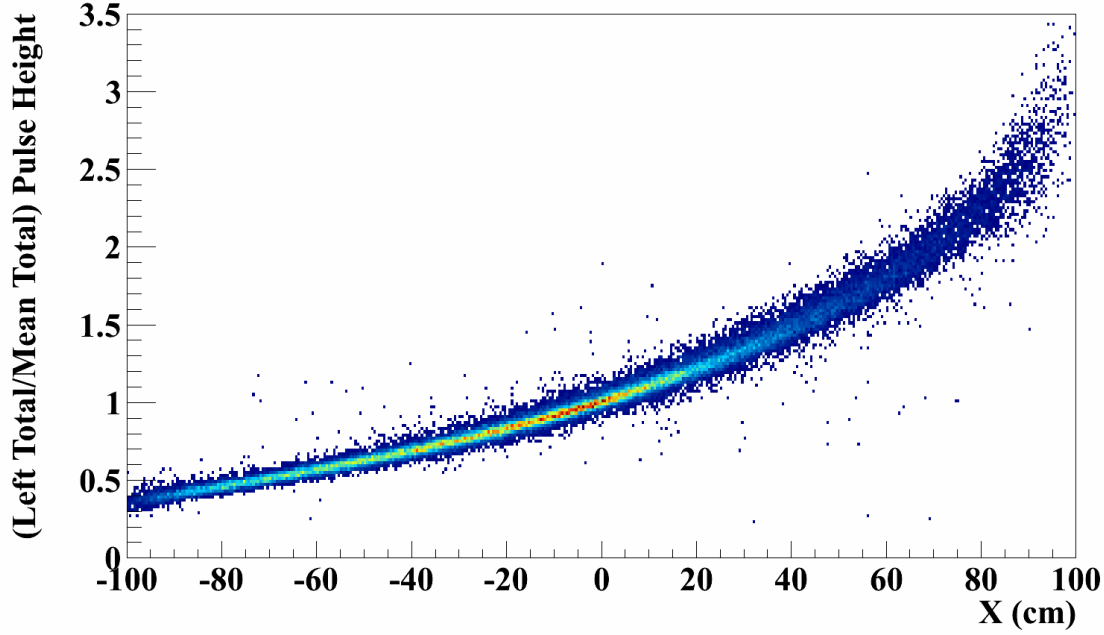
Figure 3.7: The total integrated signal for the left side of a single NW Array bar, divided by the geometric mean of the total signals from both sides of the bar, as a function of the hit position.

fraction of the total signal from the fast, so that the gamma line appears to be horizontal when the flattened signal is plotted against the total signal. The same data from Figure 3.8 are shown as flattened fast vs total in Figure 3.9. The lines corresponding to different particle species are spread out further from each other on the vertical scale, allowing for gates to be more easily drawn around each line. In this view, gammas, electrons, and punchthrough charged particles lie in the top line as the least ionizing particles. The next-most ionizing particles are located next, including hydrogen particles that stop in the detector and neutrons that elastically scatter off a hydrogen atom in the scintillating material. The bottom line contains the most ionizing particles, helium atoms or neutrons that interact with the carbon atoms of the scintillating material.
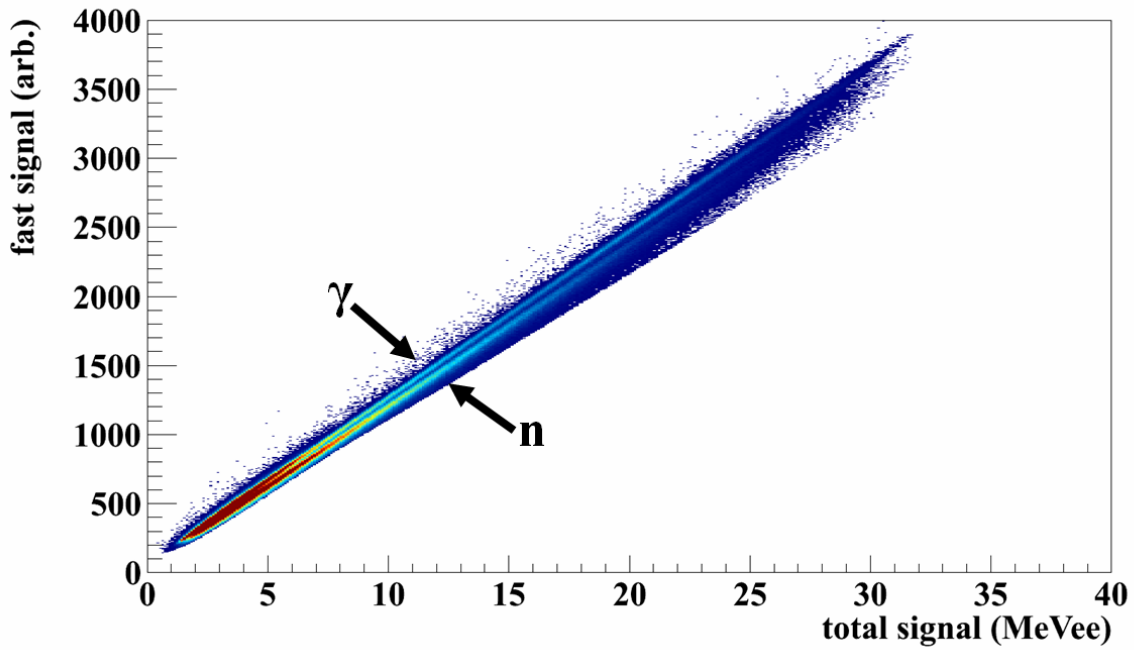
Figure 3.8: An example NW PSD spectrum, constructed by comparing the fast signal to the total signal. In this plot gammas lie on the upper line and neutrons lie on the lower line.
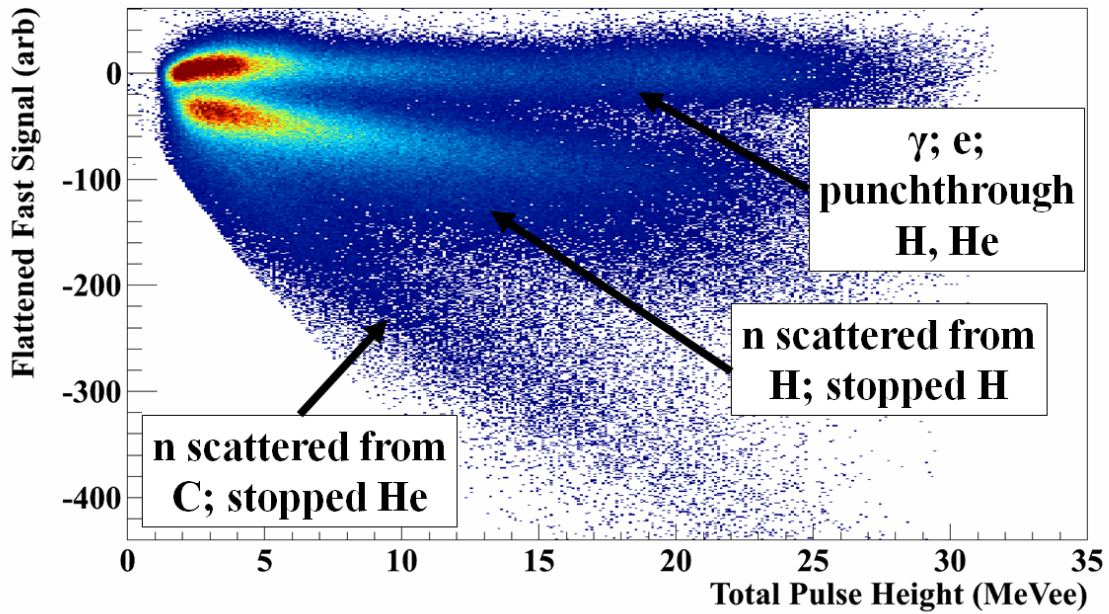
Figure 3.9: A "flattened" PSD plot, produced by subtracting a portion of the total signal from the fast so that the gamma line appears flat as a function of the total signal.

3.2.1.5 Proton Veto Matching and Charged Particle Identification

In theory, any particle detected in the Proton Veto (PV) Array should be a charged particle and the event can be removed from the NW spectrum. In practice, however, there is some amount of background in the PV Array that makes the identification of charged particles more difficult, even after removing events due to noise or cross-talk between paddles. One diagnostic we can use to select the true charged particle events from the PV Array is the PV PID information, found by comparing the pulse height recorded in the PV Array to the NW TOF. Without any corrections, the PID lines appear to be smeared out in PV pulse height with some position dependence. Particle position information is not recorded directly by the PV Array, but the position dependence can be corrected using the NW position information. A PV PID spectrum was generated for each paddle, divided into groups by the NW bar that recorded the hit, and further divided into 12 position bins along each NW bar. The PV PID lines in each of these position-gated spectra were matched to the lines seen in the center bin of a single paddle. After this procedure, the PV PID spectra become matched for all paddles in the experiment and relatively narrow gates can be taken around the charged particle lines to select those out for further analysis. For some areas in the PV paddles the resolution of the PID lines worsen drastically, generally these are locations close to the PMT. Areas with poor PID resolution were excluded from analysis. The initial PV PID can be seen in the upper panel of Figure 3.10 and the final, matched PV PID is in the lower panel of Figure 3.10. The lower line corresponds to hydrogen particles while the upper line corresponds to helium particles.

By selecting particles that fall within a given PV hydrogen PID line and drawing the NW position spectrum, the area of the wall shadowed by that paddle is apparent. The edges

60
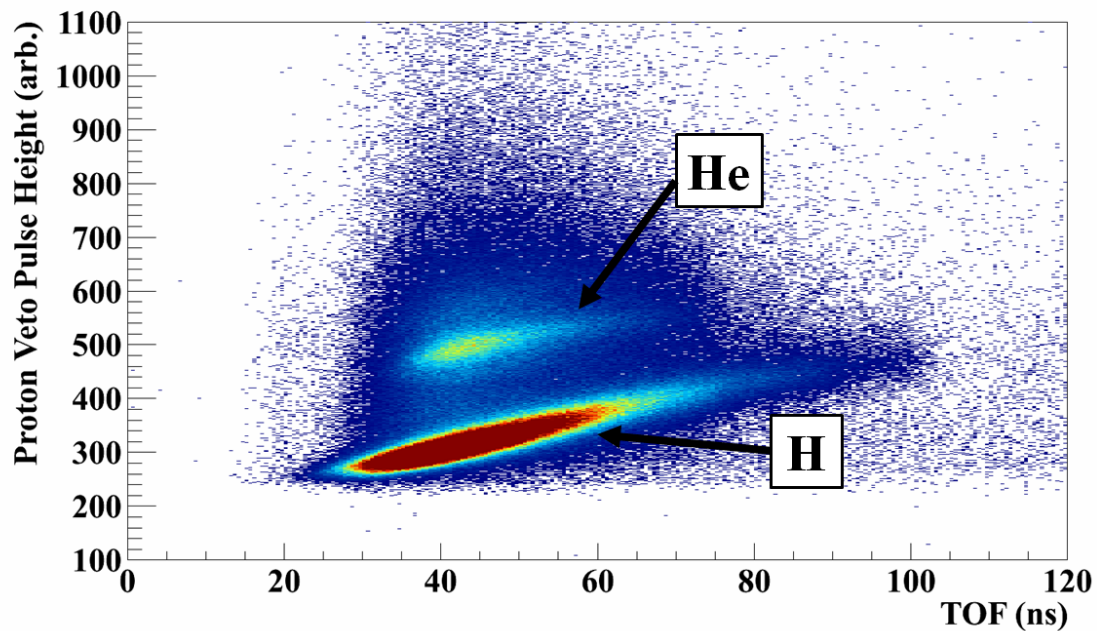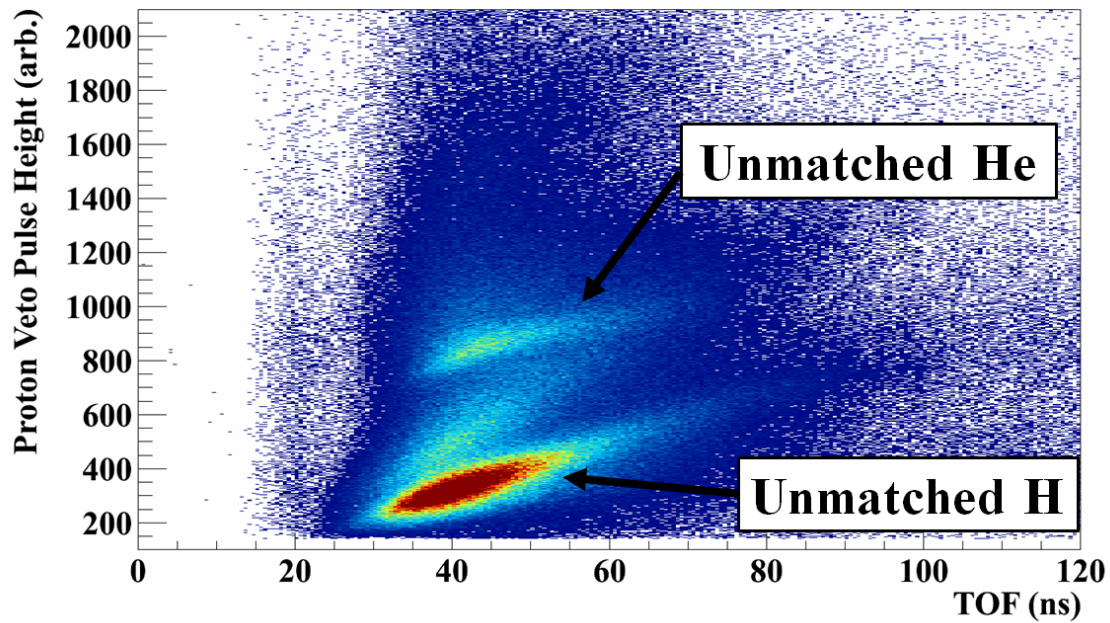
Figure 3.10: Proton Veto particle identification (PID) plot constructed from the PV pulse height against the NW TOF. The lower bands are hydrogen particles, the upper bands are helium particles. Upper: the PV PID from the raw pulse heights of the paddles. Lower: the PV PID after implementing position matching based on the position of the corresponding hit in the NW. The PID bands are noticeably narrower after matching positions and removing areas with poor resolution.

on this gated position spectrum are taken as the extent of the PV paddle's shadow. Some portions of the walls are not well covered by the paddles: the forward wall lacks coverage on the outside edges and there are a few gaps between PV paddles shadowing the backward wall. Regions of the NW Array that are not covered by the PV paddles were removed from further analysis. Additionally, the forwardmost lower paddle of the PV Array was found to suffer from very poor efficiency and the area of the NW shadowed by that paddle was removed entirely from the analysis, thus reducing the number of events at forward angles but greatly improving the certainty of those events.

3.2.2   Event Reconstruction

Information from both the NW Array and the PV Array are used to determine the potential identity of particles detected in the NW Array. A flowchart illustrating this determination is shown in Figure 3.11. Events in the PV Array are gated by the PV PID lines: a hit outside of those gates was considered as background during the analysis. Events in the NW Array that fell inside the gamma PSD gate were labeled gamma particles and were not considered in the later steps of the routine. Next, all possible matches were checked between the NW and the PV paddle that shadows that NW location. If such an event matched the criteria of falling within a PV PID line and not falling in the gamma PSD gate, it was considered a charged particle and the PV PID was used to label the hit as a hydrogen or a helium. If there were no hits in the PV Array element shadowing the NW location, the event was called a neutron.

This routine was followed if either the number of hits in the NW Array and the PV paddle shadowing that area matched, in which case all were considered charged particles, or if there were no PV paddle hits for any number of NW Array events in the shadowed
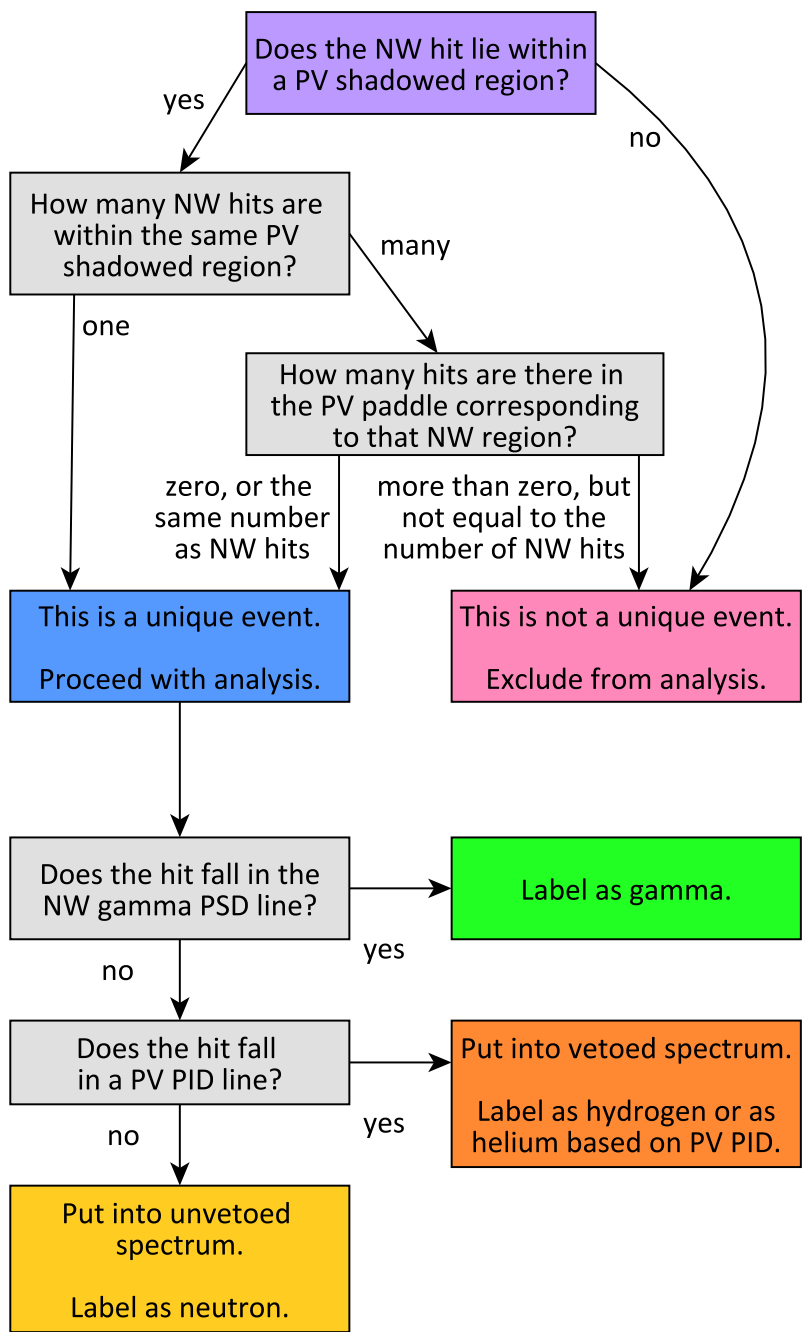
Figure 3.11: The decision process used to determine whether a NW Array event could be determined as a unique event, and if so what label it should be given.

location, in which case all were considered neutrons. If there was a mismatch in the number of events, for example if only one PV paddle hit was registered for two shadowed NW hits, those NW events were not considered unique and were rejected. Areas of the arrays that had poor coverage or were rejected from later steps in the analysis were considered in this determination prior to removal of those events.

The increased segmentation of the PV Array at backwards angles kept the rejection rate low in the backward wall, peaking at 4% and generally staying around 1% for most TOF values and for all reaction systems. The rejection rate was higher in the forward wall, which was expected because of the higher event multiplicities at forward angles and the lower number of PV paddles that shadowed the forward wall. The TOF-dependent rejection rate for the forward wall had a maximum value of 13% at small TOF values.

The forward wall rejection rates exhibited an additional dependence on position: 15% of the events were rejected from the forward half of the wall while only 6% were rejected from the less-forward half. No position dependence was observed in the rejection rates of the backward wall.

3.2.3 Efficiencies

3.2.3.1 Reconstruction Efficiency

The unvetoed particles identified in the routine detailed in Section 3.2.2, the unique hits not in coincidence with a PV Array hit, cannot be reliably considered neutrons. A large factor for the unreliability of neutron identification is the efficiency of the PV Array. Because each paddle is not 100% efficient, some charged particles will not be detected in the PV Array and would be labeled as neutrons. To a lesser degree, some of the particles removed in the

vetoed spectra are part of the background and are actually neutrons.

To better quantify the contribution of the charged particles to the NW spectra, the PID lines of the hydrogen stopping lines were first straightened using a quadratic fit of the form:

$$H_{str} = TOF + a \cdot L + b \cdot L^2 \tag{3.4}$$

where TOF is the measured time-of-flight of the particles in ns and L is the calibrated light output in MeVee. For the forward wall, a = 0.797 ns/MeVee and b = -0.00499 ns/MeVee^2. For the backward wall, a = 0.690 ns/MeVee and b = -0.00461 ns/MeVee^2. Applying these factors to both the vetoed and the unvetoed NW spectra within working position cuts and with gamma rays removed, then projecting the spectra, led to the sharp charged particle peaks seen in Figure 3.12. One can see that charged particles clearly remain in the unvetoed spectrum. It is likewise obvious that the vetoed spectrum contains more than just the charged particles, judging from what looks like a large background around the charged particle peaks.

The first step to fully separate the neutrons and charged particles is to estimate the proton veto efficiency, ϵ_{pv}, as the proportion of protons from the total NW spectrum that are correctly identified in the PV Array, and the background fraction, f_{bkgd}, in the PV Array. The f_{bkgd} was calculated as the ratio of particles that lie between the deuteron and triton peaks in the vetoed spectrum compared to the total spectrum. The average value for ϵ_{pv} was calculated by fitting a Gaussian to the proton line for both the total and vetoed spectra. An example of the fits used is shown in Figure 3.13, where the charged particle peaks are fit with Gaussian curves in black and the backgrounds of those peaks are shown in red.

Comparing the counts within the proton peaks was found to be an imprecise determination of ϵ_{pv} for two reasons. First, the shape of the proton peak differs between the vetoed
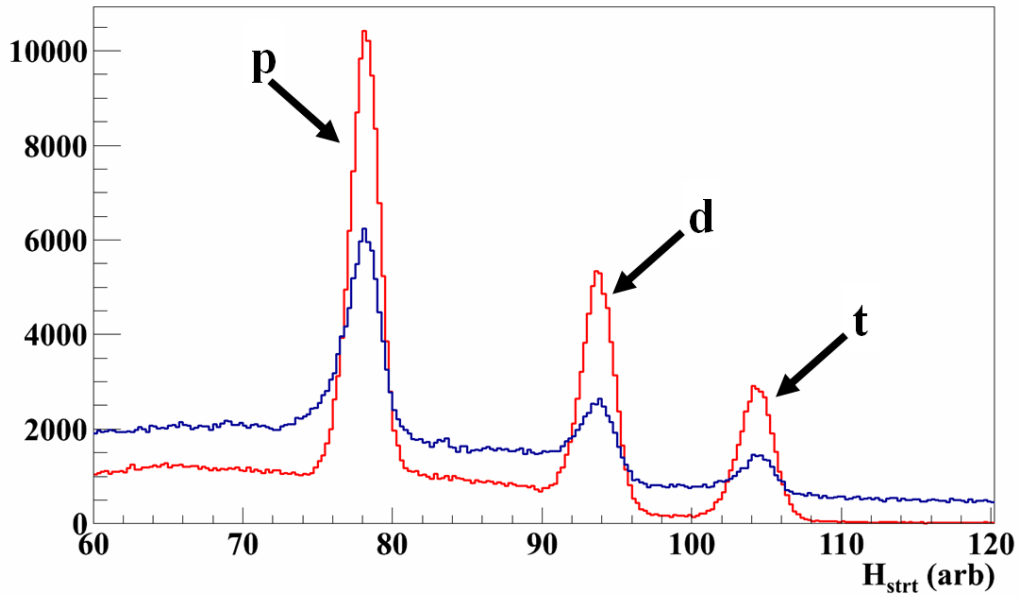
Figure 3.12: Neutron wall spectrum for the forward wall after removing bad positions and gamma rays, straightening, and projecting the spectrum. The peaks for protons, deuterons, and tritons are clearly visible in both the vetoed (red) and unvetoed (blue) spectra.
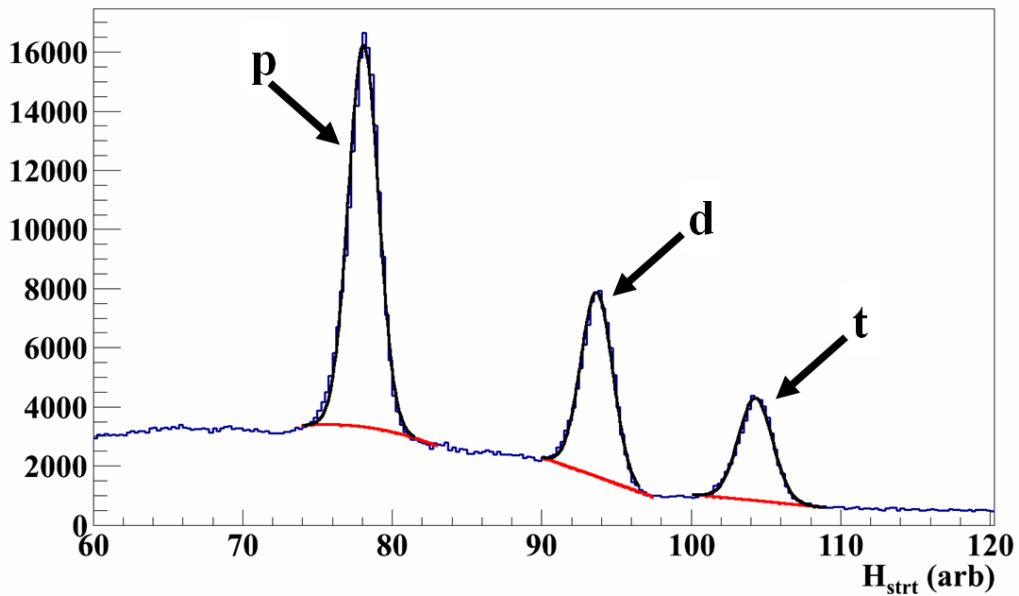
Figure 3.13: Total neutron wall spectrum for the forward wall after removing bad positions and gamma rays, straightening, and projecting the spectrum. The peaks for protons, deuterons, and tritons are fit with Gaussians, shown as a black lines, and the background fits are shown as red lines.
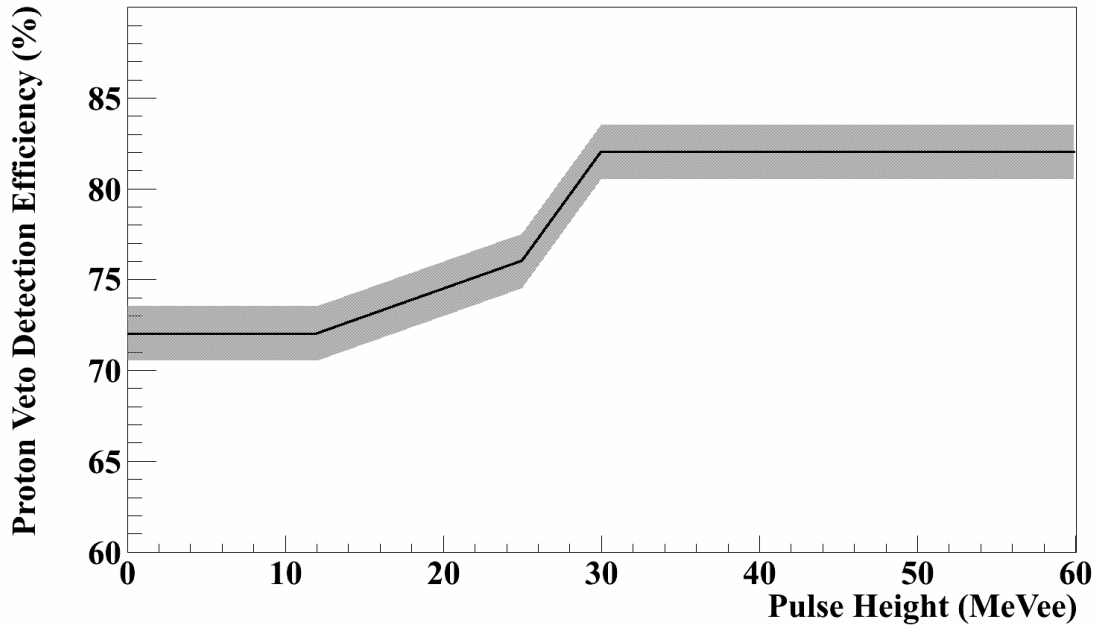
Figure 3.14: Proton detection efficiency in the PV array, ϵ_{pv}, for ^{48}Ca+^{124}Sn system in the forward wall as a function of the total light output in the neutron wall.

and total spectra, with protons at higher TOF (at larger values of H_{str}) less likely to be identified in the PV Array. An additional Gaussian was artificially fit to the right edge of the straightened peak to account for this difference in shape. Second, the proton detection efficiency varied with the light output L in the NW: protons with larger L had a higher ϵ_{pv} than protons with smaller values of L. The final ϵ_{pv} for each reaction system was determined manually to maximize the separation of the proton line from the total spectrum across TOF and L. An example of the ϵ_{pv} for the forward wall for the ^{48}Ca+^{124}Sn system is shown in Figure 3.14. The background fraction f_{bkgd} was kept at a constant value for TOF and L. The fits for both f_{bkgd} and ϵ_{pv} were repeated for each beam-target combination and each of the four detection regions in the NW Array that were determined by the PV Array coverage. Because of the error associated with a manual determination of the efficiency, the contributions to the systematic error were estimated from neutron spectra calculated with

67

ϵ_{pv} $\pm 1.5\%$. These systematics are discussed in Section 3.4.

We can extract the neutron spectrum, S_n, from the total spectrum, S_{tot}, and the vetoed spectrum, S_v, using the calculated quantities for f_{bkgd} and ϵ_{pv}. The total spectrum can be expressed both as the sum of the neutron and charged particle spectra (S_n and S_{ch}) and as the sum of the vetoed and unvetoed spectra (S_v and S_u).

$$S_{tot} = S_n + S_{ch} = S_v + S_u \tag{3.5}$$

The vetoed spectrum contains charged particles that were correctly identified in the PV Array and neutrons that were incorrectly identified. The unvetoed spectrum therefore contains charged particles that were incorrectly identified in the PV Array and neutrons that were correctly identified. Expressing these statements in terms of f_{bkgd} and ϵ_{pv}, we can write

$$S_v = \epsilon_{pv} S_{ch} + f_{bkgd} S_n \tag{3.6}$$

$$S_u = (1 - \epsilon_{pv}) S_{ch} + (1 - f_{bkgd}) S_n \tag{3.7}$$

Solving for the neutron and charged particle spectra in terms of the total and vetoed spectra yields

$$S_n = \frac{\epsilon_{pv} S_{tot} - S_v}{\epsilon_{pv} - f_{bkgd}} \tag{3.8}$$

$$S_{ch} = \frac{S_v - f_{bkgd} S_{tot}}{\epsilon_{pv} - f_{bkgd}} \tag{3.9}$$

Some regions in the NW PID are not well described by Equations 3.5-3.9. In some cases, it appears that the deuteron and triton stopping lines were over-corrected by applying the proton detection efficiency: the resulting neutron spectra yielded negative counts where the

deuteron and triton stopping lines are located. Because neither the deuteron nor the triton lines contained enough information to introduce additional deuteron or triton PV detection efficiencies, the affected PID regions were removed from neutron analysis. This affected larger times-of-flight and resulted in a cut on lower kinetic energy (lower P_t).

Lastly, some proportion of particles were rejected because the NW hit could not be uniquely identified, as described in Section 3.2.2. To determine the extent of this effect, a ratio of rejected events to total events was calculated as a function of the NW TOF within each analysis region and for each beam-target combination. This TOF-dependent rejection fraction, $f_{rej,TOF}$, was fit with a polynomial of up to the sixth order. The additional position-dependent rejection fraction for the forward wall, $f_{rej,pos}$, was fit as a Fermi step function. The rejection correction was then applied using the factor $(1 - f_{rej,pos} \cdot f_{rej,TOF})$.

3.2.3.2 Scattering Background

The path between the target and the NW Array contains many obstacles that can potentially scatter neutrons. This can create an indirect neutron path that is not only longer, but may also be detected at a polar angle that differs from the angle of emission, leading to an incorrect determination of the kinetic energy and emitted neutron position. To measure the contribution of the background scattering, brass shadowbars were arranged between the target and the NW Array in a specially designed stand that could accommodate the shadowbars in any combination of five locations. In Figure 3.5, the shadowbars were located at the lower half of the forwardmost section of the wall and at the upper half of the more backward section. The 30 cm thickness of the brass shadowbars should stop any neutrons emitted from the reactions traveling on a direct path from the target. One such bar is shown in Figure 3.15.

Figure 3.15: A 30 cm bar used to shadow the NW Array.

The region in the NW Array covered by the shadowbars should have fewer counts compared to surrounding areas, because only the particles that took an indirect (scattered) path would be detected immediately behind the shadowbars. There are some particles that are stopped in or scattered by the aluminum plate that forms the face of the shadowbar mount, so the three shadowbar locations that were not used in the experimental runs shown in Figure 3.5 are the only areas without any extra material between the target and the NW Array and therefore see slightly more counts compared to the surrounding positions.

If the neutron distribution across a bar were isotropic and the brass bars blocked all incoming neutrons, we would see a flat distribution of neutrons as a function of position with a square well corresponding to the spot shadowed by the shadowbar. The proportion of neutrons found in the well compared to those found on either side provides a reasonable estimate of the scattering background, as only neutrons that took an indirect path should be able to reach the portion of the wall covered by the shadowbar. In reality, the initial position distribution peaks at small polar angles in the laboratory frame and the neutron yield decreases with larger angles. In addition, the projected shape of the shadowbars has

curved edges due to the detector position resolution. Therefore a simple square well cannot be expected to fit the one-dimensional projection perfectly. An example position spectrum of a shadowed NW bar is shown in the upper panel of Figure 3.16. A linear fit was applied to the region of the wall not shadowed by the shadowbar and the spectrum was straightened by dividing the empirical bin value by the fit value for each position, with the result shown in the lower panel of Figure 3.16. The average value of the background in the straightened 1D spectrum is 1.0 by construction. The straightened spectrum was then fit with a square well with curved edges of the form:

$$\left(1 + 0.5 erf\left(-\frac{x - x_0}{\sqrt{2}\sigma_0}\right) + 0.5 erf\left(\frac{x - x_1}{\sqrt{2}\sigma_1}\right)\right) \cdot s + b \tag{3.10}$$

where $x_{0,1}$ and $\sigma_{0,1}$ are the locations and resolutions of the edges of the well, erf is the Gaussian error function, s is the signal fraction and b is the background fraction. Because this experiment used the same location and setup of both the NW Array and the shadowbars as the experiment E09042 in Ref [2] , some of the values calculated from the previous analysis could be applied to the fits, namely σ=2.8 cm and the width of the well $x_0 - x_1$=17.7 cm for the forward wall and $x_0 - x_1$=14.5 cm for the backward wall. Remembering the constraint that $s + b = 1$, only two variables remained to be constrained, x_0 and b. The best fit was selected for x_0 from all shadowbar runs, then all shadowed position spectra were refit to constrain the last variable, the background fraction, b.

Each individual shadowbar could project onto two or three NW bars, depending on the position of the shadowbar, as seen in Figure 3.17.

In the case where three NW detector bars were shadowed, the outside two bars are only partially shadowed in the vertical direction, but the center bar has full vertical coverage and
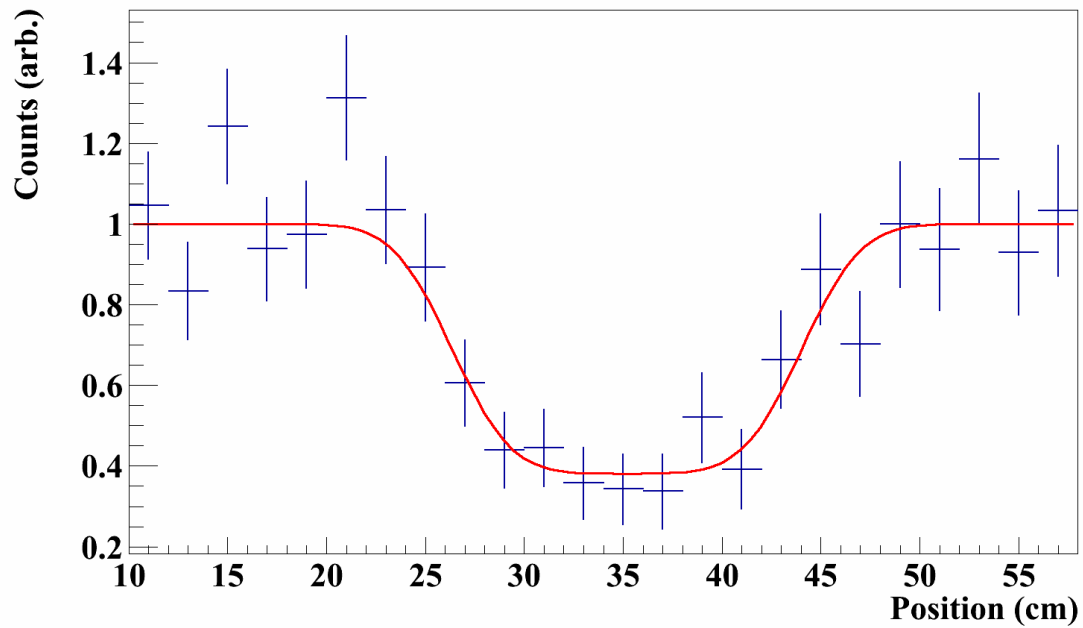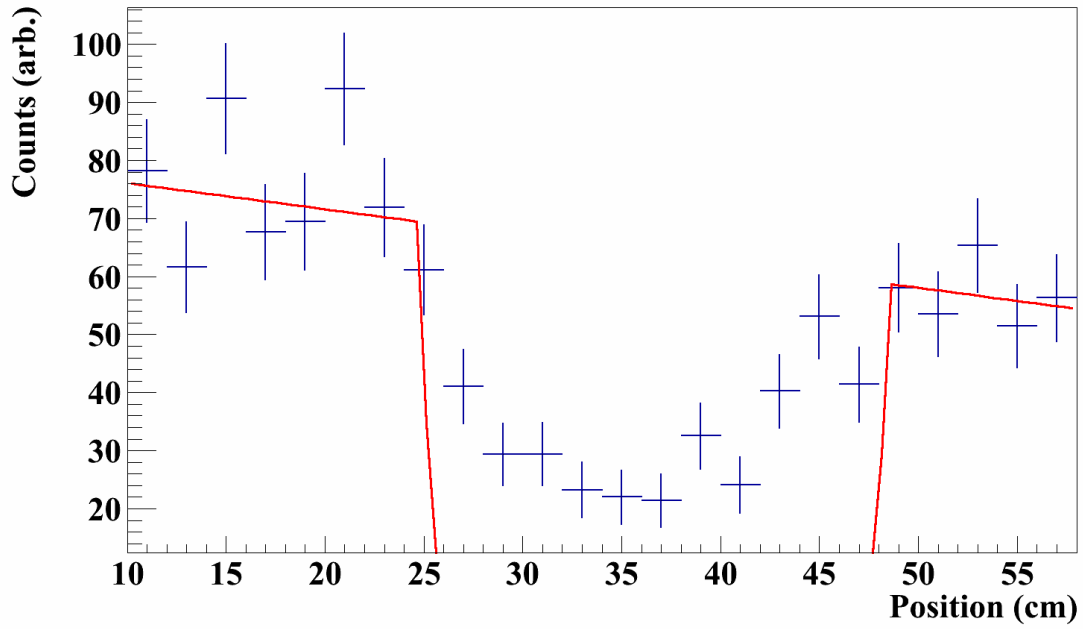
Figure 3.16: Upper: 1D spectrum of a shadowed NW bar. Lower: Straightened 1D spectrum from the same data, scaled so that the unshadowed region is 1. The bottom of the well shows the background fraction.
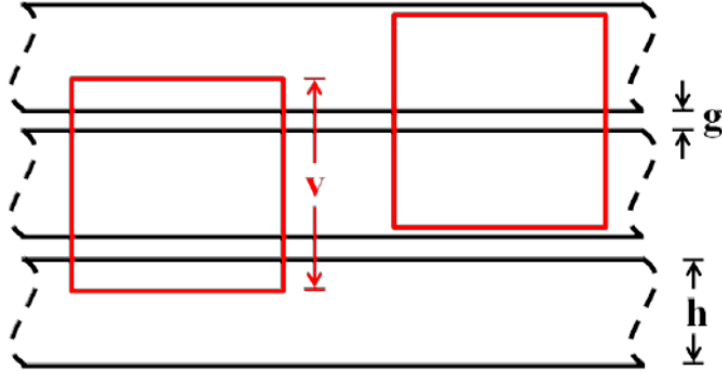
Figure 3.17: Possible shadowing of shadowbars on the NW Array. In the case on the left, 3 NW bars are shadowed: the center one is shadowed fully and the other two are only partially shadowed. In the case on the right, 2 NW bars are both partially shadowed. [2]

therefore provides the easiest determination of the scattering background. In the forward wall, two shadowbar positions met this condition out of the four positions that were also shadowed by working PV paddles, so analysis of the scatting background in the forward wall primarily relied on those two locations. In the backward wall, only three shadowbar locations were well-covered by the PV paddles; of these three, only one shadowbar had full vertical coverage of a NW bar.

Data from NW bars not fully vertically covered by the brass shadowbars can still be used to calculate the background scattering. Where only two NW bars are shadowed by a particular shadowbar, we can calculate the fractional coverage f_i of each bar:

$$v = h(f_1 + f_2) + g \tag{3.11}$$

where $h = 7.62$ cm is the height of the NW detector bar, the gap between bars is $g = 0.98$ cm, and v is the vertical height of the shadow. Assuming the vertical shadow extends 4% larger than the measured horizontal width, v is 18.2 cm for the forward wall and 15.3 cm for the backward wall [2]. Then if we define the fractional coverage of bar i, f_i, in terms of the

73

measured background fraction β_i and the true background fraction β_0, we see that

$$f_i = \frac{1 - \beta_i}{1 - \beta_0} \tag{3.12}$$

The ratio of fractional coverages of the two shadowed NW bars, f_{12}, can be expressed

$$f_{12} = \frac{f_1}{f_2} = \frac{1 - \beta_1}{1 - \beta_2} \tag{3.13}$$

Solving Equations 3.11 and 3.13, we see that

$$f_1 = \frac{v - g}{h} \frac{f_{12}}{1 + f_{12}} \tag{3.14}$$

$$f_2 = \frac{v - g}{h} \frac{1}{1 + f_{12}} \tag{3.15}$$

It is possible that the shadow can extend into the gap below the bottom NW bar of the pair or above the top NW bar, or even to cover a third bar to a slight degree. If this is the case, one bar will be fully covered and would have a true fractional coverage of one, but solving the Equations above will calculate the coverage as greater than one, which is not physically possible. An additional factor can be introduced to account for the extra extent of the coverage past the two bars, s.

$$f_1 = \frac{v - g - s}{h} \frac{f_{12}}{1 + f_{12}} \tag{3.16}$$

$$f_2 = \frac{v - g - s}{h} \frac{1}{1 + f_{12}} \tag{3.17}$$

This factor s can be fit using all shadowbar data for a specific location so that the fractional

coverage of the fully-covered NW bar is calculated to be 1, then the same value for s is used to determine the coverage of the partially-covered NW bar. In all cases, calculated values for f_i were averaged between different beam-target combinations, assuming that the shadowbars were set up exactly the same way each time, and the averaged fractional coverage was used as a constrained parameter to determine the amount of the background scattering. The resulting calculated background β_0 from cases where a brass shadowbar fully covered the height of a NW detector bar was cross-checked by values of β_0 calculated from partially-covered bars.

Scattered neutrons will take an indirect flightpath from the target to the NW Array. Therefore there may be a dependence of the background scattering on the TOF, as longer flight paths will have longer TOFs than a direct path. To measure the effect of the TOF dependence on the fractional background scattering, the events in the forward wall were separated into two TOF bins with equal statistics. More TOF bins could not be used due to an overall low number of counts in the shadowbar runs; the backward wall did not have enough statistics to be divided into multiple TOF bins. In general, there was less neutron scattering in the lower TOF bin. The background scattering of the two TOF bins was fit with a linear equation to the average TOF for each bin, with the result extended to all values of TOF as in Equation 3.18.

$$Bkgd_{wall0} = A \cdot TOF + B \tag{3.18}$$

The fractional background scattering was found to be independent of the target used. For the ^{48}Ca beam, A = 0.00141 TOF^{-1} and B = 0.221. When applied to the measured TOF, the background scattering ranges from 26-42% in the forward wall. No correlation could be
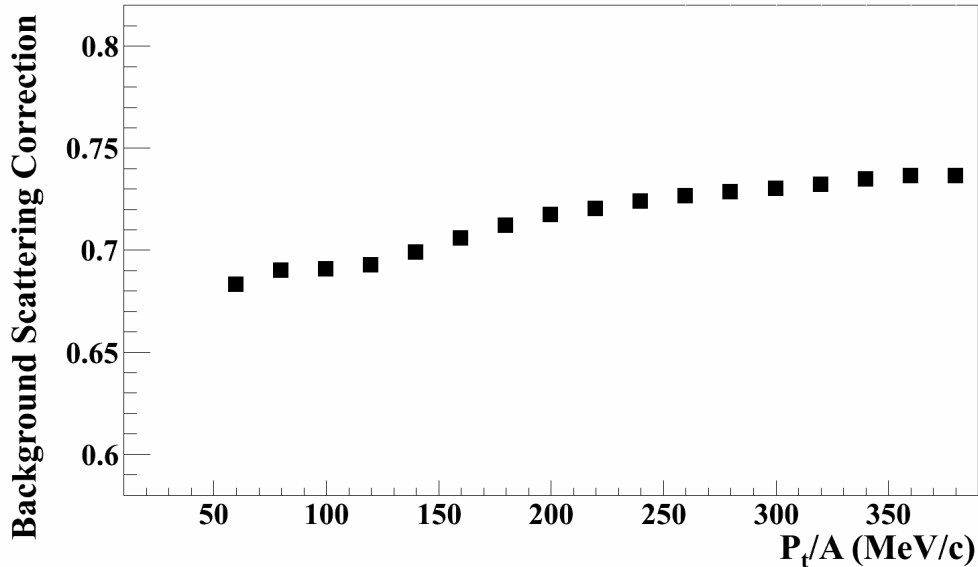
Figure 3.18: The calculated correction for background scattering in the forward wall as a function of the transverse momentum.

found between scattering background and polar angle or height of the bar. In the absence of more detailed data, the scattering fraction in the backward wall was taken as a constant: 0.402. The correction factor $(1 - b)$ for the ^{48}Ca beam data in the forward wall is shown in Figure 3.18 as a function of the neutron transverse momentum.

To estimate the systematic uncertainties in the calculation of background scattering, most fit parameters in Equation 3.10 were varied: the position resolution σ by $\pm$ 0.5 cm and the shadowed width $x_1 - x_0$ by $\pm$ 2.0 cm. The uncertainty in the background was taken to be $\pm 10\%$ of the calculated background value and was included in the neutron spectra systematic error. These systematics are discussed in Section 3.4.

3.2.3.3 Geometric Efficiency

The total area of the NW Array included in the final analysis is shown in Figure 3.19, with areas removed that correspond to positions of the shadowbars or the shadowbar mounts,
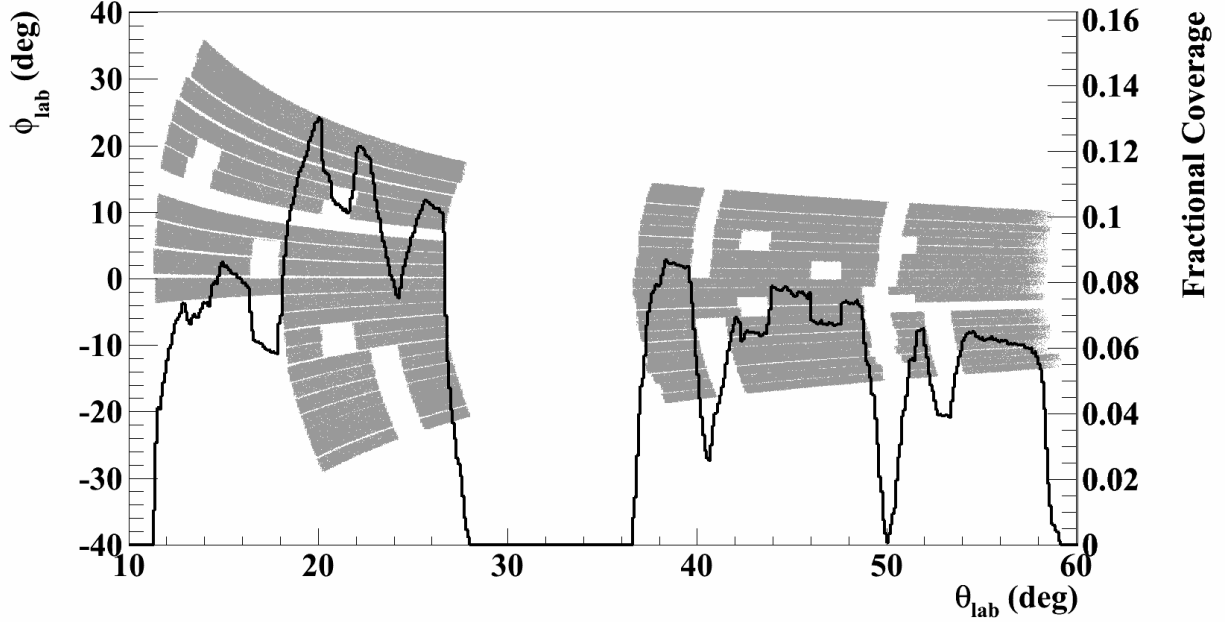
Figure 3.19: Azimuthal coverage of the NW Array in the Lab frame. The shaded region shows the positions of the two walls in the lab polar angle (θ_{lab}) and azimuthal angle (ϕ_{lab}). The solid line shows the fractional ϕ_{lab} coverage as a function of θ_{lab}.

lack of coverage from the PV Array, or NW Array bars or PV paddles with low detection efficiency or poor resolution. The line superimposed on the Figure corresponds to f_ϕ, the fractional coverage of the detector in the azimuthal direction. This quantity is calculated as $f_\phi = d\phi/360°$ where $d\phi$ is the total azimuthal angle covered per polar angle bin (in degrees). Correcting for the coverage of the detectors allows for a better comparison to theoretical calculations, in which particles are summed over all azimuthal angles. To eliminate the problem of a small f_ϕ factor greatly inflating the small statistics from the edges of the distribution, events are not considered from polar angles for which $f_\phi<0.03$.

3.2.3.4 Detector Physical Efficiency

The detector efficiency of the NW Array is a measure of the likelihood that a neutron with a particular incoming kinetic energy will interact with the scintillating material and deposit

enough energy to be registered by the PMTs at either end. The efficiency was calculated using a program called SCINFUL-QMD, developed by Satoh et al. at the Japan Atomic Energy Agency [44], which incorporates the quantum molecular dynamics plus the statistical decay model (QMD-SDM) into the SCINFUL code developed for liquid organic scintillators at Oak Ridge National Laboratory.

The transport processes are the first step of the calculation, in which neutrons, protons, and pions are propagated through the NE-213 organic scintillating material used in the NW Array and known total cross sections are used to determine if the simulated neutron collides with a nucleus in the scintillating material. The cross sections are taken from experimental data with a neutron source and NE-213. If a collision occurs, a nuclear reaction channel is selected from all the possible channels and the resulting deposited energy is calculated. For each interaction, the path length to the scintillator surface is calculated and used to determine the light output response function, which describes the probability of obtaining a light signal of a certain pulse height for a given neutron incident energy.

The calculation step with the greatest uncertainty is the conversion from the incoming neutron kinetic energy into the light output caused by the deexcitation of the scintillation material. For the detection efficiency performed in this analysis, the light response function used describes experimental light output data of light charged particles (p, d, t, ^{3}He, and ^{4}He), as the kinetic energy can be more accurately measured for charged particles than for neutrons [44]. While different particles excite the NE-213 to different proportions of excited states, the light response from the deexciting NE-213 should be the same for the same excited states, regardless of what particle species caused the excitation. An example light output response is shown in Figure 3.20 for neutrons with $E_{kin,lab}$=65 MeV incident on a simulated NE-213 bar matching the dimensions of those used in the NW Array. In this
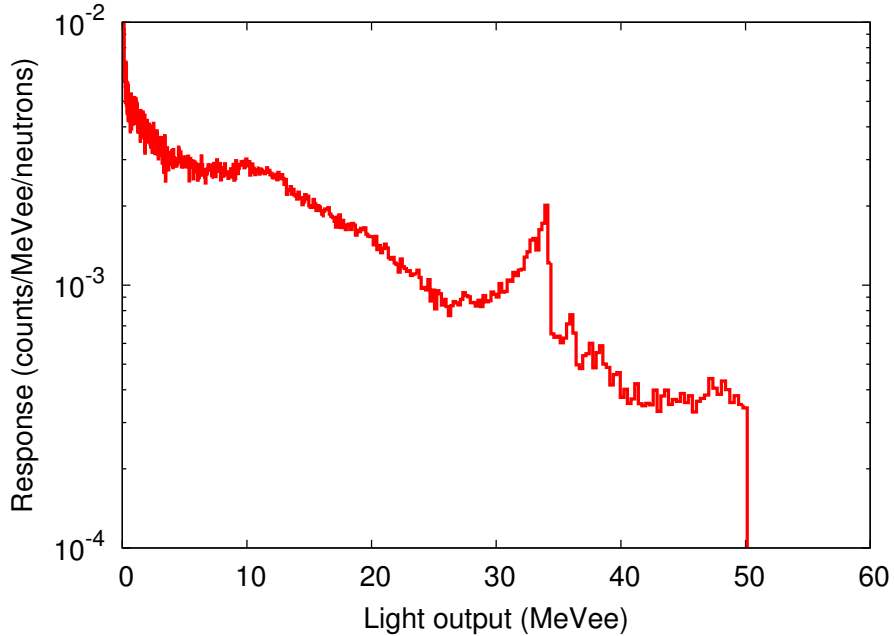
Figure 3.20: Light Response from SCINFUL-QMD for neutrons with incident kinetic energy of 65 MeV in the simulated NW Array NE-213 bars.

case, the responses from high-energy protons that punch through the bar are not considered. Punchthrough protons are removed in the PSD analysis for experimental data because they have a PSD shape that is very similar to that of gamma events, so the punchthrough protons are also removed in this step of the calculation to make the two more comparable.

The detection efficiency for neutrons of a given incident kinetic energy is then determined by integrating the light response above the experimental hardware threshold. For the data presented here, the thresholds were set at 2 MeVee. In this calculation, the efficiencies for a range of incident energies from $E_{kin,lab}$=10 MeV to 200 MeV were calculated in 5 MeV steps. The detection efficiencies for incident neutrons in between the calculation's energy steps were found by extrapolation. The exception was for energies between 80 MeV$<E_{kin,lab}<$150 MeV, where SCINFUL-QMD cannot accurately describe the light outputs; the original formulation of SCINFUL was capable of describing light outputs up to $E_{kin,lab}$=80 MeV. By including QMD methods, the upper limit was extended to 3 GeV, but is not very accurate up to
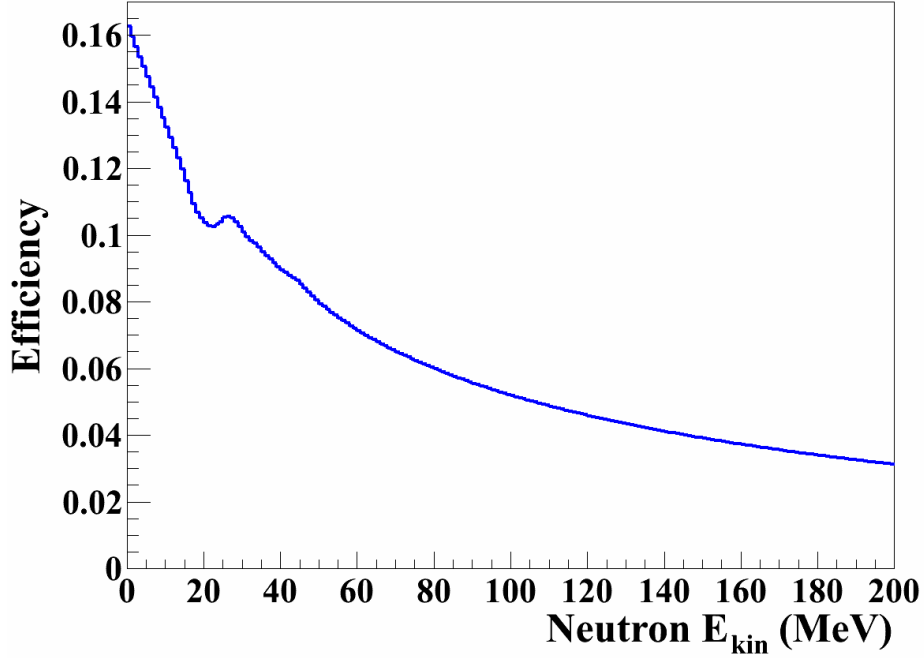
Figure 3.21: Detection Efficiency from SCINFUL-QMD for the 2 MeVee hardware threshold.

$E_{kin,lab}$<150 MeV. The efficiencies of neutrons from 80 MeV<$E_{kin,lab}$<150 MeV were found by fitting the points from 50 MeV$\leq$$E_{kin,lab}$$\leq$80 MeV and 150 MeV$\leq$$E_{kin,lab}$$\leq$200 MeV. The resulting detection efficiencies are shown in Figure 3.21.

Above the range of $E_{kin,lab}$ > 40 MeV, which are the neutron energies used in this analysis, the highest detection efficiency is about 8.5%. The majority of neutrons analyzed are from higher kinetic energies for which the detection efficiency is closer to 4% or below. Correcting for such low detection efficiencies has a large effect on the data. Even small deviations in the detection efficiency could therefore cause large changes in the neutron spectra. Because of the difficulties in neutron detection, the systematic errors from neutron detection efficiencies were estimated at ±10%. The resulting systematics are included in Section 3.4.

3.3 LASSA Analysis

The LASSA detectors were used to detect the charged particles emitted from the collisions. The double-sided silicon strip detectors (DSSDs) are used primarily to determine the position of the charged particles while the cesium iodide (CsI(Tl)) detectors provide a very accurate determination of their energies. By using both detectors in the dE-E method, isotopic information can be resolved. Therefore a very careful calibration must be performed on the LASSA system to maximize the possible precision. Care is required when dealing with multiple hits and position matching between the DSSD and CsI crystals.

3.3.1 LASSA Calibrations

The calibration method for the LASSA telescopes follows a stepwise procedure: first the DSSDs are calibrated, then the CsI are calibrated. The CsI electronics demonstrate a non-linearity at large channels which should only affect helium particles with the highest energies, which contribute only minimally to the analysis. The Si electronics are non-linear at low channels, but a recent analysis in Ref. [3] by Mike Youngs shows only a very small effect in the non-linear region, so it should not have a large adverse effect in the calibration for this data.

3.3.1.1 Silicon Calibrations

The silicon strips were calibrated using a ^{228}Th source, which emits alpha particles at five different energies, from 5.42 MeV to 8.78 MeV. Because of the gain used on the Si detectors in this experiment, the highest alpha energy at 8.78 MeV was generally not visible, so only four alpha energies were used to set the slope of the Si energy calibration. All emitted alphas

Table 3.1: Initial energies of alpha particles emitted by the ^{228}Th source and the calculated energies seen by the Si detector after accounting for losses through intermediate materials.

Energy at Emission (MeV)	Energy After Losses (MeV)
5.42315	5.0509
5.68537	5.3268
6.28808	5.9532
6.77830	6.4616
8.78486	8.5210

lose energy in the 50 μg/cm^2 gold source window and the aluminized mylar foil and 1 μm thick Si dead layer on the face of the LASSA telescope: the energy losses due to each of these materials must be calculated to determine the final energy detected by the Si strips. The initial energies of emitted alphas and the final alpha energies detected in the Si detector are shown in Table 3.1. The program LISE++ was used to calculate all energy losses and deposited energies [49]. The ^{228}Th source calibration data from a single Si strip is shown in Figure 3.22.

Because the four available alpha energies are relatively close in energy, spanning only about 1.5 MeV out of the detector range of 8 MeV, the ^{228}Th source data could not reliably produce the linearity and offset of the calibration, giving some doubt to the Si calibration at low energies. To correct this problem, the punchthrough point of protons was used. The highest energy protons that are fully stopped by the CsI detectors deposit 146.8 MeV in the 6 cm CsI crystals, which corresponds to 0.51 MeV deposited in the Si strip. This punchthrough point is very well defined in the PID and was used to verify the Si calibration, as well as to correct the calibration if necessary.
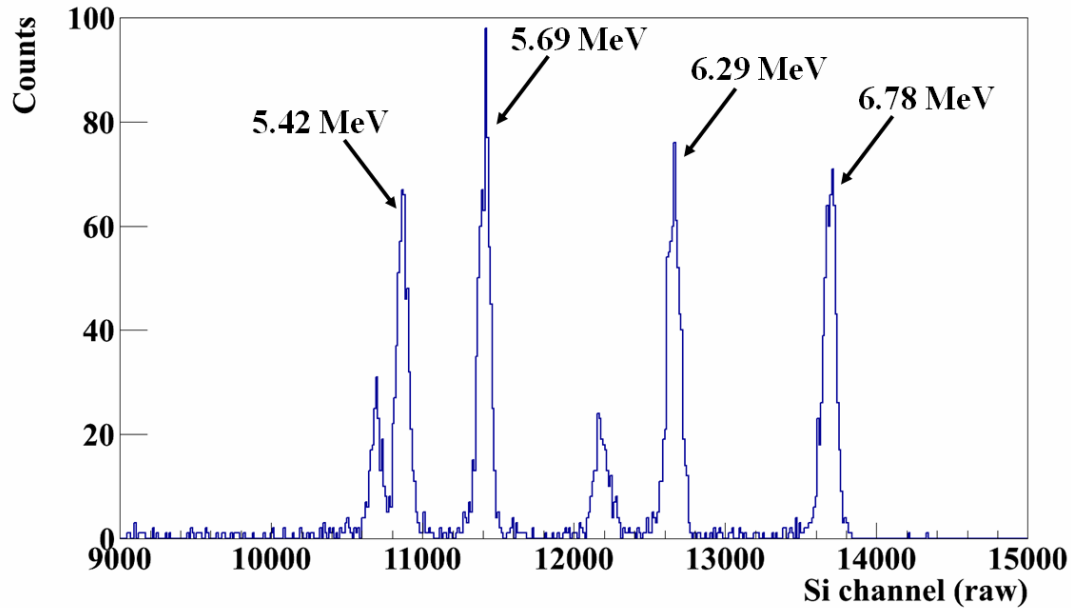
Figure 3.22: A single uncalibrated Si strip with data from the ^{228}Th source calibration run. The four sharp peaks are used to calibrate the Si detector.

3.3.1.2 Cesium-Iodide (CsI(Tl)) Calibrations

The CsI crystals were calibrated using information from the LISE++ computer program [49]. For energies deposited in the Si detector, LISE calculates the initial total energy of the particle and the amount that was deposited in the CsI crystal, assuming that the particle was stopped in the 6 cm length of CsI. This curve is well-defined for regions where the Si energy varies quickly along with the CsI energy, corresponding to low total energies of particles that deposit more than 2 MeV in the Si detector. An example fit is shown in Figure 3.23 after calibration, where the red line is the polynomial fit to a LISE calculation for the proton PID line, good down to 2 MeV in the Si energy.

At larger kinetic energies, the Si energy deposited flattens while the CsI energy increases dramatically: this region does not allow for a precise calibration using LISE. Thus, the low region of the CsI energy range is fit to the dE-E curve as defined by the Si, while the
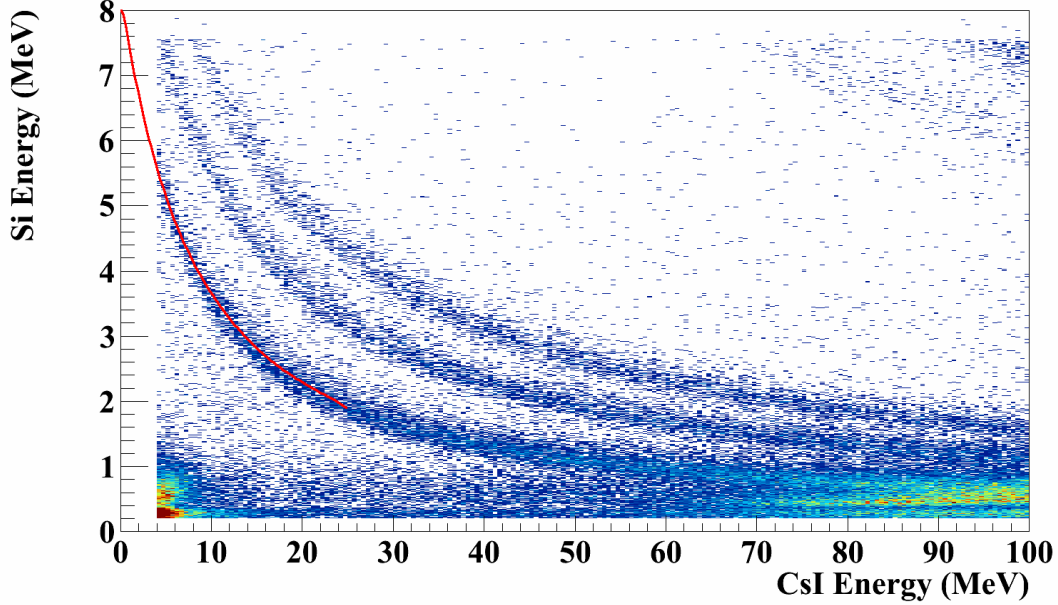
Figure 3.23: An example calibrated PID from a single CsI crystal. The LASSA dE-E curve as calculated by LISE for protons is fit to a polynomial down to Si energies of 2 MeV; this polynomial fit is shown in red.

higher energies are once again set using the proton punchthrough point of 146.8 MeV. The punchthrough point was identified by first drawing a gate around the proton PID line and examining the CsI energies of the events within that gate. An example of the resulting spectrum is shown in Figure 3.24. The punchthrough point was defined as the half-height on the shoulder, found by fitting the end of the spectrum with a curve of the form

$$Counts = \frac{ax + b}{1 + e^{(x-c)/d}} + fx + g \tag{3.19}$$

where c is the half-height on the shoulder. Each crystal was fit individually and a linear scale applied to match the punchthrough point to 146.8 MeV. The CsI energies for hydrogens with higher mass (deuterons with A=2 and tritons with A=3) were further scaled by their punchthrough points: deuterons and tritons were scaled linearly to set their punchthrough
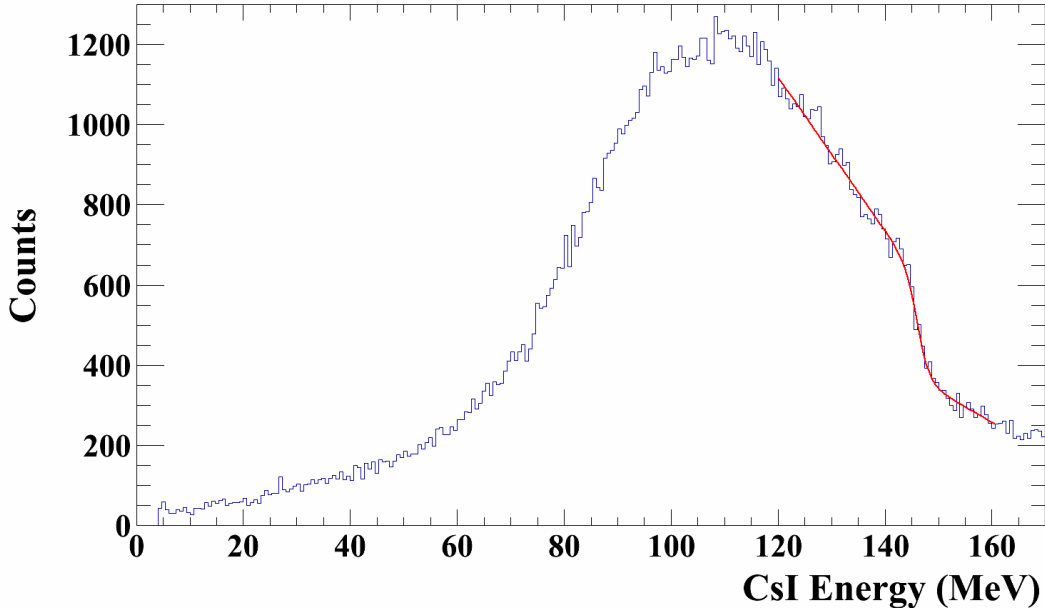
Figure 3.24: CsI energies in one crystal, gated on the proton PID line. The red line is the shoulder fit using Equation 3.19.

Table 3.2: The punchthrough energies of hydrogen particles in a LASSA CsI crystal.

Particle Species	Kinetic Energy (MeV)
proton	146.8
deuteron	195.8
triton	232

point to the values shown in Table 3.2. Because only a partial range of energies were detected for helium particles, the helium PID lines could not be adjusted for the punchthrough point, so the proton calibration was used for those CsI energies.

Particles with Z>1 are known to ionize the CsI crystals differently than hydrogen isotopes. From previous experiments Ref [50], we know that the light output for protons, deuterons, and tritons depends linearly on energy. For protons, we can write

$$L = \frac{E_p - b}{a} \tag{3.20}$$

Table 3.3: Fitting parameters to account for the light output produced by different particles in the CsI.

Z	a	b	c	d
1	0.2010	-0.9587		
2	0.1696	4.575	0.3380	-0.05772

where L is the light output of the CsI energy, E_p is the energy calibration for protons, and a and b are empirical fit parameters.

An earlier experiment determined the relationship between light output and deposited energy for more highly charged particles; because we are using the same CsI crystals, we can assume that the same relationships hold between light output and energy deposited in the crystal. Since helium particles are the only particles detected with Z>1, we need only one more equation to account for the ionization of Z=2 particles

$$E_{He} = aL + bA^c(1 - e^{dL}) \qquad (3.21)$$

where L is determined from the proton parameters, as in Equation 3.21, A is the mass number of the isotope, and a, b, c, and d are once again fit parameters. The variables used in this correction can be found in Table 3.3 from Ref. [50].

3.3.2   Event Reconstruction

Not only charged particles, but also electronics noise can create Si and CsI signals. Most of the noise can be removed from analysis by employing a software cut unique to each channel; generally the cut is low enough that it does not interfere with the hydrogen PID line. In some portions of the experiment, the noise levels were higher and interfered with proton identification, so a higher Si energy cut was applied. This is accounted for in the P_t/A vs.

Y_{lab} coverage discussed in Section 5.2 or, if the Si strip is severely undercounting as a result of the noise, dropped entirely.

Some Si detector hits produced pulses so large that they bled across the interstitial gap and a portion of the pulse was registered on the neighbor. To treat these events, a gluing procedure was followed that can add back the neighbor's lower energy to the higher energy of the hit strip. If a strip registers at least 3% of the energy read by its neighbor, but not more than the neighbor's energy, then the hit is removed from that strip and its energy is added to the neighboring strip's energy. This process "glues" together the split energies caused by the pulses that cross the interstitial gaps.

To identify if a hit is unique, a pixelation routine is followed. First for a given hit, the hit strips are identified from the front and back faces of the Si telescope. Particles deposit similar amounts of energy to each side of the DSSD, so the two strip energies should have similar values, following the conditions:

$$\text{if } E_{front} < 3.0 MeV, \ |E_{front} - E_{back}| < 0.4 MeV \tag{3.22}$$

$$\text{if } E_{front} \geq 3.0 MeV, \ \frac{|E_{front} - E_{back}|}{E_{front}} < 0.1 \tag{3.23}$$

If the energies of the two sides match the appropriate condition, the CsI crystal backing that hit location is checked. If there is no CsI hit, the hit is removed. If two or more Si pixels are hit in front of a single CsI crystal, it means that more than one particle hit the crystal during the event and the multiple hits cannot be distinguished, so all hits within that quadrant are discarded. This corresponds to a loss of about 10% of particles in the forward most telescope and 4-7% of particles in all other telescopes. The hits that have a unique match between the two Si faces with reasonably close energies and that register in the CsI crystal backing that

location are accepted as hit pixels in the event.

All pixel hits are then examined to identify charged particles based on the dE-E PID line formed by the calibrated Si (E_{front}) and CsI energies. To allow for easier selection of particles, the PID gates are drawn on a straightened PID plot, formed by translating the Si and CsI energies

$$PID_{straight} = x \cdot \ln(300) - \ln(x \cdot E_{front}) - \left[(x - 1) \cdot \ln\left(E_{CsI} + 0.5 \cdot E_{front}\right)\right] \quad (3.24)$$

where

$$x = (1.825 - 0.0072 \cdot E_{front}) \quad (3.25)$$

When $PID_{straight}$ is plotted against E_{CsI}, the results are straight vertical lines corresponding to each particle species, as seen in Figure 3.25. The largest value in the straightened PID plot corresponds to protons, followed by deuterons and tritons at lower values. Any hit that falls within those gates is labeled as that particle. Thus in further analysis steps, any hits within the proton gate are considered protons, in the deuteron gates are considered deuterons, and in the triton gate are considered tritons. The PID gates for ^{3}He and ^{4}He are drawn directly from the dE-E PID plot, since they are well separated.

Finally, the total energy of the pixel hit is calculated by summing back in the energies lost to intermediate materials between the collision event in the target and the LASSA telescope, including losses within the LASSA telescope, as calculated using the LISE++ computer program [49]. The thicknesses used in this calculation are summarized in Table 3.4. This process starts with the measured CsI energy and adds in the energy lost to the aluminized mylar foil, then adds in the measured energy in the Si detector. Next the losses attributed to the Si dead layer, the second mylar foil, and the SnPb foils are added. Finally, a correction is
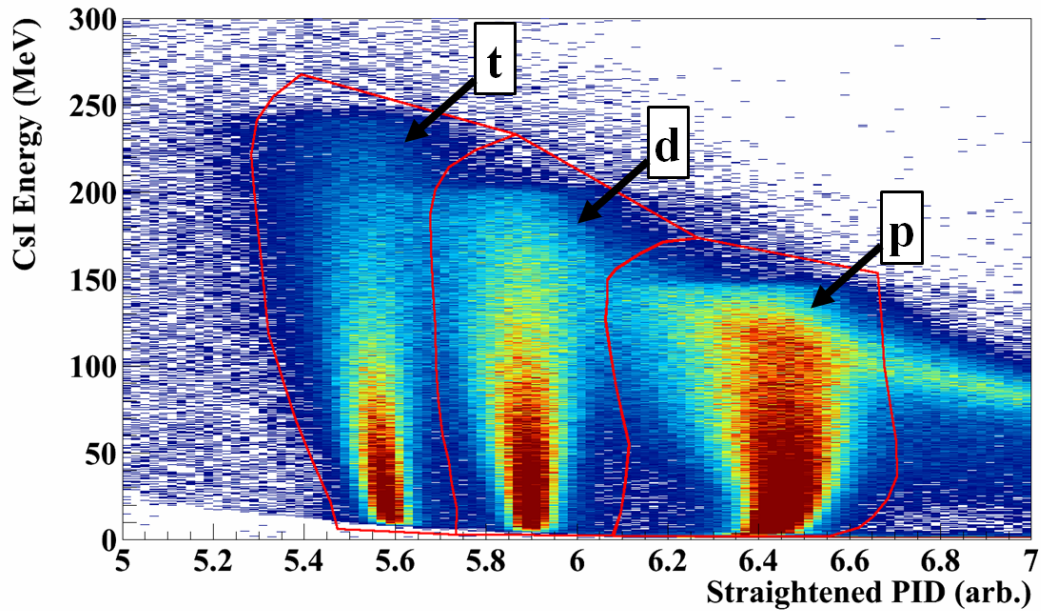
Figure 3.25: The straightened LASSA PID for hydrogen isotopes. Analysis gates are shown in red.

made for the energy lost to half of the target, under the assumption that the collision event occurred at the center of the target. An effective thickness of the target is calculated as $t_{1/2}/cos\theta$ because the target is arranged to face the beam and not the detector, so particles detected at more backward angles traveled through a larger thickness of the target.

Table 3.4: Thicknesses of materials attributable to energy losses between the collision event and detection in the LASSA Si and CsI detectors.

Material	Thickness (mg/cm^2)
Half ^{112}Sn target	2.49
Half ^{124}Sn target	2.705
SnPbSb foil	16.69284
Al	0.02
Mylar	0.24543
Si Dead layer	0.2321

89
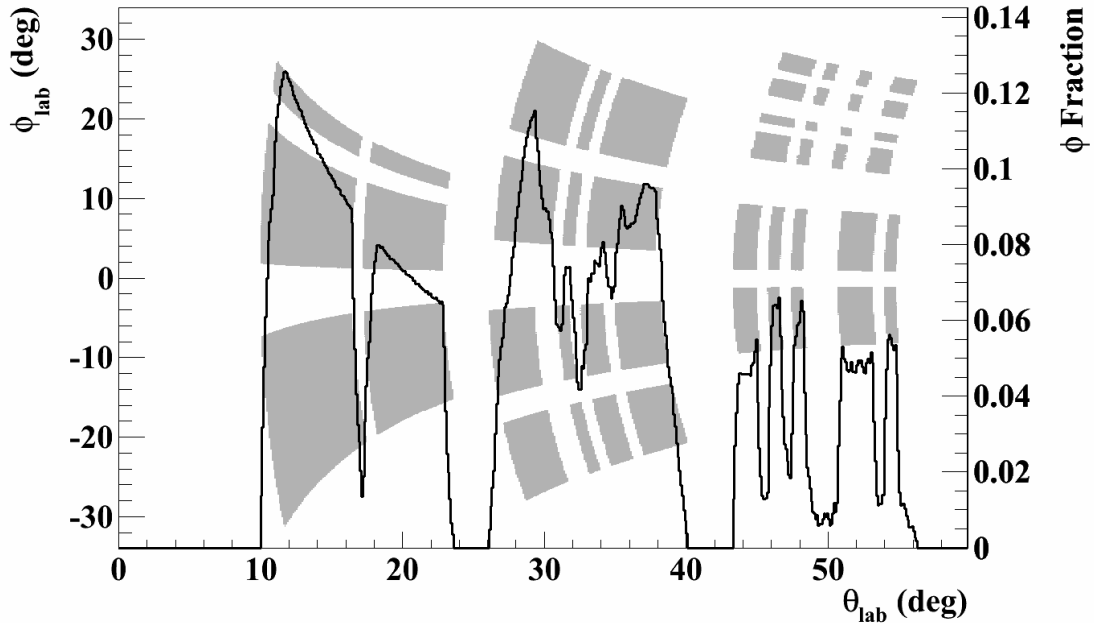
Figure 3.26: Azimuthal coverage of the LASSA Array in the Lab frame for ^{48}Ca+^{124}Sn. The shaded region shows the positions of the LASSA telescope in the lab polar angle (θ_{lab}) and azimuthal angle (ϕ_{lab}). The solid line shows the values of f_ϕ as a function of θ_{lab}.

3.3.3 Proton Efficiencies

3.3.3.1 Geometric Efficiency

The geometric coverage for charged particles are calculated in the same way as for neutrons, as detailed in Section 3.2.3.3.

As in the NW Array, the LASSA Array does not cover the full azimuthal direction, so corrections must be made for the fractional azimuthal coverage, f_ϕ, for a given polar angle θ. The azimuthal f_ϕ is shown in Figure 3.26 for the ^{48}Ca+^{124}Sn system. The different beam-target combinations have different f_ϕ as some detectors were debugged throughout the experiment and only became usable after a change in beam or a change in target. The ^{48}Ca+^{124}Sn system had the fullest coverage, since it was run last.

3.3.3.2 Detector Efficiencies

A CsI crystal can only measure energy of a charged particle accurately if it is the only particle detected by that crystal at a given time. If two or more particles enter a single crystal, their energies will be summed together and it is impossible to determine what fraction of the summed energy belonged to each constituent. Therefore, all cases where more than one particle hits an individual crystal must be thrown out, regardless of other analysis cuts: if the particles came in from the correct pixel, are above analysis thresholds, lie within the particle identification band, or so on.

If the probability for a single CsI crystal to register a hit during any given event is relatively low, we can assume that the distribution of hits in that crystal obeys Poisson statistics. In this case, the probability for number k particles to be detected by a single crystal in an event is

$$P(k) = \frac{\lambda^k e^{-\lambda}}{k!} \tag{3.26}$$

where λ is the average number of particles observed in the crystal per event. The fraction of times that the crystal sees at least one particle per event, the fractional hit fraction, r, can be determined using the equation

$$r = P(k \geq 1) = \sum_{k}^{\infty} \frac{\lambda^k e^{-\lambda}}{k!} \tag{3.27}$$

Given that $P(k \geq 0) = 1$, then

$$e^{-\lambda} = 1 - r \tag{3.28}$$

The CsI detection efficiency ϵ_{CsI} is the probability to detect only one event divided by the average number of the events, so $\epsilon_{CsI} = \frac{P(k=1)}{\lambda} = e^{-\lambda} = 1 - r$.
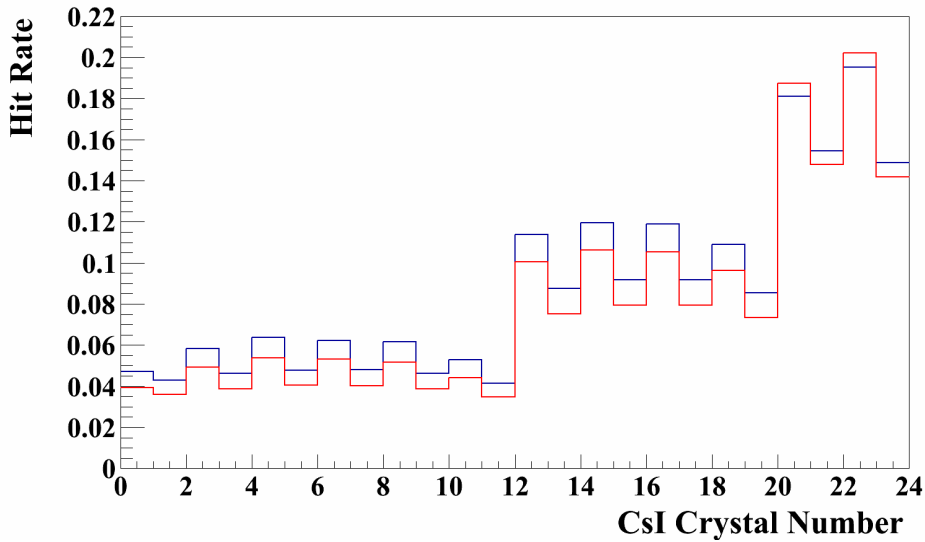
Figure 3.27: The average occupancy of each CsI crystal for ^{48}Ca+^{124}Sn. The crystal number index is equal to (4·Telescope ID) + CsI ID; in general, the larger crystal indices are more forward. Even-numbered crystals are located more forward of odd crystals in a given telescope. The blue line corresponds to the central event occupancy rate, the red line corresponds to the mid-peripheral event occupancy rate.

The hit rate r was determined for each crystal per beam-target combination and centrality cut, found as the total occupancy of a single crystal divided by the number of central or mid-peripheral events, and is assumed to be independent of particle isotope. The most forward crystals have a hit rate of up to 20% for both centrality cuts and the most backward crystals have a hit rate as low as 3% as seen in Figure 3.27. Then the efficiency for each crystal is as low as 80% for forward crystals and high as 98% for backward crystals. The charged particle spectra were corrected for the calculated CsI detection efficiencies.

The Si strips should also have a detection efficiency. Multiple hits are not a concern since the Si detectors are highly segmented, but they can have significant dead time as the signals from each hit are processed. In the later experiment E09042, a pulser was set up during the data runs to evaluate the contribution of dead time to the Silicon efficiencies, but this was unfortunately not done for the present experiment. The Si efficiencies are estimated

92

from the E09042 analysis. In E09042, the efficiency was found to correlate very strongly with beam energy, and therefore with the charged particle multiplicity N_C detected in the Miniball. The Ca+Sn collisions in the present analysis have values of N_C that are almost identical, if not slightly lower, than the 50 MeV/A beam energy E09042 Sn+Sn data with almost identical Miniball setups. Therefore, the values of silicon efficiency for the 50 MeV/A Sn+Sn data were used as an estimate for the current Ca+Sn data, with the lowest efficiency calculated at 95% [3]. Because this efficiency was not measured directly, it was included as a systematic error on the upper bound only for the charged particle spectra. The resulting systematics are discussed in Section 3.4.

The last remaining correction to account for in the charged particle detection is the background. In the LASSA PID plot (Figure 3.28) this is seen as a dark blue "haze" behind the brighter, sharp PID lines that correspond to the charged particles. It can be surmised that the haze extends throughout the spectrum and contributes some counts to the charged particles. A simple procedure was followed to estimate the contribution of the background to the charged particle lines using the straightened PID spectra, formed by Equation 3.24.

As in Figure 3.25, the particles in Figure 3.29 with a larger value of $PID_{straight}$ are the lighter particles. Between the two helium isotopes on the far left and the three hydrogen isotopes on the right is a gap where no charged particle should register; any hits in this area can be assumed to be the detected background in the LASSA telescope. Since we are unable to determine otherwise, the number of background counts is assumed to be a constant for all values of $PID_{straight}$. The fraction of the background behind each PID line is then:

$$f_{bkgd} = \frac{background}{counts} \qquad (3.29)$$
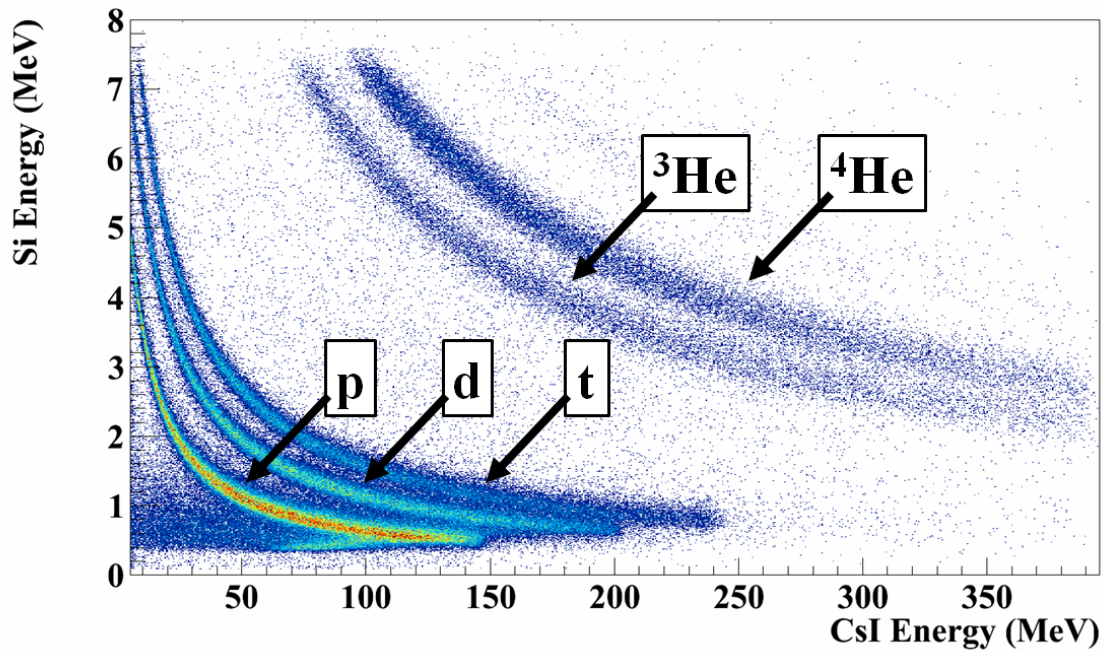
Figure 3.28: Full PID plot for one CsI crystal. The sharp, brightly colored lines correspond to charged particles. The "haze" of dark blue counts scattered throughout are background hits.
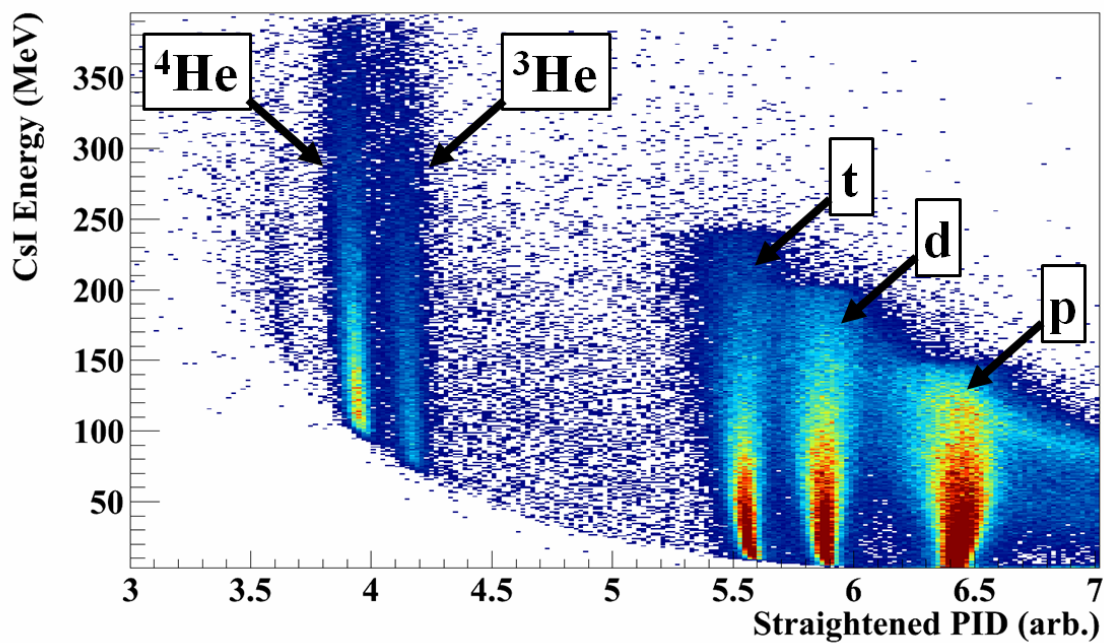
Figure 3.29: The straightened LASSA PID for hydrogen and helium isotopes.

and the fraction of events in the PID line that are correctly identified as charged particles
is:

$$f_{charge} = \frac{counts - background}{counts} \qquad (3.30)$$

To correct each PID line for the presence of background particles, one needs only multiply
by the correction factor f_{charge}. This fraction was determined for each hydrogen and helium
isotope in each crystal individually, gated on the two centrality cuts used and for all of the
beam-target combinations.

Since the background is assumed to be relatively constant throughout the CsI energy, the
correction factor from each particle was used across a span of CsI energies. The correction
factor from the proton line was used for $E_{CsI}<150$ MeV, from the deuteron line for $E_{CsI}<195$
MeV, from the triton line for $E_{CsI}<230$ MeV, and from the alpha line for $E_{CsI} \geq 230$ MeV.

3.4   Systematic Errors

Estimations of the systematic errors were calculated as follows. For charged particle spectra,
as mentioned in Section 3.3.3.2, the detection efficiency of the Si strips could not be calculated
because the relevant information was not collected during the experiment. This detection
efficiency was estimated as 5% of the value determined in experiment E09042 performed
immediately after this one, and was included only as an upper error bound on the charged
particle data (hydrogen and helium isotopes).

There are three sources of error in the neutron data, fully described in Sections 3.2.3.1,
3.2.3.2, and 3.2.3.4. The contributions from each to the systematic error are listed in Table
3.5. The three contributions to the systematic error are added in quadrature to achieve the
total systematic error for neutron spectra at approximately 13% across all values of P_t/A.

Table 3.5: Contributions of uncertainties in the neutron efficiencies to the neutron systematic error.

Contribution to the Systematic Error	Uncertainty in Value (%)	Uncertainty in Correction (%)	Average Value of Systematic Error contribution across P_t spectra (%)
Detection Efficiency	10	10	10
Background Scattering	10	3	3
PV Array Efficiency	1.5	1.5	1.5
Total Systematic Error			13

Chapter 4

Calculations

The observables measured in this experiment are compared against those obtained from Improved Quantum Molecular Dynamics (ImQMD-Sky) calculations. ImQMD-Sky contains many parameters that are used to describe heavy-ion collisions (HICs). Many of those parameters have been chosen to reproduce empirical data. However, some parameters governing the isospin dependence of the collision dynamics are poorly constrained by experimental data. By measuring specific experimental observables predicted to be sensitive to the poorly constrained values of physics inputs to the calculations, the models can be modified to provide a more accurate description of the collision dynamics and hopefully a better description of the effective interactions used within the model.

ImQMD-Sky [1] attempts to describe what happens in HICs by calculating the position and momentum vectors of each nucleon as a function of time using molecular dynamics. Since molecular dynamics calculates the nucleonic equations of motion throughout the collision, it is possible to calculate the formation of clusters, which are bound by the mutual interactions of nucleons within them. In order to calculate the potential, the nuclei involved in the collision are written as an N-body wavefunction formed as the product of the individual nucleon wavefunctions taken as Gaussian wave packets. However, in the evolution of these wavefunctions, the phase space widths of the Gaussian wave packets are held fixed as a function of time. Motivated in part by the Ehrenfest theorem, the centroids of these Gaussians move classically, subject to the self-consistent mean field potential calculated using the nucleon

positions and Skyrme effective interactions, and also scatter due to the residual interactions. Generally, the nucleonic effective potentials can be varied to determine the ones that best reproduce the experimental observables. Collisions between individual nucleons have an interaction probability given by experimental cross sections, but modified approximately by Pauli blocking and in-medium effects. The algorithm to compute cluster production is also approximate. When the wave packets of two or more nucleons overlap with relative positions less than $R_0 = 3.5$ fm and relative momenta less than $P_0 = 250$ MeV/c, those nucleons are considered to be coalesced into a cluster. The calculation continues through time steps until an end time set by the user, typically corresponding to the point at which the colliding nuclei and produced particles are again fully separated and the values of the observables stabilized.

In the calculations described below, the mean field potential is derived from the potential energy density u that includes the a local energy density (u_{loc}) and an energy density from a momentum-dependent interaction (u_{md}):

$$u = u_{loc} + u_{md} \tag{4.1}$$

Here u_{loc} is adopted from a Skyrme-like energy density, which differs from those used in other transport models in that it can describe properties of nuclear structure. This formulation generally removes the nucleon spin-orbit interaction as it is negligible at the high incident beam energies used in most HICs. The form of this local energy density is written as

$$
\begin{aligned}
u_{loc} = \frac{\alpha}{2}\frac{\rho^2}{\rho_0} + \frac{\beta}{\eta+1}\frac{\rho^{\eta+1}}{\rho_0^\eta} + \frac{g_{sur}}{2\rho_0}(\nabla\rho)^2 + \frac{g_{sur,iso}}{\rho_0}[\nabla(\rho_n - \rho_p)]^2 \\
+ A_{sym}\rho^2\delta^2 + B_{sym}\rho^{\eta+1}\delta^2
\end{aligned}
\tag{4.2}
$$

The coefficients α, β, η, g_{sur}, $g_{sur,iso}$, A_{sym}, and B_{sym} can be obtained directly from the standard Skyrme parameters t_0, t_1, t_2, t_3, x_0, x_1, x_2, and x_3 [51]. A_{sym} and B_{sym} depend on the specific set of Skyrme parameters used in the calculation and are used to describe local effects of the symmetry energy. The asymmetry, δ, is the difference in proton and neutron density (ρ_p and ρ_n, respectively)

$$\delta = \frac{\rho_n - \rho_p}{\rho_n + \rho_p} \approx \frac{N - Z}{A} \tag{4.3}$$

In Equation 4.1, a momentum-dependent energy density, u_{md}, is used that is derived from a Skyrme-like momentum-dependent interaction density

$$u_{md} = u_{md}(\rho\tau) + u_{md}(\rho_n\tau_n) + u_{md}(\rho_p\tau_p)$$

$$= C_0 \int d^3p d^3p' f(\vec{r},\vec{p}) f(\vec{r},\vec{p'})(\vec{p} - \vec{p'})^2 \tag{4.4}$$

$$+ D_0 \int d^3p d^3p' \left[f_n(\vec{r},\vec{p}) f_n(\vec{r},\vec{p'})(\vec{p} - \vec{p'})^2 + f_p(\vec{r},\vec{p}) f_p(\vec{r},\vec{p'})(\vec{p} - \vec{p'})^2 \right]$$

where $f(\vec{r},\vec{p})$ are the nucleon phase space densities

$$f(\vec{r},\vec{p}) = \sum_i \frac{1}{(\pi\hbar)^3} exp[-(\vec{r} - \vec{r_i'})/2\sigma_r^2 - (\vec{p} - \vec{p_i'})/2\sigma_p^2] \tag{4.5}$$

and C_0 and D_0 are coefficients determined from the standard Skyrme parameters

$$C_0 = \frac{1}{16\hbar^2} \left[t_1(2 + x_1) + t_2(2 + x_2) \right] \tag{4.6}$$

$$D_0 = \frac{1}{16\hbar^2} \left[t_2(2 + x_2) - t_1(2 + x_1) \right] \tag{4.7}$$

Note that u_{md} depends on both the position vector, $\vec{r}$, and the momentum vector, $\vec{p}$, for

each individual nucleon as it relates to all other nucleons in the reaction, based on their total phase space densities that evolve through each time step in the calculation. Further discussion of the influence of the momentum-dependence is discussed in Section 4.2.

From Equations 4.2 and 4.4, the symmetry energy $S(\rho)$ for cold nuclear matter can be expressed in terms of the parameters based on the mean-field approach used in this ImQMD-Sky calculation [1]:

$$S(\rho) = \frac{1}{3}\frac{\hbar^2}{2m}\rho_0^{2/3}\left(\frac{3\pi^2}{2}\frac{\rho}{\rho_0}\right)^{2/3} + A_{sym}\rho + B_{sym}\rho^{\eta} - \frac{1}{24}\left(\frac{3\pi^2}{2}\right)^{2/3}[3t_1x_1 - t_2(4+5x_2)]\rho^{5/3}$$

(4.8)

4.1 Symmetry Energy

For simplicity, many transport models use a form of $S(\rho)$ that depends on $(\rho/\rho_0)^{\gamma}$, where larger values of γ correspond to stiffer symmetry energy strengths. The ImQMD-Sky calculations presented here use a Skyrme description that can be connected to nuclear structure effects, which is missing when one uses the parameter γ [1]. The Skyrme sets in this analysis use parameters that fit Equation 4.8 but can be re-expressed in terms of the saturation symmetry energy S_0 and slope of the symmetry energy L. These two constants describe $S(\rho)$ via a Taylor expansion around $\rho \approx \rho_0$ with slope L and curvature K_{sym}

$$S(\rho) = S_0 + L\frac{\rho - \rho_0}{3\rho_0} + \frac{1}{2}K_{sym}\left(\frac{\rho - \rho_0}{3\rho_0}\right)^2$$

(4.9)

Larger values of L correspond to stiffer density dependencies of the symmetry energy, while smaller values of L correspond to softer density dependencies. L is the slope of the symmetry

Table 4.1: Selected parameters used in the four Skyrme sets used in this analysis [1].

Name	S_0 (MeV)	L (MeV)	K_0 (MeV)	K_{sym} (MeV)	Stiff vs Soft	m_n^*/m_n	m_p^*/m_p	m_n^*/m_p^*
SkM*	30	46	217	-156	Soft	0.82	0.76	>1
SLy4	32	46	230	-120	Soft	0.68	0.71	<1
Gs	31	93	237	14	Stiff	0.81	0.76	>1
SkI2	33	104	241	71	Stiff	0.66	0.71	<1

energy near saturation density

$$L \equiv 3\rho_0 \left(\frac{\partial S(\rho)}{\partial \rho} \right) \bigg|_{\rho=\rho_0} \tag{4.10}$$

and K_{sym} is the curvature of the symmetry energy near saturation density [52]

$$K_{sym} \equiv 9\rho_0^2 \left(\frac{\partial^2 S(\rho)}{\partial \rho^2} \right) \bigg|_{\rho=\rho_0} \tag{4.11}$$

Of 240 Skyrme parameter sets available [53], the four used in this analysis were selected because they had values of $S_0 = 32 \pm 2$MeV, $K_0 = 230 \pm 20$ MeV, and $m^*/m \sim 0.7$ and because they span the range of experimental constraints on L [1]. The parameters of each Skyrme set are summarized in Table 4.1. The quantity $S(\rho)$ is shown in Figure 4.1 for these four Skyrme parameterizations, where the soft parameterizations are shown as solid lines and the stiff parameterizations are shown as dashed lines. In the calculations presented here, SkM* and SLy4 have values of L=46 MeV, which are taken to model a 'soft' symmetry energy, or γ<1 in other transport models. Gs and SkI2 have values of L>90 MeV and are used to model a 'stiff' symmetry energy.
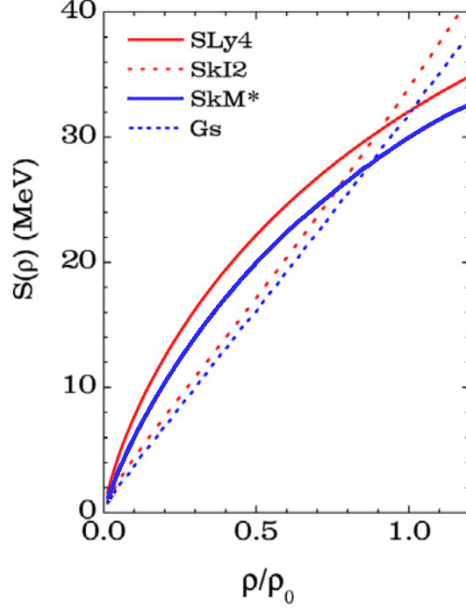
Figure 4.1: The symmetry energy strength $S(\rho)$ for the four Skyrme parameter sets used in this analysis. Soft parameterizations are shown as solid lines and stiff are shown as dashed lines. Sets with $m_n^* < m_p^*$ are shown in red and those with $m_n^* > m_p^*$ are shown in blue.

4.2 Effective Mass

The nucleon movements as influenced by the potentials from all other nucleons in the collision can be described using a mean field, which introduces a momentum dependence, which has origins in the exchange term, the intrinsic momentum-dependence, and the non-localities of the nucleon-nucleon interaction. This can be explained if we start with a Hamiltonian equation:

$$\dot{x} = \frac{\partial H}{\partial p} = \frac{p}{m} + \frac{\partial U}{\partial p} \tag{4.12}$$

By introducing the quantity $\dot{x} = \frac{p}{m^*}$, which defines the effective mass m^*, Equation 4.12 can be rewritten

$$\frac{m^*}{m} = \left(1 + \frac{m}{p}\frac{\partial U}{\partial p}\right)^{-1} \tag{4.13}$$

Or, after rearranging,

$$\frac{m^*}{m} = 1 - \frac{\partial U}{\partial E} \qquad (4.14)$$

The nucleon effective mass was introduced by Brueckner [54] to simplify the description of nucleons moving through a momentum-dependent mean field. Details of early calculations implied that $\frac{m^*}{m} \approx 0.7$ [55]. In principle, neutrons and protons could feel different momentum-dependent potentials and would therefore act with differing effective masses, giving rise to an effective mass splitting between the two nucleon species $(m_n^* \neq m_p^*)$. The effective masses used in model calculations are relatively unconstrained, by either the magnitude of the effective mass or by the sign of the splitting. In practice, if $m_n^* < m_p^*$, then high-momentum neutrons will experience a more repulsive potential than high-momentum protons and one would expect to see a relative increase in the emission of high-momentum neutrons. Likewise, if $m_n^* > m_p^*$, one would expect to see a relative decrease in high-momentum neutron emission. It is therefore expected that the high momentum region should have the greatest sensitivity to an effective mass splitting, if there is one.

Within the Skyrme sets used in these ImQMD calculations, Gs and SkM* have $m_n^* > m_p^*$ and SkI2 and SLy4 have $m_n^* < m_p^*$, as summarized in Table 4.1. These differences are shown in Figure 4.1 with the red lines depicting $m_n^* < m_p^*$ and the blue lines used for $m_n^* > m_p^*$.

4.3   In-Medium Nucleon-Nucleon Cross Sections

As introduced at the beginning of this Chapter, when two simulated nucleons collide due to the residual interaction, their collision probability may be estimated using in-medium nucleon-nucleon cross sections, σ_{NN}. The cross sections defined in the simulation are generally derived from experimental free scattering σ_{NN}^{free}, the empirical scattering measured for

two isolated nucleons. The default in-medium cross sections (σ_{NN}) used in ImQMD-Sky scale from the free cross sections σ_{NN}^{free} as [56]

$$\sigma_{NN} = \left(1 - 0.2(\rho/\rho_0)\right)\sigma_{NN}^{free} \tag{4.15}$$

The $\sigma_{nn/np}^{free}$ currently used in ImQMD-Sky are the fits to empirical data from Ref [57]. At the limit of $\rho=0$, the in-medium scattering is equal to the free scattering, but the difference in interaction probabilities increase with the local density. The in-medium components of the cross sections used in this analysis have the form from Equation 4.15.

The residual interaction is purely nuclear. The strong contribution to the neutron-neutron scattering is isospin equivalent to the strong interaction contribution to proton-proton scattering, thus the default option sets σ_{nn} equal to σ_{pp}. However, because neutrons and protons have differing isospin, σ_{np} can theoretically differ. The default formulation in this calculation allows for isospin dependence in the nucleon-nucleon scattering, which is scaled only from the measured free scattering of the same nucleon-nucleon pair,

$$\sigma_{np,nn,pp} = \left(1 - 0.2(\rho/\rho_0)\right)\sigma_{np,nn,pp}^{free} \tag{4.16}$$

As an alternative picture, a second set of calculations was performed with isospin-independent cross sections, that is

$$\sigma_{np} = \sigma_{nn} = \sigma_{pp} = \left(1 - 0.2(\rho/\rho_0)\right)\frac{2N_{np}\sigma_{np}^{free} + (N_{nn} + N_{pp})\sigma_{nn,pp}^{free}}{N_{NN}} \tag{4.17}$$

where N_{nn}, N_{pp}, N_{np}, and N_{NN} are the total number of possible neutron-neutron, proton-proton, neutron-proton, and nucleon-nucleon colliding pairs in the reaction system [56].

Thus the cross sections defined in Equation 4.17 are written as the arithmetic average of the empirical free cross sections along with the in-medium scaling as seen in Equation 4.15.

4.4   Coalescence and Light Charged Particle Formation

A major difficulty for most transport models, including ImQMD-Sky, lies in reproducing lightly bound nuclei, which are often called clusters. Copious light clusters are emitted from HICs, lowering the production of free neutrons and protons in the reaction. Since the nucleon and cluster production rates are coupled due to charge and mass conservation, if the model does not accurately reproduce cluster production, it is unlikely to accurately reproduce single nucleon spectra. One possible difficulty in reproducing the cluster yields is that there are considerable differences in the binding energies of clusters between the theoretical model and the empirical data, particularly for ^{4}He and other helium isotopes. By simple phase space considerations, such an under-prediction of the binding energies of alphas and heavier clusters will lead to over-predicting both nucleons and clusters like deuterons and tritons in QMD models and to under-predicting alphas and other strongly-bound clusters [58].

Coalescence invariant (CI) nucleon spectra can be constructed in an attempt to partially overcome this limitation. This method breaks light charged particles (LCPs) down into their constituent nucleons and adds them to the respective free spectra

$$dY_{CI}(n) = \sum_{N,Z} N \cdot dY(N, Z) \tag{4.18}$$

$$dY_{CI}(p) = \sum_{N,Z} Z \cdot dY(N, Z) \tag{4.19}$$

The CI neutron and proton spectra and CI ratios make for a more reliable comparison

between experimental results and theory calculations [40] in a way that is model independent. For the LCPs calculated in the ImQMD-Sky simulations analyzed here, Equations 4.18 and 4.19 can be rewritten as

$$dY_{CI}(n) = dY_{free}(n) + dY(d) + 2 \cdot dY(t) + dY(^3He) + 2 \cdot dY(^4He) + 4 \cdot dY(^6He) \quad (4.20)$$

$$dY_{CI}(p) = dY_{free}(p) + dY(d) + dY(t) + 2 \cdot dY(^3He) + 2 \cdot dY(^4He) + 2 \cdot dY(^6He) \quad (4.21)$$

In principle, the CI spectra could include clusters heavier than ^{6}He, if produced in the simulation, but the effect of omitting heavier clusters should be small. Generally, the heavier the particle, the smaller its yield: the most likely particles to be emitted at high transverse velocities from an HIC are those with lighter masses. This can be seen more clearly at higher momenta, due in part to the necessity of scaling the transverse momentum by $1/A$. The production of more massive particles is peaked towards positions and velocities where the nucleonic phase space densities are higher. At mid-rapidity, this primarily occurs at lower momenta and consequently the differential multiplicities of heavier fragments decay faster than for lighter fragments. At large values of P_t/A, the largest contribution to the CI neutron and proton spectra comes from deuterons. In the empirical data presented here, ^{4}He contributes an order of magnitude less to the CI spectra than do deuterons at $P_t/A = 300$ MeV/c and higher, as will be shown in Section 5.4. Measurements from past experiments have observed that LCPs heavier than ^{4}He have even smaller yields especially at high transverse momenta where we can best compare between data and calculations [59], so it is reasonable to expect that heavier clusters not measured in this experiment would contribute negligibly to the CI nucleon spectra.

4.5 Results from ImQMD Calculations: Ratios of Free Nucleons

Four Skyrme parameterization sets (Gs, SkM*, SkI2, and SLy4) were used to calculate the production of neutrons, protons, and LCPs for the two reactions, ^{48}Ca+^{124}Sn and ^{48}Ca+^{112}Sn, for both central collisions (with impact parameter b=1 fm) and mid-peripheral collisions (b=5 fm). For all Skyrme models, the spectra were calculated in a very similar method as used for the experimental data. In this analysis, P_t/A spectra were constructed to maximize the overlap of detector coverage for the six different particles measured in the experiment. The differences in the LASSA coverage seen in Figure 2.20 and the NW Array coverage seen in Figure 2.7 are exacerbated when the laboratory coordinates are translated to the center of mass frame as needed to construct E_{CM}/A spectra; using P_t/A spectra allows for minimal extrapolations between spectra of different particles, allowing for an overall smaller systematic error in the analysis. A more thorough discussion of the measured P_t/A for each particle is presented in Chapter 5.

The P_t/A multiplicity spectra are constructed as

$$\frac{dM}{d(P_t/A)d(Y/Y_{beam})_{lab}} \tag{4.22}$$

with an analysis cut for the ImQMD-Sky calculations taken around mid-rapidity data, $0.45<(Y/Y_{beam})_{lab}<0.55$, which matches well to the empirical cut at $0.44<(Y/Y_{beam})_{lab}<0.59$. The rapidity is defined as

$$Y = \frac{1}{2}\ln\frac{E+p_z c}{E-p_z c} \tag{4.23}$$

and is commonly used to describe a particle's motion along the beam axis in a more robust
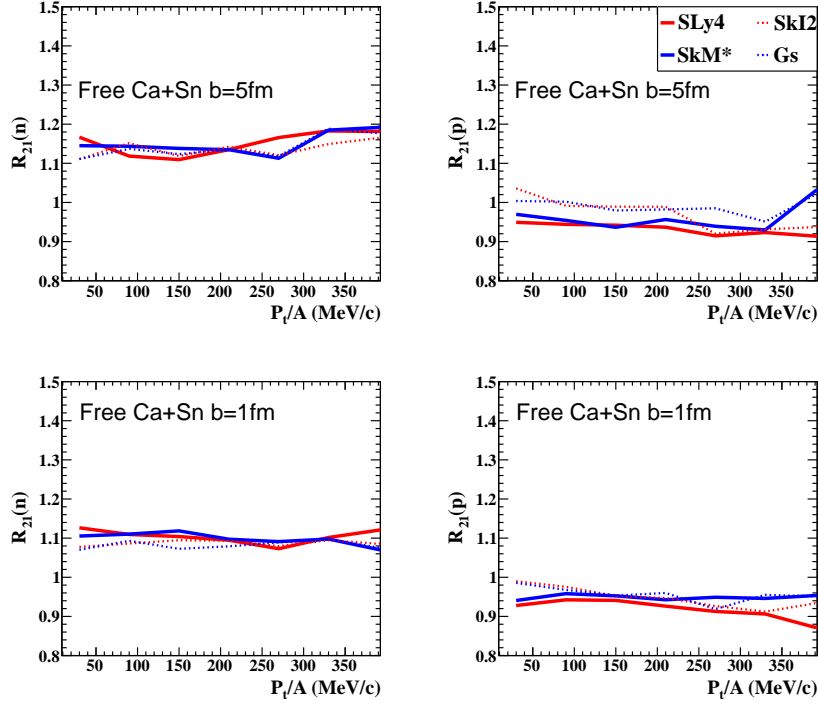
Figure 4.2: Isoscaling ratios from ImQMD-Sky calculations. Left panels: neutron isoscaling ratios, $R_{21}(n)$. Right panels: proton isoscaling ratios, $R_{21}(p)$.

way than by P_z alone. By scaling by the beam rapidity, Y_{beam}, the motions of the particles are put into perspective: nucleons with values of $Y/Y_{beam} = 1$ traveled near the beam's momentum. In the mid-rapidity region around $Y/Y_{beam} \sim 0.5$ are particles that end with momentum parallel to the beam at about half the initial beam value; previous calculations have shown that this mid-rapidity selection should pick out the overlap region between the beam and target nuclei in the asymmetric Ca+Sn reaction [60].

The first calculations presented are the isoscaling ratios in Figure 4.2: $R_{21}(n)$ are shown in the left panels and $R_{21}(p)$ in the right panels. The isoscaling ratios are written as in Equation 1.7. Keeping with convention, reaction 2 is the more neutron-rich $^{48}Ca+^{124}Sn$ and reaction 1 is the less neutron-rich $^{48}Ca+^{112}Sn$. For the rest of this Chapter, the results for central collisions (b=1 fm) are shown in the lower panels and for mid-peripheral collisions
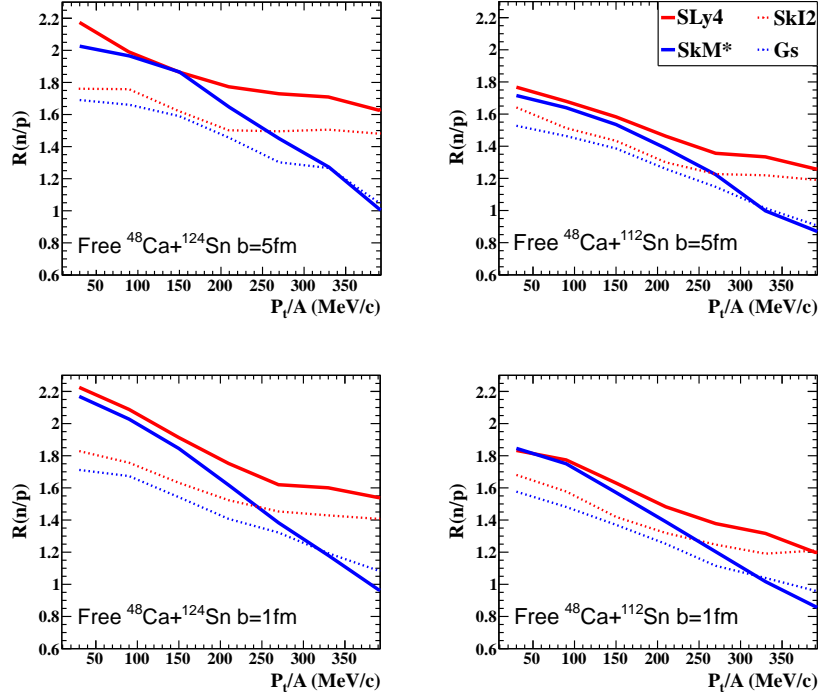
Figure 4.3: Single neutron to proton ratios, $R(n/p)$ as calculated with ImQMD-Sky.

(b=5 fm) are shown in upper panels. In this work the convention is used that calculations with $m_n^* < m_p^*$ are shown in red while those with the opposite splitting are shown in blue, and soft symmetry strengths are shown as solid lines while stiff symmetry strengths are dotted lines.

There is very little sensitivity in the calculated free $R_{21}(n)$ or $R_{21}(p)$ to either the symmetry energy stiffness or the effective mass splitting. The largest effect is the 5% increase in the $R_{21}(p)$ for the soft symmetry energy compared to the stiff symmetry energy.

The single n/p ratios, as defined in Equation 1.6, are presented in Figure 4.3. The left panels show $R(n/p)$ for ^{48}Ca+^{124}Sn and the right panels show $R(n/p)$ for ^{48}Ca+^{112}Sn. Here a sensitivity is observed to both the symmetry energy stiffness and to the effective mass splitting. At low values of P_t/A, $R(n/p)$ splits by the stiffness, with larger $R(n/p)$ values predicted by softer Skyrme parameterizations. This observation holds for both cen-
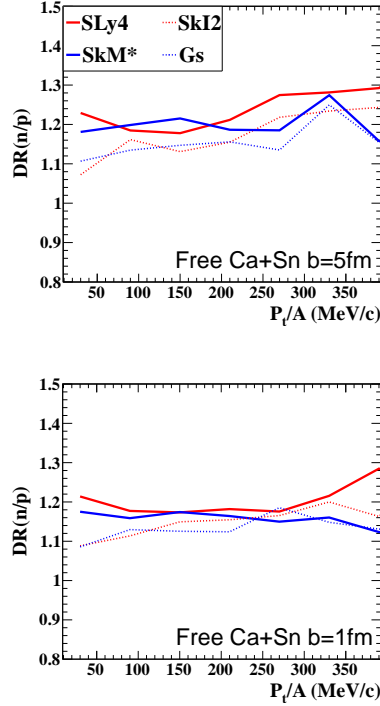
Figure 4.4: Double neutron to proton ratios, $DR(n/p)$, as calculated with ImQMD-Sky.

tral and mid-peripheral impact parameters and for both reactions. This makes sense for subsaturation densities in neutron-rich systems, where soft symmetry energies are stronger than stiff symmetry energies and therefore lead to more repulsive potentials for the excess neutrons. Additionally, this effect appears to be larger in the ^{48}Ca+^{124}Sn system, which has a greater neutron excess than the ^{48}Ca+^{112}Sn reaction system.

At values of large P_t/A, $R(n/p)$ splits primarily by m^*. The calculations with $m_n^* < m_p^*$ (red lines) lead to an increased repulsive potential of high-momentum neutrons compared to the calculations with $m_n^* > m_p^*$ (blue lines). Again, this effect is more pronounced for the more neutron-rich ^{48}Ca+^{124}Sn system. In the region $P_t/A > 300$ MeV/c, the effective mass splitting is the dominant effect in the calculations.

Finally, the neutron to proton double ratios, as defined in Equation 1.8, are shown in Figure 4.4. $DR(n/p)$ is used to cancel multiple sources of errors or uncertainties that may

be present for one particle type or for one reaction but not the other; thus the effects of the errors are minimized when taken in ratio form. Since two different particle spectra are compared between two beam-target combinations with differing values of N/Z, we still expect to see a sensitivity to the symmetry energy. For both central and mid-peripheral impact parameters, the $DR(n/p)$ is about half as sensitive to the symmetry energy stiffness or the effective mass splitting that was seen in the $R(n/p)$ calculations.

4.6 Results from ImQMD Calculations: Ratios of Coalescence Invariant (CI) Nucleons

The P_t/A spectra of CI nucleons were calculated by summing over particles produced in the ImQMD calculations up to ^{6}He, as written in Equations 4.20 and 4.21. The ratios $R_{21}(x)$, $R(n/p)$, and $DR(n/p)$ were constructed from the resulting CI nucleon spectra.

The CI isoscaling ratios $R_{21}(x)$ are shown in Figure 4.5. As observed in the free isoscaling ratios in Figure 4.2, there is little sensitivity in any of the isoscaling ratios to either the slope of the symmetry energy, L, or the effective mass splitting. The primary effects of including clusters into the ratios occur at low values of P_t/A, which makes sense since the contributions of clusters are small at high transverse momenta.

The single n/p ratios for CI nucleons are shown in Figure 4.6. The four Skyrme parameter sets remain separated by the sign of the effective mass splitting at high P_t/A; the calculations for the ^{48}Ca+^{124}Sn reaction (left panels) show a greater difference between the two pairs. Comparing to the free $R(n/p)$ in Figure 4.3, the difference among the four Skyrme sets has become negligible at low P_t/A: there is no longer a predicted splitting based on L. This is consistent with previous ImQMD calculations of n/p ratios for symmetric Sn+Sn
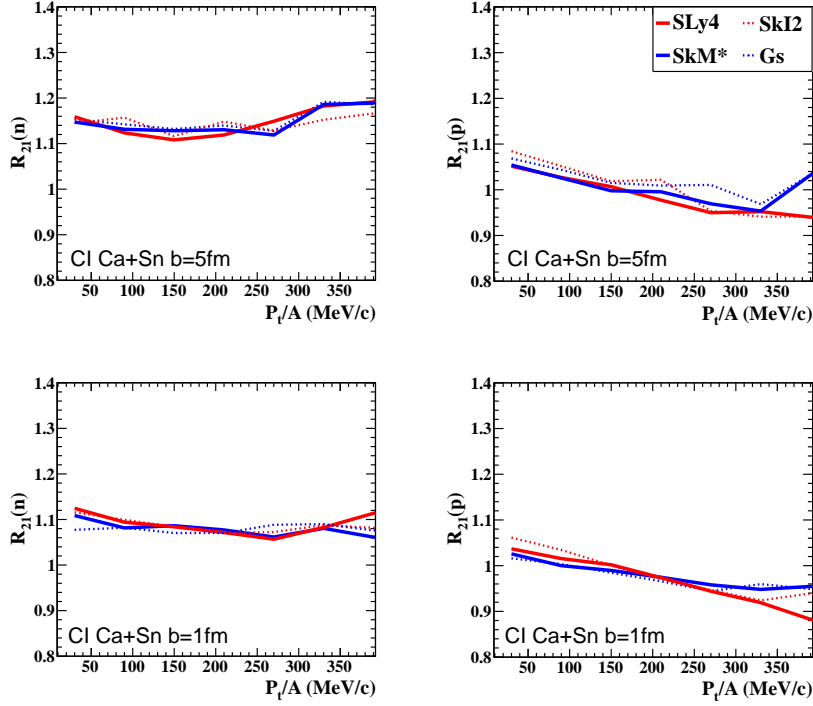
Figure 4.5: Isoscaling ratios from ImQMD-Sky calculations of CI nucleons. Left panels: CI neutron isoscaling ratios, $R_{21}(n)$. Right panels: CI proton isoscaling ratios, $R_{21}(p)$.

reactions [1] and comparisons with experimental Sn+Sn data [2]. This is not surprising since cluster contributions at low momenta are dominated by deuterons and alphas whose emissions are largely insensitive to the symmetry energy.

Finally, the $DR(n/p)$ constructed from the calculated CI nucleon spectra are shown in Figure 4.7. As observed in the CI $R(n/p)$, the sensitivity to L is no longer present at low P_t/A, while the values of the ratio at high P_t/A values remain largely unchanged from the free $DR(n/p)$ in Figure 4.4.

It appears that $R(n/p)$ is the observable most sensitive to both the stiffness and the mass splitting in this system and should be the most sensitive observable to constrain either effect from this experimental data. This is not surprising because the relative difference seen in $DR(n/p)$ should be roughly given by the percent different between the neutron-rich $R(n/p)$
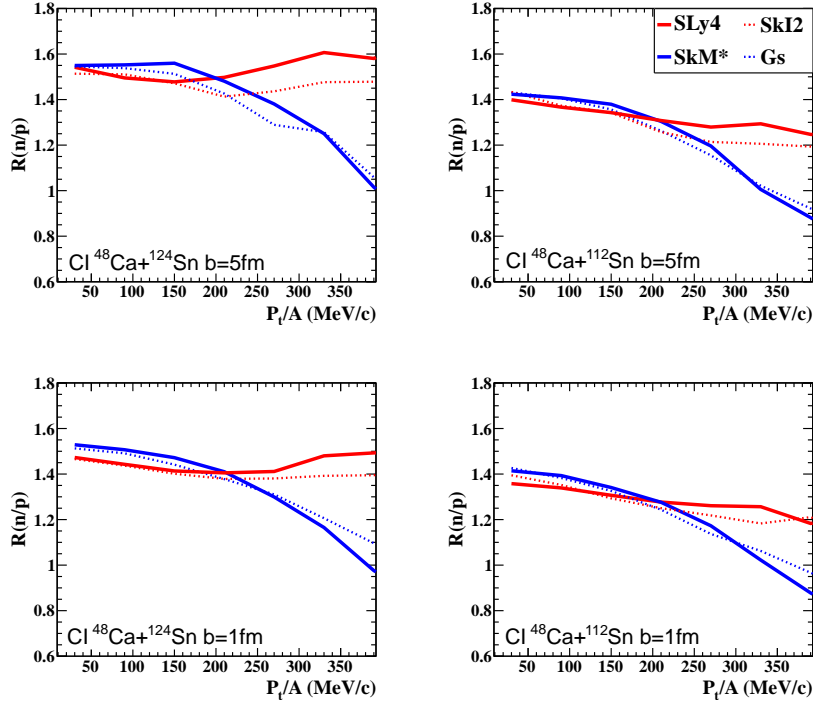
Figure 4.6: Single neutron to proton ratios, $R(n/p)$ of CI nucleons as calculated with ImQMD-Sky.

and the neutron-poor $R(n/p)$. However, previous analyses of the companion experiment $^{124}Sn+^{124}Sn$ and $^{112}Sn+^{112}Sn$ at 50 and 120 AMeV still displayed a significant sensitivity to $DR(n/p)$ at the highest center of mass energies [2,3]. In Chapter 5, both the Ca+Sn data analyzed in this work and the Sn+Sn data of the companion experiment will be compared to ImQMD-Sky calculations to get a better sense of the effects.

4.7 Results from ImQMD Calculations: Ratios of CI Nucleons for Isospin-Independent Cross Sections

To examine the sensitivity of the ImQMD-Sky calculations to the form of σ_{NN} used, calculations from two forms were compared. The calculations used to produce the free and
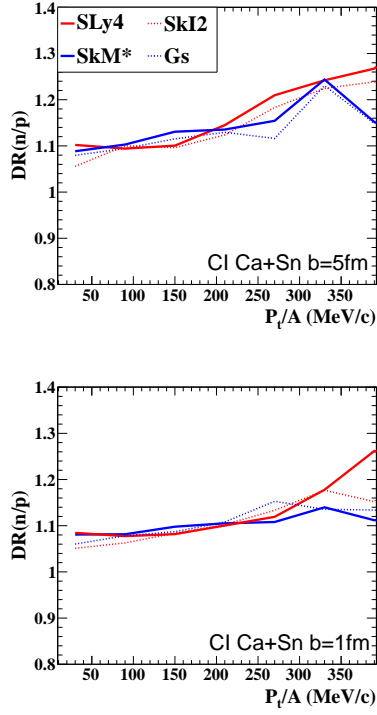
Figure 4.7: Double neutron to proton ratios, $DR(n/p)$ of CI nucleons as calculated with ImQMD-Sky.

CI nucleon ratios shown in Sections 4.5 and 4.6, respectively, use the default σ_{NN} shown in Equation 4.16, which allows for an isospin-dependent description of the nucleon-nucleon interactions in which $\sigma_{nn} = \sigma_{pp} \neq \sigma_{np}$. This assumption is tested against the isospin-independent form $\sigma_{nn} = \sigma_{pp} = \sigma_{np}$ shown in Equation 4.17; the resulting CI nucleon ratios are shown in this Section. The free nucleon ratios are not displayed for the isospin-independent cross sections, as the CI ratios have less sensitivity to uncertainties in the cluster production rates and consequently have shown better agreement between calculations and experimental data.

The isoscaling ratios for the CI nucleons produced with $\sigma_{nn} = \sigma_{pp} = \sigma_{np}$ calculations are shown in Figure 4.8. The differences from the calculated $R_{21}(x)$ using $\sigma_{nn} = \sigma_{pp} \neq \sigma_{np}$ in Figure 4.5 are slight.
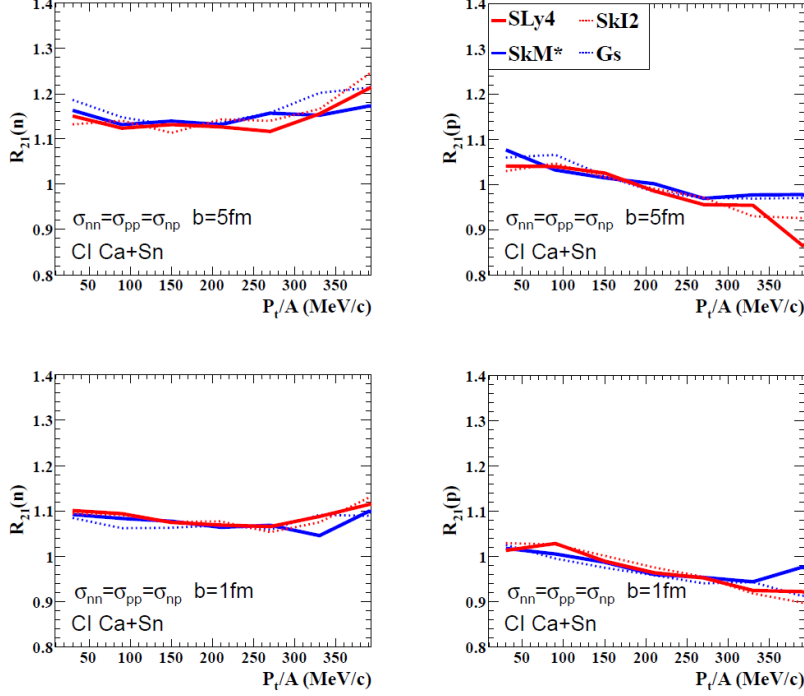
Figure 4.8: Isoscaling ratios from ImQMD-Sky calculations of CI nucleons using the in-medium cross sections $\sigma_{nn} = \sigma_{pp} = \sigma_{np}$. Left panels: neutron isoscaling ratios, $R_{21}(n)$. Right panels: proton isoscaling ratios, $R_{21}(p)$.

The n/p ratios for the CI nucleons produced with $\sigma_{nn} = \sigma_{pp} = \sigma_{np}$ calculations are shown in Figure 4.9. Here some differences with the $\sigma_{nn} = \sigma_{pp} \neq \sigma_{np}$ $R(n/p)$ in Figure 4.6 are apparent, as one might expect since the effect of changing the cross sectional forms is largest for σ_{np}. The major effect from isospin-independent cross sections appears to be an increase of $R(n/p)$ values at high P_t/A in the case where $m_n^* > m_p^*$ (SkM* and Gs parameterizations shown as blue lines). The effect is greatest at high P_t/A for the mid-peripheral ^{48}Ca+^{124}Sn reaction (upper left panel), where both parameterizations using $m_n^* > m_p^*$ increase by about 20% and the $m_n^* < m_p^*$ parameterizations (red lines) increase by about 10%. For the mid-peripheral ^{48}Ca+^{112}Sn reaction (upper right panel) at high P_t/A, both parameterizations employing $m_n^* > m_p^*$ increase by about 5% when switching to the isospin-independent form of the cross sections.
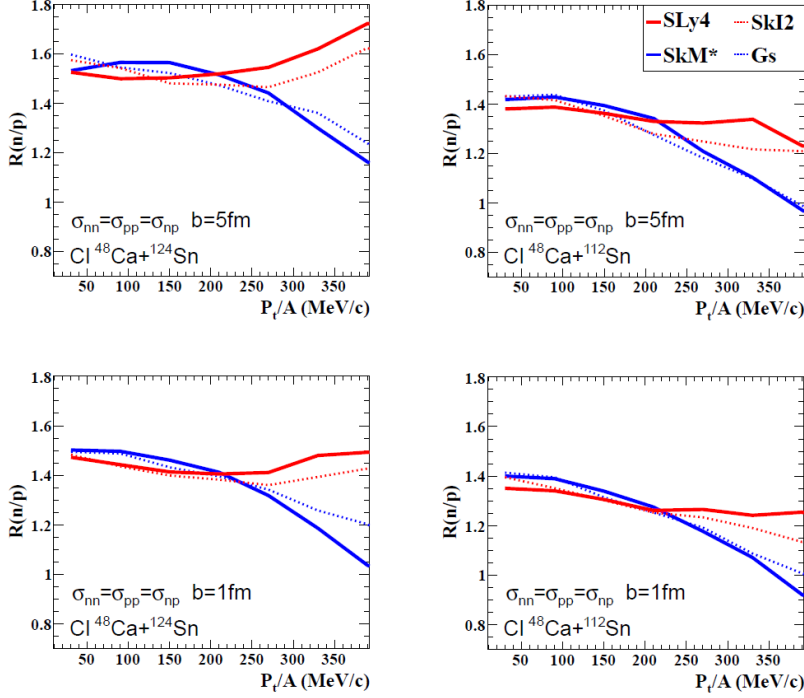
Figure 4.9: Single neutron to proton ratios, $R(n/p)$ of CI nucleons as calculated with ImQMD-Sky using the in-medium cross sections $\sigma_{nn} = \sigma_{pp} = \sigma_{np}$.

The CI $DR(n/p)$ calculated for isospin-independent cross sections are shown in Figure 4.10. The central $DR(n/p)$ (bottom panel) are relatively unchanged from the isospin-dependent results shown in Figure 4.7, while the mid-peripheral $DR(n/p)$ show a slight increase at high P_t/A consistent with the relative increase at high P_t/A for mid-peripheral ^{48}Ca+^{124}Sn n/p ratio compared to the mid-peripheral ^{48}Ca+^{112}Sn n/p ratio.

Overall the differences between the isospin-independent cross sections ($\sigma_{nn} = \sigma_{pp} = \sigma_{np}$) and the isospin-dependent cross sections ($\sigma_{nn} = \sigma_{pp} \neq \sigma_{np}$) are relatively small because both use the same density-dependent scaling (Equation 4.15) from the free nucleon-nucleon cross sections as a realistic approximation to the in-medium nucleon-nucleon cross sections. Both forms also have the same overall nucleon-nucleon collision rate, so that only the isospin-dependence of the cross sections is varied [56].
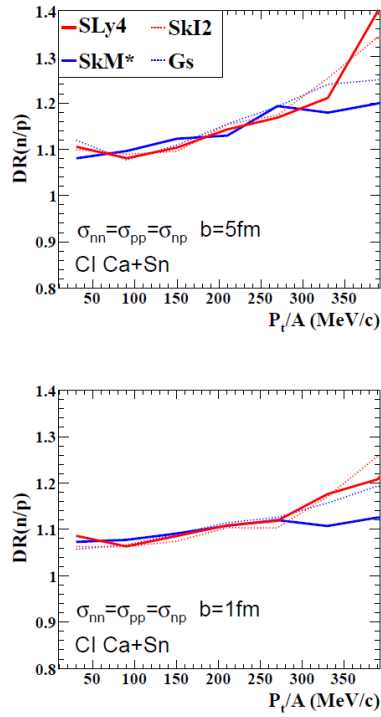
Figure 4.10: Double neutron to proton ratios, $DR(n/p)$ of CI nucleons as calculated with ImQMD-Sky using the in-medium cross sections $\sigma_{nn} = \sigma_{pp} = \sigma_{np}$.

Chapter 5

Results

5.1 Presentation of Data

To gain insight into how the experimental data vary with transverse momentum, P_t/A, and relative rapidity, $(Y/Y_{beam})_{lab}$, the data are first examined in 2D P_t/A vs $(Y/Y_{beam})_{lab}$ plots. Example plots are shown in Figure 5.1 for mid-peripheral $(0.3{<}\hat{b}{<}0.6)$ ^{48}Ca+^{124}Sn data with all calibrations and efficiencies applied to the data; the analogous plots are very similar for central $(\hat{b}{<}0.3)$ ^{48}Ca+^{124}Sn data and for both centrality cuts of the ^{48}Ca+^{112}Sn data. This Figure clearly shows the acceptance of the detectors for each particle species.

The energies of hydrogen isotopes could only be detected up to the punchthrough point of the CsI crystals, which is the maximum energy for a particle to be stopped in the 6 cm length of the CsI crystal, as described in Section 3.3.1.2. The upper detection energy for the ^{3}He and ^{4}He particles was limited by the high gain of the amplifiers used in the CsI detectors, limiting most crystals to a maximum detected energy of approximately 400 MeV. The high gain was chosen to maximize the resolution for protons, which are detected at lower energies in the CsI than the heavier isotopes.

The lower energy cuts of the charged particle spectra are likewise defined by a high gain, this time in the Si detectors as described in Section 3.3.1.1. Again the gain was chosen to maximize proton resolution, this time limiting the maximum energy in the DSSDs to about 8 MeV. This has the greatest effect in the helium isotopes, where 8 MeV energy loss in the
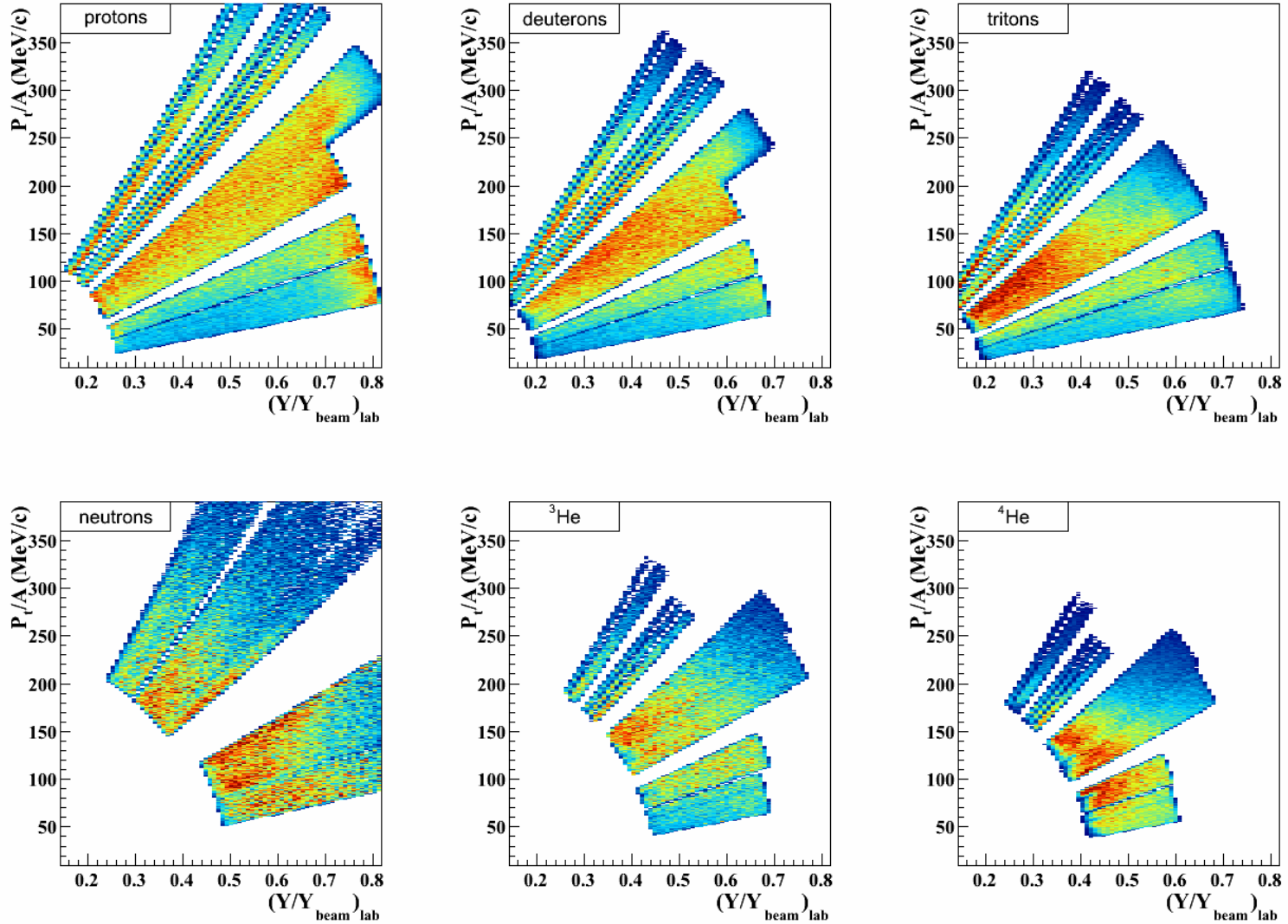
Figure 5.1: ^{48}Ca+^{124}Sn P_t/A vs. $(Y/Y_{beam})_{lab}$ plots including all efficiency corrections. Only data from mid-peripheral events $(0.3<\hat{b}<0.6)$ are shown, but the central data is similar. Panels are labeled with the species shown.

Silicon detector sets a minimum detected energy for the helium particles that corresponds to about 100 MeV in the CsI crystal. Therefore the dynamic energy range was fairly narrow for ^{3}He and ^{4}He, spanning only 110 MeV $<E_{kin}<$400 MeV.

As care was taken to obtain "clean" spectra for each individual isotope, CsI crystals that exhibited significant amounts of punchthrough particles, where tritons and deuterons overlap the proton line at high energies, were not analyzed at energies above this contamination point. This effect was greater for the more forward crystals where particles have higher emission energies and are more likely to punch through, whereas backward crystals showed little to no punchthrough effects. The analysis cut to remove punchthrough effects resulted in the "step" seen in the middle section of the 2D spectra for protons and deuterons at the transition between one set of CsI crystals to a more backward set that did not show punchthrough effects.

The energy cutoffs seen in the 2D ^{3}He and ^{4}He spectra are due to the different gains set in the CsI detector amplifiers. The crystals in the middle telescopes had the smallest gain, allowing for the widest range in detected energy of the helium particles. The most forward and most backward crystals were set with higher gains, therefore lowering the maximum detectable energies of the helium particles. In all cases, the maximum energies were well above the hydrogen punchthrough energies in the CsI, so the hydrogen spectra were not affected.

The neutron spectrum in the bottom left panel has a higher low energy cut than those seen for the charged particles because of the energy threshold set in the NW Array electronics, as described in Section 3.2.3.4, and the over-subtraction of deuterons and tritons from the NW Array PID, as described in Section 3.2.3.1.

The distribution of the particles generally looks smooth across the relative lab rapidity

and the transverse momentum. The lower number of counts at the edges of the detector faces is due to bins not fully covered, which is not corrected for in this representation of the data. It should also be noted that each panel in Figure 5.1 has a different range on the color scale, so the colors should not be compared across different particle species.

The ImQMD calculations suggest that a mid-rapidity cut, that is to say an analysis cut around $(Y/Y_{beam})_{lab} \sim 0.5$, should select the overlap region between the beam and target nuclei in the asymmetric Ca+Sn reaction. For the experimental data, a final rapidity cut from $0.44<(Y/Y_{beam})_{lab}<0.59$ was used. The lower range of the cut represents the edge of the detection at low P_t/A of the neutrons as well as the heliums, ^{3}He and ^{4}He. The upper end of the analysis gate was chosen to maximize the number of events sharing similar physics and also correlates to the upper edge of the detection range of the ^{4}He. The distribution of particles across the detectors as seen in Figure 5.1 is especially smooth within the chosen mid-rapidity region.

5.2 Free Particle Spectra

The analyzed particles are presented in P_t/A spectra, constructed in the form

$$\frac{dM}{d(P_t/A)d(Y/Y_{beam})_{lab}} \tag{5.1}$$

where dM is the number of particles within the analysis cut per transverse momentum bin, $d(P_t/A)$, and lab rapidity bin, $d(Y/Y_{beam})_{lab}$. The spectra are a function of P_t/A to show how the production varies across the detected P_t/A range. The values of transverse momenta are divided by the number of nucleons, A, to better compare different species.

The quantity dM is calculated from the number of detected particles that fall within that P_t/A, $(Y/Y_{beam})_{lab}$ bin, including all the relevant efficiencies discussed in Chapter 3, within the cuts corresponding to central or mid-peripheral impact parameters determined from the Miniball charged particle multiplicity spectra as described in Chapter 3.1. Spectra from central collisions are normalized by the total number of central events and mid-peripheral collision data are likewise normalized by the total number of mid-peripheral events. The P_t/A value for the bin is calculated as the average P_t/A value from all events within that bin, which can differ from the P_t/A value of the bin's center.

As seen in Figure 5.1, the detector arrays do not fully cover the entire mid-rapidity range, $0.44 < (Y/Y_{beam})_{lab} < 0.59$. For a P_t/A, $(Y/Y_{beam})_{lab}$ bin that is not fully covered within the mid-rapidity cut, the fractional area is calculated from a more finely-binned mask of the detector coverage for each reaction.

The calculation for the fractional coverage of each analysis bin begins with a Monte Carlo simulation of the LASSA coverage for charged particles and the NW Array coverage for neutrons. This Monte Carlo simulation creates a "mask" of the detector coverage, where a very fine P_t/A, $(Y/Y_{beam})_{lab}$ bin that has simulated counts is considered covered by the detector and empty bins are not. The simulated masks for all six analyzed particles for the ^{48}Ca+^{124}Sn reaction are shown in Figure 5.2, depicting the values of P_t/A and $(Y/Y_{beam})_{lab}$ for which we expect to see each particle. The neutrons (lower left panel) are expected to be observed in a different P_t/A, $(Y/Y_{beam})_{lab}$ region than the protons (upper left panel) because the detectors have different geometric coverages, thresholds, and efficiencies. The other charged particle species likewise have different coverages than the protons because the energy range detected differs for each species and because they are displayed and analyzed as P_t/A, which scales down the heavier isotopes more than the lighter ones.
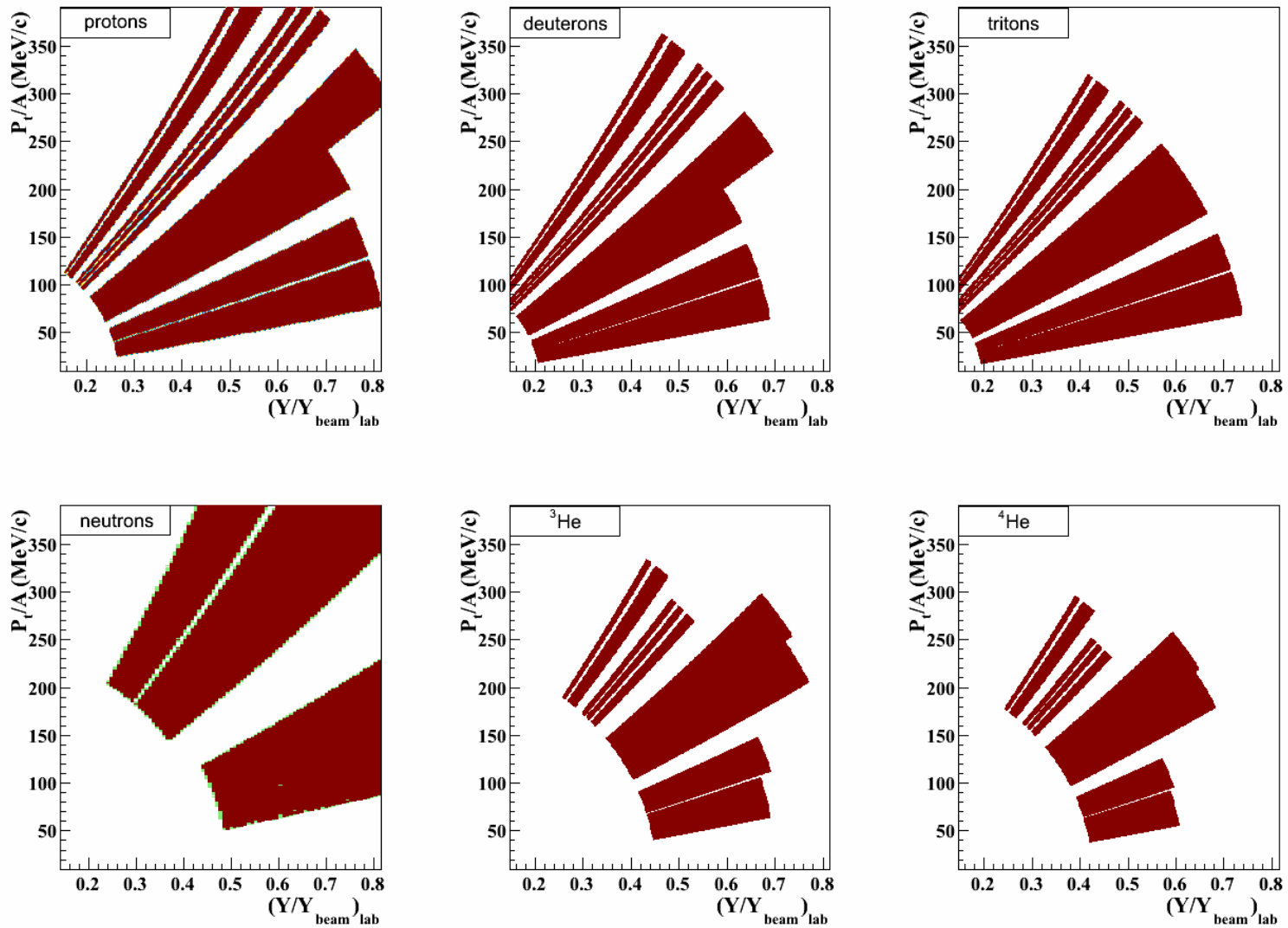
Figure 5.2: P_t/A vs $(Y/Y_{beam})_{lab}$ masks for particles produced in the ^{48}Ca+^{124}Sn Monte Carlo simulation. Panels are labeled with the species shown.

123

The mask is then used to determine the fractional bin coverage for each larger P_t/A, $(Y/Y_{beam})_{lab}$ bin, as shown in Figure 5.3. The fractional coverages were calculated for bins with width $d(Y/Y_{beam})_{lab}= 0.075$, so the fractional coverages of two adjacent rapidity bins were averaged together to determine the total coverage of the full $d(Y/Y_{beam})_{lab}= 0.15$ bin. Only bins with a total fractional coverage greater than 30% and individual fractional coverages greater than 18% in each $d(Y/Y_{beam})_{lab}= 0.075$ bin were considered, to avoid over-correcting data from bins with small area. The same process was followed for each isotope from each reaction.

The full bin area of $dP_t/A= 20$ MeV/c and $d(Y/Y_{beam})_{lab}= 0.15$ is scaled by the fractional area covered so that the quantity $d(P_t/A)d(Y/Y_{beam})_{lab}$ reflects the true area covered in the bin. Because the average P_t/A value of data within the bin was used as the P_t/A value, rather than the central P_t value of the bin, the distribution of the data within the bin is reflected in the P_t/A spectra. For fully-covered dP_t/A, $d(Y/Y_{beam})_{lab}$ bins the difference between the center value and the average value may be small, but bins where the coverage is primarily in one corner of the bin will be skewed in that direction.

The resulting spectra as calculated from Equation 5.1 are shown in Figures 5.4 and 5.5. For all plots in this Chapter, central events (those with $\hat{b}<0.3$) are shown as solid points and mid-peripheral events (those with $0.3<\hat{b}<0.6$) are shown as open points. Only statistical errors are plotted, but systematic errors are summarized in Section 5.5.1.

One feature all spectra share is that the central differential multiplicity spectra are slightly higher than the mid-peripheral spectra. This is expected, as central collisions usually have a greater overlap in the beam and target densities and therefore more nucleons are involved in the collision, resulting in an increased multiplicity of free nucleons and light fragments. At large values of P_t/A, the spectra typically decay with a shape of $e^{-p_t^2/k_BT}$ or e^{-E_t/k_BT},
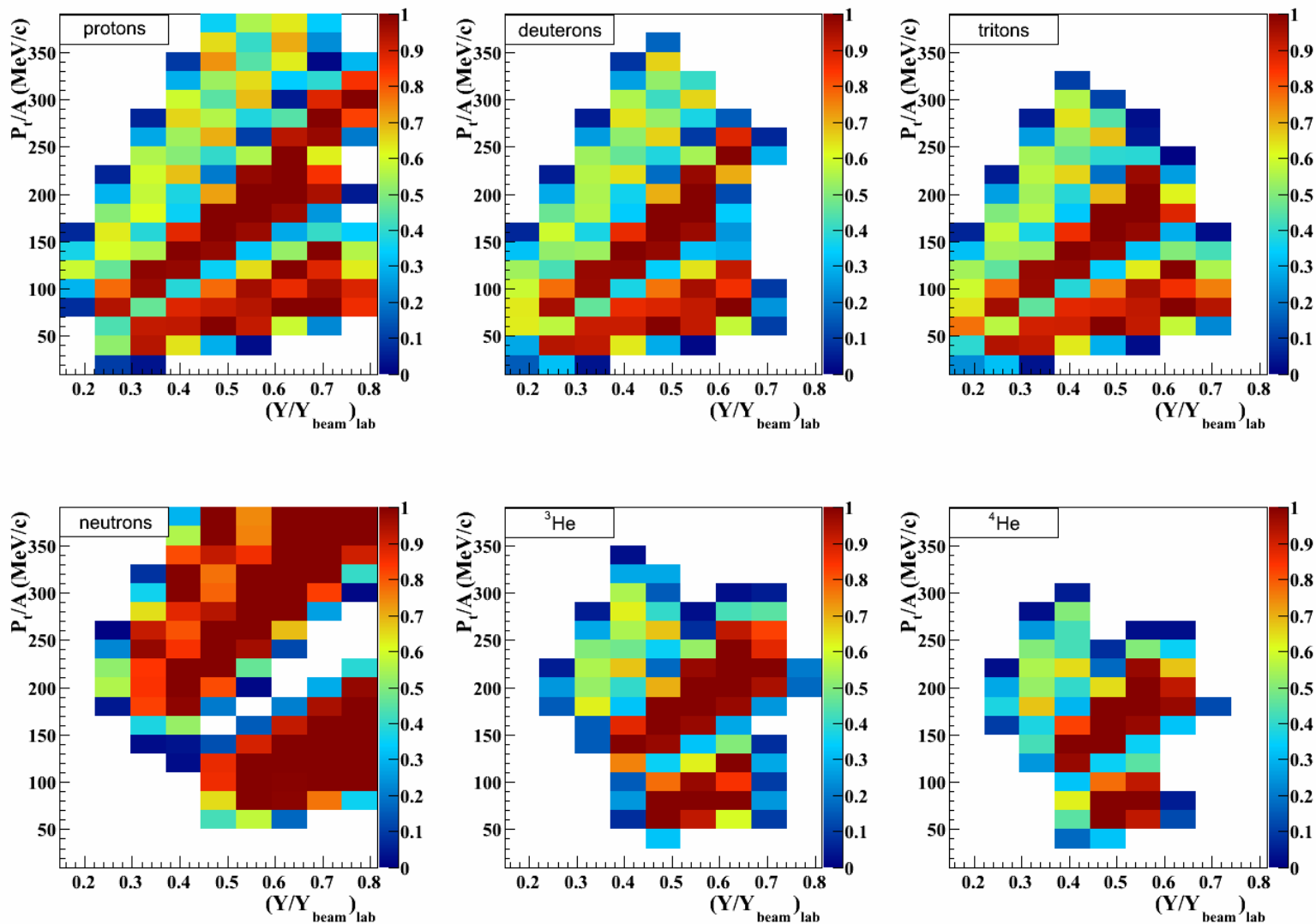
Figure 5.3: Fractional coverages of the ^{48}Ca+^{124}Sn masks for P_t/A, $(Y/Y_{beam})_{lab}$ bins of size $dP_t/A = 20$ MeV/c, $d(Y/Y_{beam})_{lab}$ = 0.075. Panels are labeled with the species shown.

125
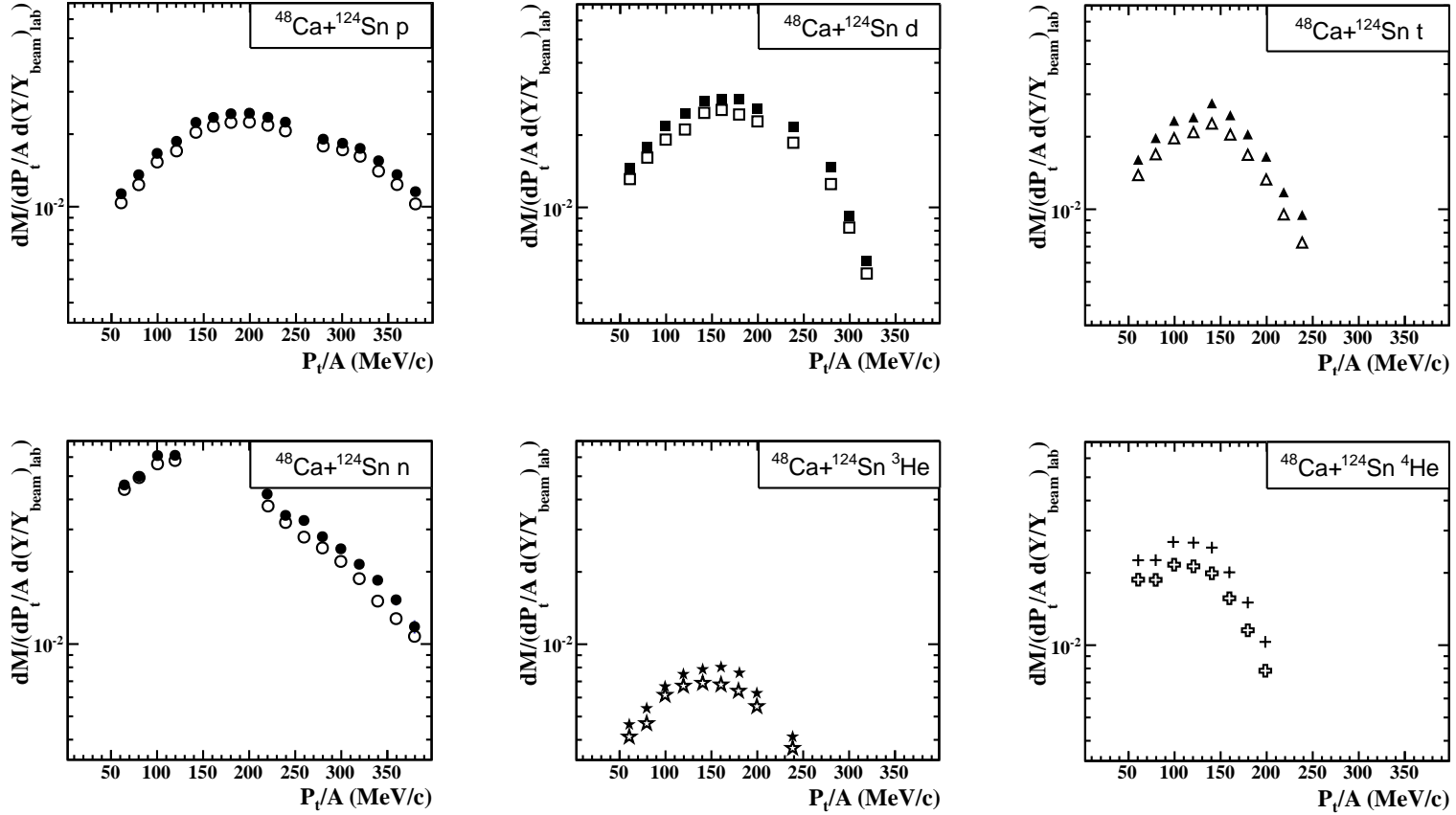
Figure 5.4: Free particle P_t/A spectra for the ^{48}Ca+^{124}Sn reaction within the mid-rapidity region. Panels are labeled with the individual species shown.
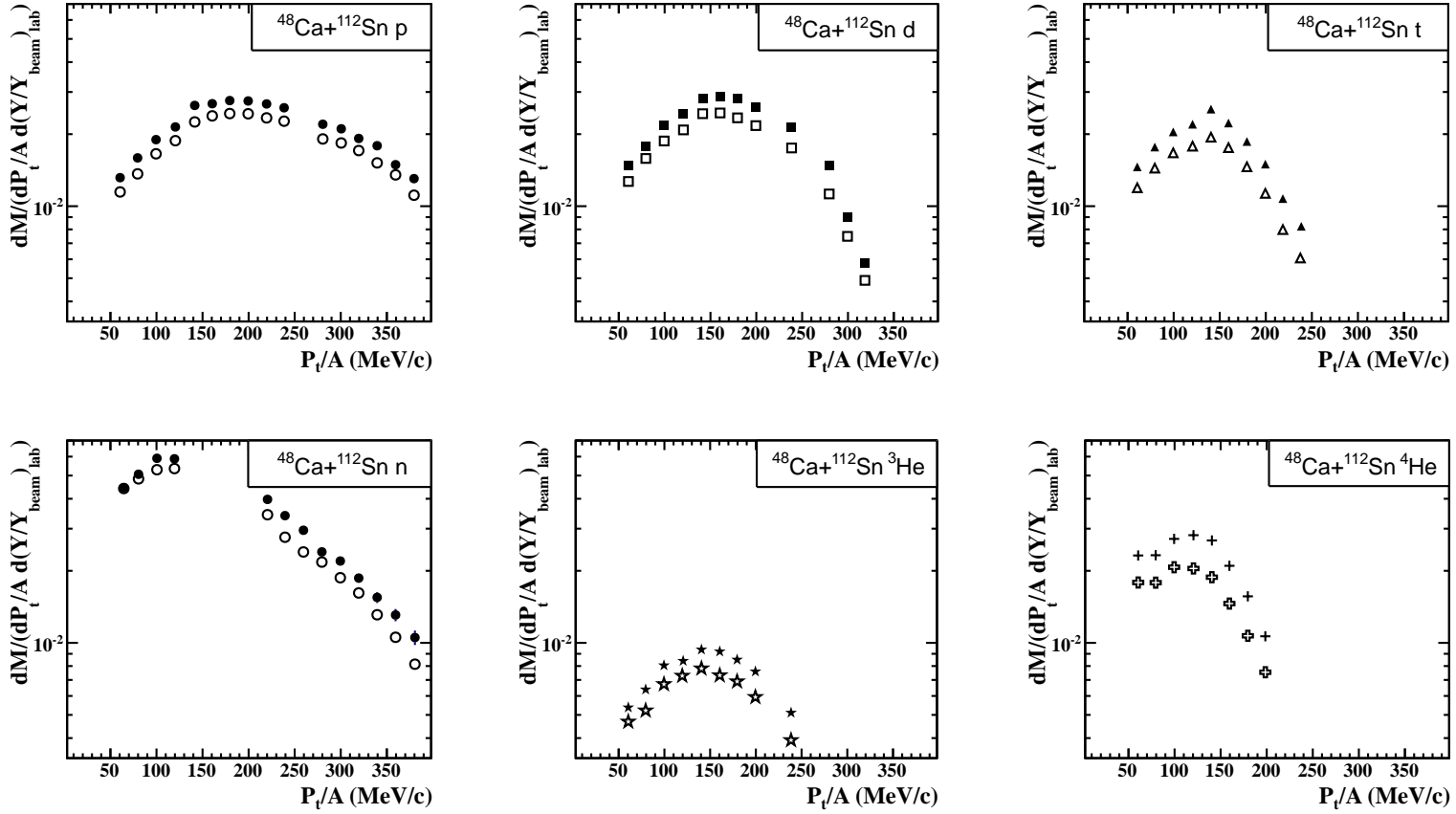
Figure 5.5: Free particle P_t/A spectra for the ^{48}Ca+^{112}Sn reaction within the mid-rapidity region. Panels are labeled with the individual species shown.

as one expects from the statistical decay of a thermalized source [45]. At lower values of P_t/A, the charged particles exhibit a peak that roughly corresponds to the Coulomb barrier. Neutrons also exhibit a peak at lower values of P_t/A which is partly due to the fact that neutron emission is not influenced by the Coulomb force. The breaks in the spectra are due to gaps in coverage as seen in the Monte Carlo masks in Figure 5.2.

The experimental free nucleon spectra are compared to ImQMD calculations in Figures 5.6 and 5.7 for neutrons and protons respectively. In these Figures and all further comparisons to ImQMD results in this Chapter, the calculations are shown as lines. Skyrme sets SLy4 and SkI2 with $m_n^* < m_p^*$ are in red, while SkM* and Gs with $m_n^* > m_p^*$ are in blue. The sets with soft symmetry strengths, SLy4 and SkM*, are shown as solid lines and while those with stiff symmetry strengths, SkI2 and Gs, are plotted with dotted lines.

For both species, the ImQMD predictions overpredict the central and mid-peripheral experimental data for both ^{48}Ca+^{124}Sn and ^{48}Ca+^{112}Sn. The closest match between the experiment and calculations is for mid-peripheral neutrons (upper panels of Figure 5.6) but the shapes of the spectra do not match. Protons at high P_t/A are slightly overpredicted by calculations. Generally, the difference between the experimental free nucleon spectra and the calculations are bigger than the differences between the parameter sets. These differences will become drastically smaller in Section 5.4, when CI nucleons are compared.

5.3   Spectral Ratios of Free Particles

The ratios of free neutrons and protons are compared to ImQMD calculations. As discussed in Section 1.3, spectral ratios should enhance the sensitivity of the data to the symmetry energy while diminishing effects from other potentials, such as Coulomb repulsion between
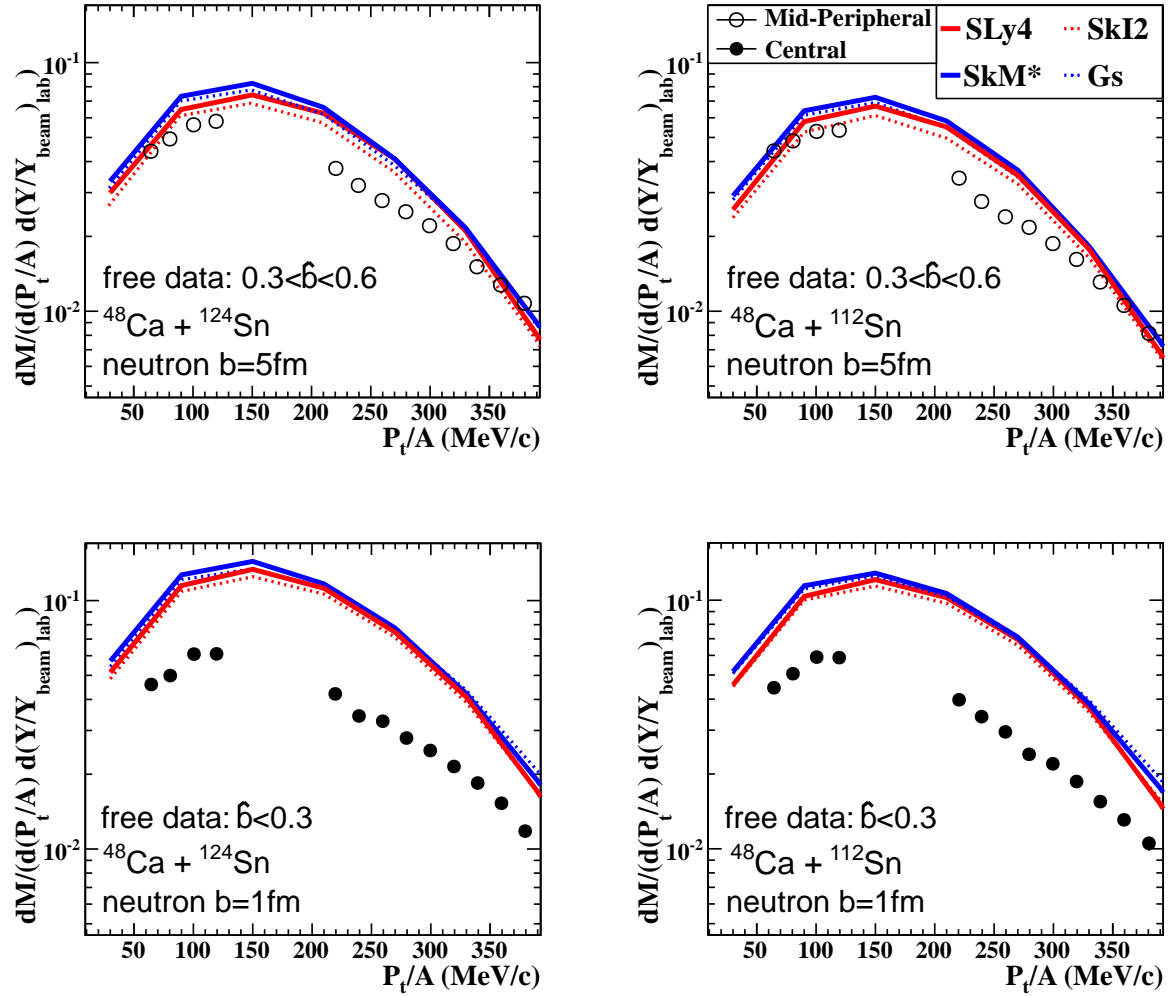
Figure 5.6: Experimental free neutron P_t/A spectra are compared to the neutrons calculated in ImQMD-Sky for four different parameter sets. Left panels: ^{48}Ca+^{124}Sn free neutrons. Right panels: ^{48}Ca+^{112}Sn free neutrons. Upper panels: mid-peripheral collisions. Lower panels: central collisions.
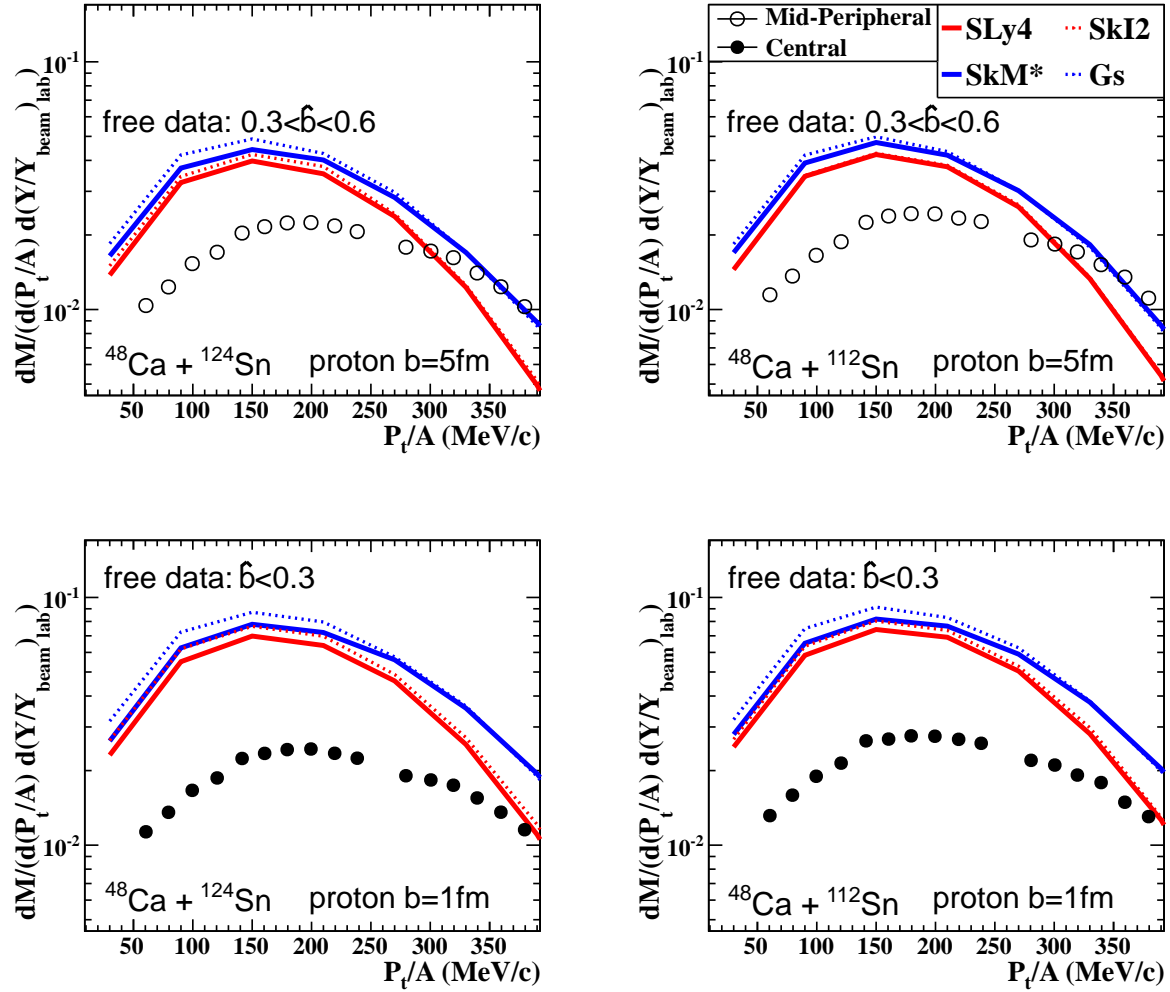
Figure 5.7: Experimental free proton P_t/A spectra are compared to the protons calculated in ImQMD-Sky for four different parameter sets. Left panels: ^{48}Ca+^{124}Sn free protons. Right panels: ^{48}Ca+^{112}Sn free protons. Upper panels: mid-peripheral collisions. Lower panels: central collisions.

protons, or difficulties in the analysis, such as accounting for neutron detection efficiencies. As discussed in Chapter 4, we expect that the free nucleons will compare well to calculations only for regions of high transverse momentum.

The isoscaling ratios from Equation 1.7 are shown in Figure 5.8, with $R_{21}(n)$ depicted in the left panels and $R_{21}(p)$ in the right panels. Here the convention is followed that reaction 2 is the more neutron-rich reaction, ^{48}Ca+^{124}Sn, and reaction 1 is the less neutron-rich reaction, ^{48}Ca+^{112}Sn. For all four panels, the free experimental data are shown as circular points. In this Figure and in all further multi-panel comparisons between empirical ratios and ImQMD calculations, the mid-peripheral data are shown in the upper panels ($0.3<\hat{b}<0.6$ or b=5 fm) and the central data are shown in the lower panels ($\hat{b}<0.3$ or b=1 fm). Only the statistical errors are displayed. The $R_{21}(n)$ data generally lie above 1, as expected since by convention the more neutron-rich reaction is in the numerator. Likewise, the free $R_{21}(p)$ data lie below 1 as we expect. In general, the data compare well to the calculations especially at larger values of P_t/A. However, there is little sensitivity to either L, the slope of the symmetry energy strength, or to $m_n^* \neq m_p^*$, the effective mass splitting.

In Figure 5.8 and all further plots in this Chapter, the no-sensitivity limits for each ratio are shown at dashed gray lines. These limits are the initial value for each ratio, calculated from the composition of the beam and target nucleons. For example, the no-sensitivity limit of $R_{21}(n)$ is $N_0(^{48}$Ca+^{124}Sn$)/N_0(^{48}$Ca+^{112}Sn$) = 102/90 \approx 1.13$. This is the expected value for the ratio if the nucleons were emitted from a thermalized source in proportion to their numbers within the source. One might imagine that this would be the result if the nucleons were distinguishable particles in the absense of the Pauli exclusion principle and there were no symmetry or Coulomb mean field potentials that could lead to a preferential emission of either protons or neutrons beyond their initial ratios.
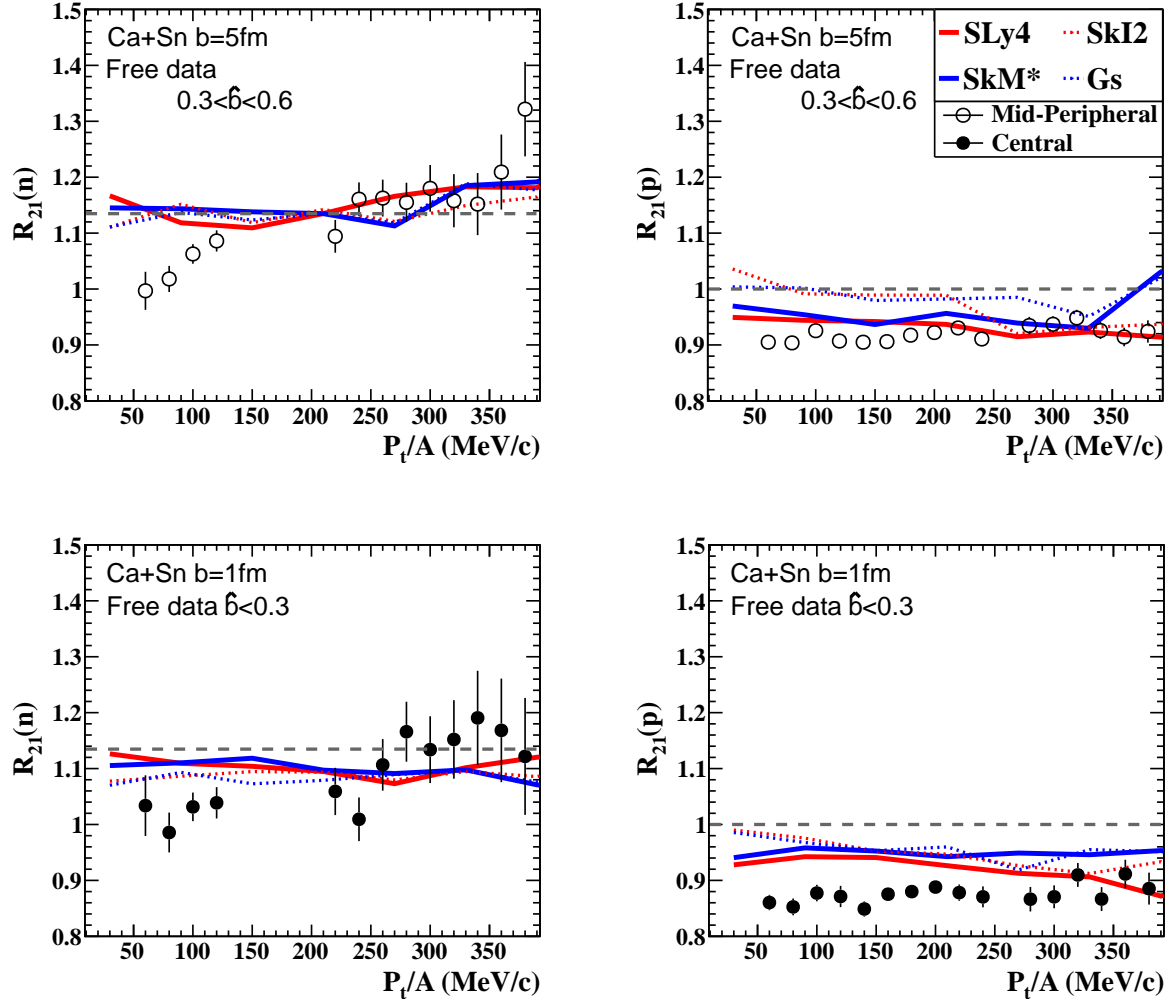
Figure 5.8: Isoscaling ratios of free nucleons are shown as circles. ImQMD-Sky calculations are shown as lines. Left panels: Single neutron ratios, $R_{21}(n)$. Right panels: Single proton ratios, $R_{21}(p)$. Upper panels: mid-peripheral collisions. Lower panels: central collisions.

For completeness, the isoscaling ratios for the measured particles with A>1 (deuterons, tritons, ^{3}He, ^{4}He) are shown in Figure 5.9. The isoscaling ratios for both deuterons and ^{4}He are near 1, which is expected since these are symmetric particles that should demonstrate little sensitivity to the symmetry energy. The $R_{21}(t)$, isoscaling ratios of tritons, lie above 1, with the interpretation of tritons as 'neutron-like' since they are composed of two neutrons and one proton. The values of $R_{21}(t)$ are consistent with $R_{21}(n)$ from Figure 5.8. Similarly, $R_{21}(^3He)$ lie below 1 and have similar values to $R_{21}(p)$ in Figure 5.8, consistent with the interpretation of ^{3}He as 'proton-like' since it has two protons and one neutron.

The n/p ratios as written in Equation 1.6 are shown in Figure 5.10 as the circular points, again with only statistical errors displayed. The left panels show $R(n/p)$ for ^{48}Ca+^{124}Sn while ^{48}Ca+^{112}Sn $R(n/p)$ are shown in the right panels. The $R(n/p)$ values are slightly lower for the ^{48}Ca+^{112}Sn reaction, which one might expect from the lower N/Z starting value of the reaction. The empirical $R(n/p)$ data generally compare well to the calculations especially in the high momentum range of P_t/A>200 MeV/c. At low P_t/A, the data points are typically twice as large as the calculations, demonstrating the poor matchup of the free nucleon data to transport model calculations at low energies, as seen in previous studies.

The empirical n/p ratios are subject to analytical difficulties; the neutrons in particular have multiple efficiency corrections that can have significant effects on the data. To limit the systematic effects on the data, a double neutron to proton ratio $DR(n/p)$ is often used, whereby any factor that effects one particle or one reaction will be cancelled. This ratio is written in Equation 1.8. The free nucleon $DR(n/p)$ are shown in Figure 5.11. The empirical $DR(n/p)$ again compare well to the calculations. However, similar to the isoscaling ratios, there is little sensitivity within the modeled $DR(n/p)$ to either the symmetry energy strength or the effective mass splitting.
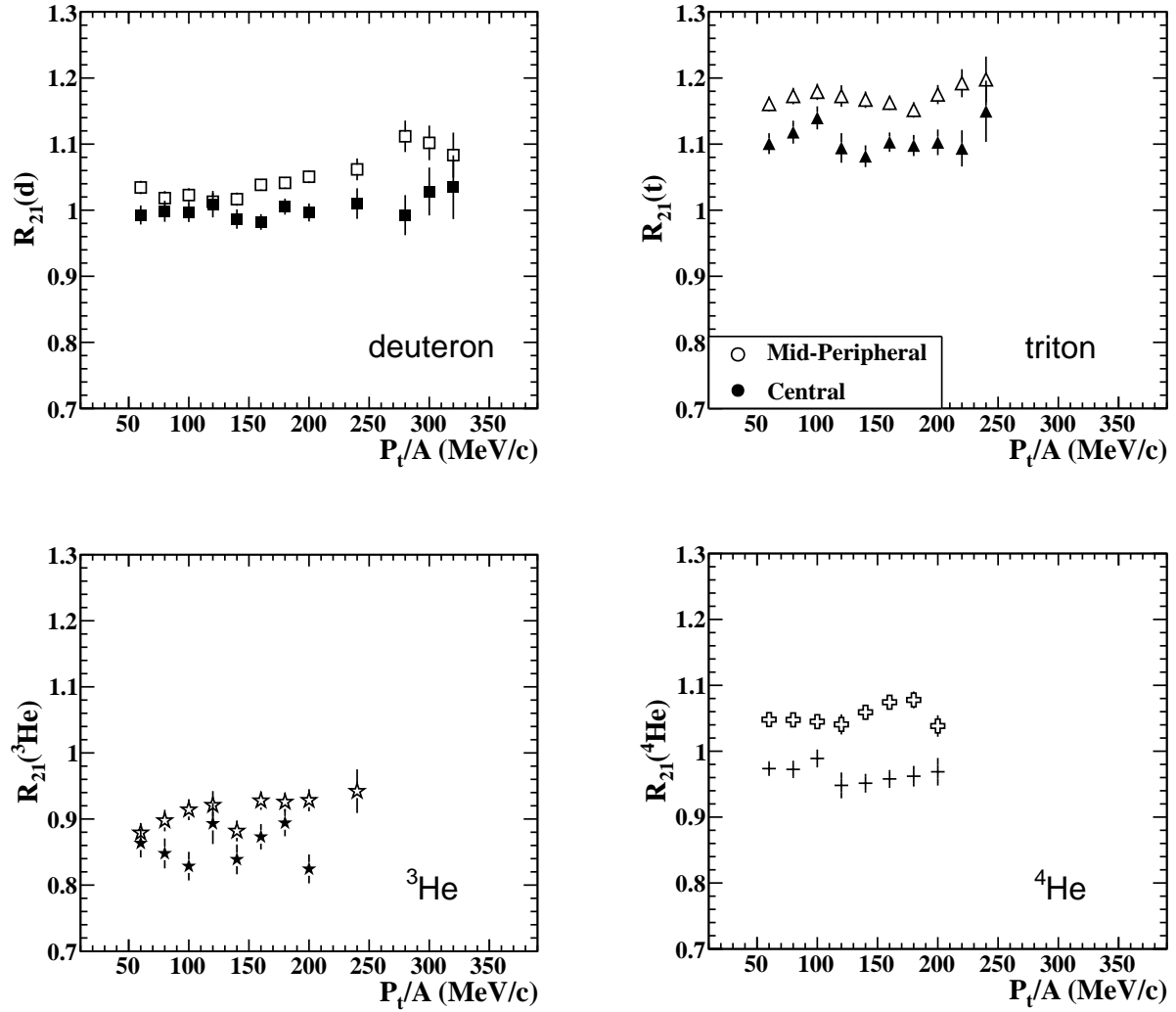
Figure 5.9: Isoscaling ratios of A>1 particles as labeled in each panel. All open points are data from mid-peripheral collisions. All closed points are from central collisions.
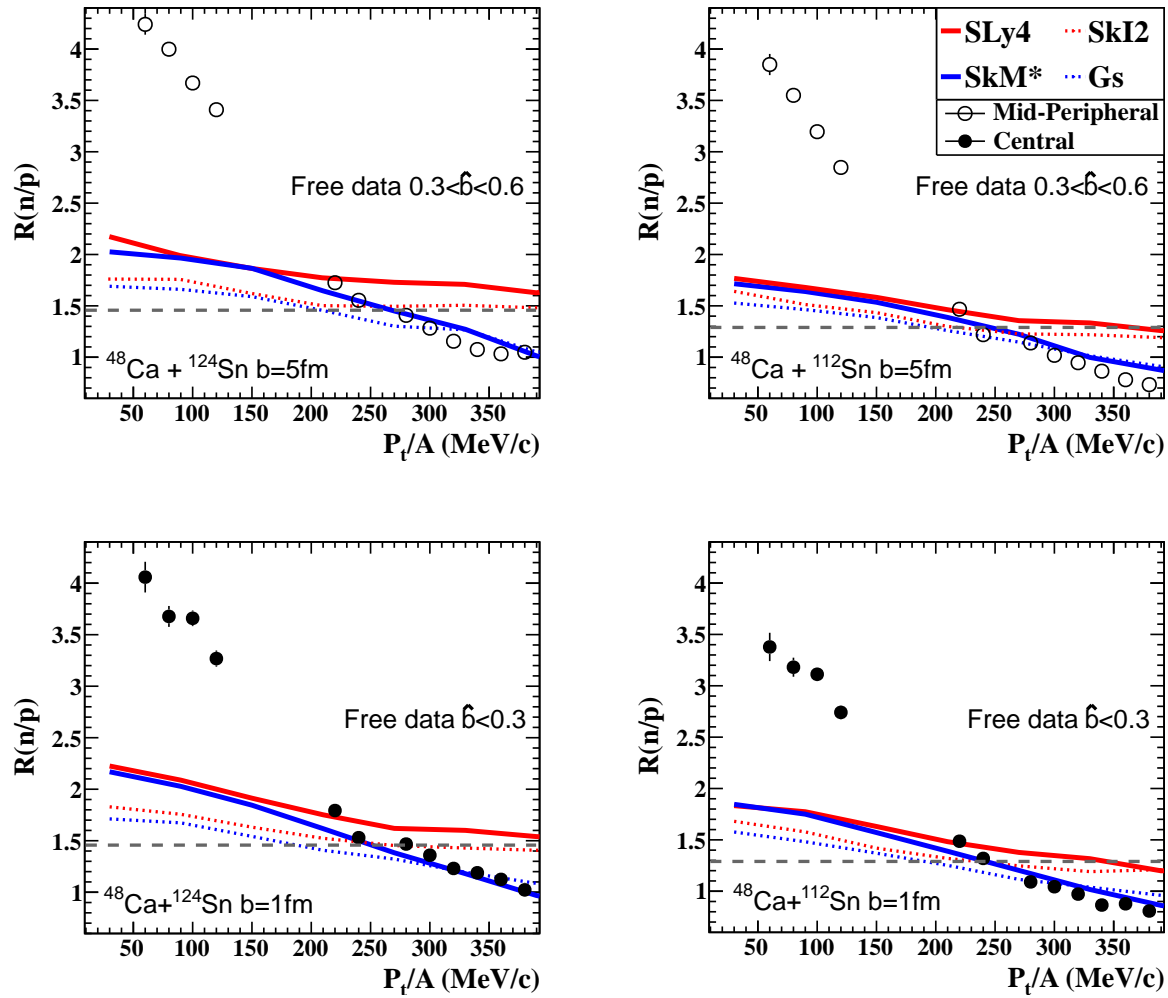
Figure 5.10: $R(n/p)$ from free nucleons are shown as circular data points. ImQMD-Sky calculations are shown as lines. Left panels: $R(n/p)$, for ^{48}Ca+^{124}Sn. Right panels: $R(n/p)$ for ^{48}Ca+^{112}Sn. Upper panels: mid-peripheral collisions. Lower panels: central collisions.
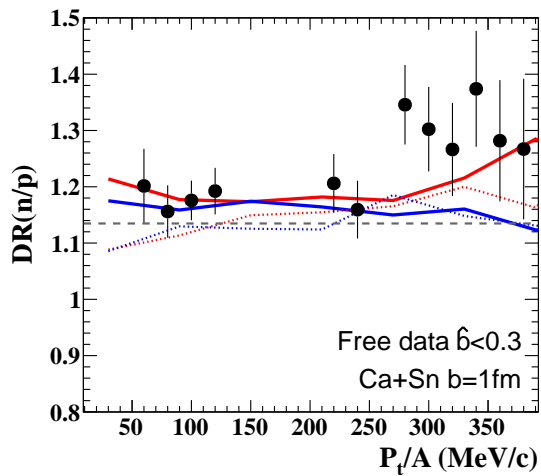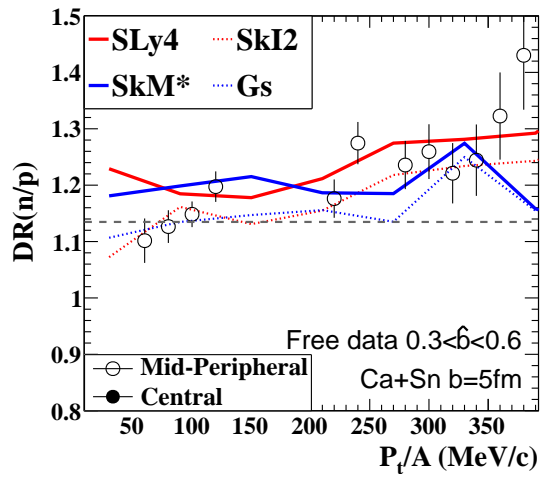
Figure 5.11: Free nucleon $DR(n/p)$ data are shown as circular data points. ImQMD-Sky calculations are shown as lines. Upper panel: mid-peripheral collisions. Lower panel: central collisions.

5.4 Coalescence Invariant (CI) Spectra

Previous studies ([2,3,45]) have observed that the free neutron and proton spectra obtained from experiments are not very well described by the spectra calculated by the transport models. In particular, transport models are currently unable to quantitatively reproduce the production of nucleons and LCPs observed from HICs, partly due to flaws in the code algorithm that identifies fragments and partly due to the cluster formation theories in ImQMD. Some fragments, for example ^{4}He, are produced in ImQMD calculations at significantly lower rates than what are observed in the empirical data. To overcome this limitation of the calculations, the experimental data and model calculations are made more similar: the measured fragment spectra (A>1) are broken into their constituent neutrons and protons and added into the respective free $A = 1$ spectra. These summed spectra are called coalescence invariant (CI) spectra because they are the total neutron and proton spectra regardless of whether the particles are observed as free or as coalesced into fragments.

As described in Section 4.4, the experimental CI neutron spectra are built as follows from the measured LCP spectra within the same beam-target combination, centrality cut, and mid-rapidity cut:

$$\frac{dY_{CI}(n)}{d(P_t/A)} = \frac{dY_{free}(n)}{d(P_t/A)} + \frac{dY(d)}{d(P_t/A)} + 2 \cdot \frac{dY(t)}{d(P_t/A)} + \frac{dY(^3He)}{d(P_t/A)} + 2 \cdot \frac{dY(^4He)}{d(P_t/A)} \qquad (5.2)$$

The experimental CI proton spectra are built as follows:

$$\frac{dY_{CI}(p)}{d(P_t/A)} = \frac{dY_{free}(p)}{d(P_t/A)} + \frac{dY(d)}{d(P_t/A)} + \frac{dY(t)}{d(P_t/A)} + 2 \cdot \frac{dY(^3He)}{d(P_t/A)} + 2 \cdot \frac{dY(^4He)}{d(P_t/A)} \qquad (5.3)$$

The spectra in Figures 5.4 and 5.5 show that particles with $A > 1$ have P_t/A cutoffs

much lower than those for free protons and neutrons. To extend the P_t/A range available, we extrapolate the $A > 1$ spectra past their empirical cutoff points. Following Ref [45], we assume that particles with large momenta (large energies) are emitted as if from a thermalized source, with the shape of their spectra following $\sim e^{-E/T}$, or $\sim e^{-p^2/T}$. To obtain the values for the spectra out to the proton $P_t/A = 400$ MeV/c cutoff, the last 5-6 points of each $A > 1$ spectra were fit with a line of the form $e^{-(C \cdot (P_t/A)^2 + D)}$, where C and D are the fit parameters. The difference between the last data point and the fit value at the same P_t/A was used to estimate the fit error. The extrapolated $A > 1$ spectra are shown as red points for the ^{48}Ca+^{124}Sn reaction in Figure 5.12 and for the ^{48}Ca+^{112}Sn reaction in Figure 5.13, with the measured data points shown as black points. As with previous Figures, central data ($\hat{b}$<0.3) are shown as closed points and mid-peripheral events ($0.3<\hat{b}$<0.6) are open points.

Finally, the empirical and extrapolated $A > 1$ spectra were added to the free neutron and proton spectra following Equations 5.2 and 5.3. In the range of the $A > 1$ particle spectra where we obtained experimental data, the CI neutrons and protons were only constructed in P_t/A bins that have information for all $A > 1$ particles. "Empty" bins with transverse momenta lower than the P_t/A cutoffs could in principle be extrapolated from the higher energy data, but the low momentum data are not the relevant region to compare between experiment and model calculation. Further, the ideal shape of the spectra is unknown, in part because the symmetry energy that governs the spectra is so poorly constrained. Therefore only the large P_t/A values were extrapolated before being added to form the CI spectra.

The CI neutrons and protons are shown in Figures 5.14 and 5.15 for neutrons and protons respectively, along with CI spectra predicted by ImQMD-Sky calculations. In general the CI neutron spectra have larger values than the CI protons, which is expected since both reactions have a neutron excess. For both species, the ImQMD predictions
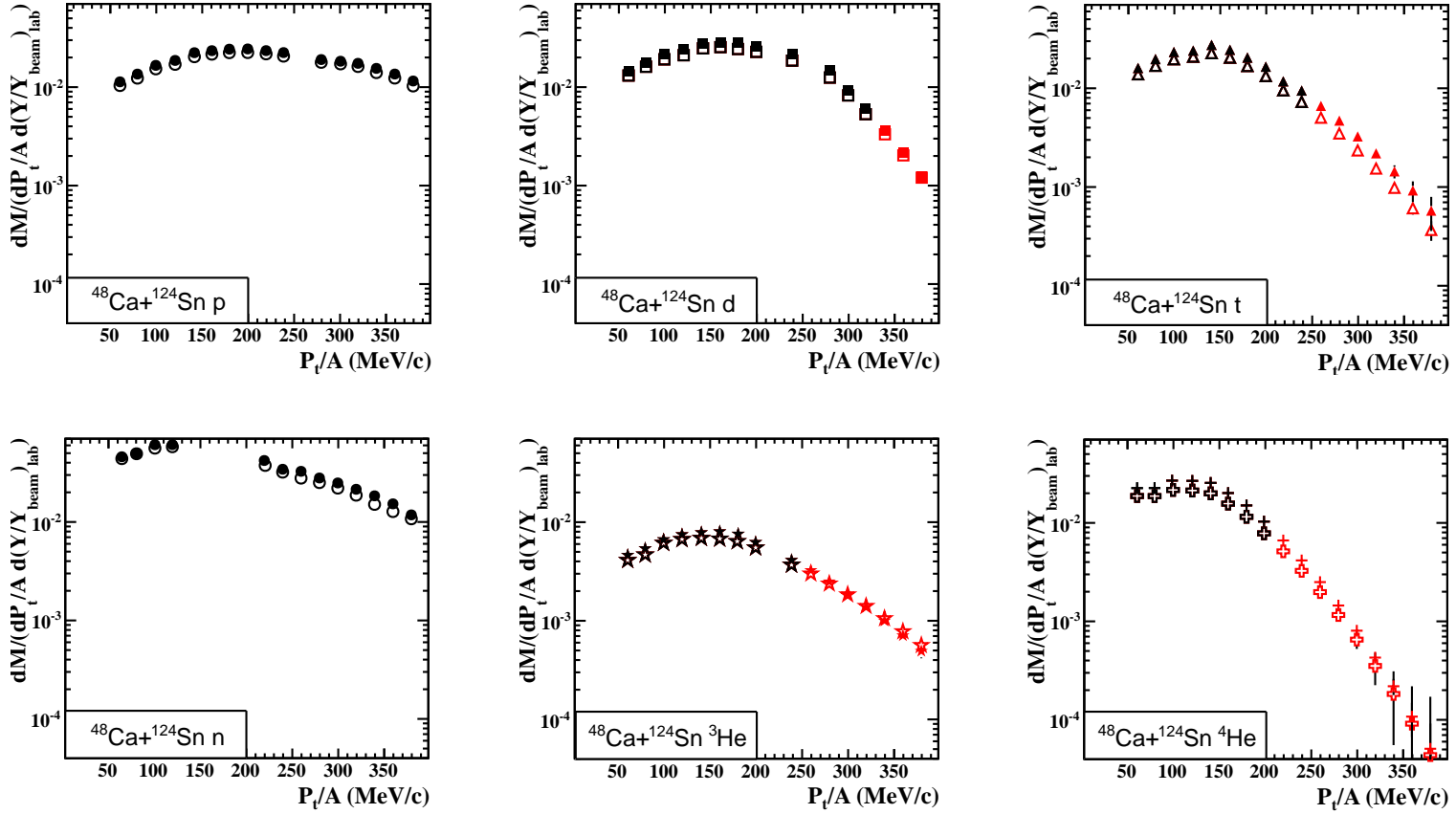
Figure 5.12: Free particle P_t/A spectra (black points) and extended spectra (red points) for the ^{48}Ca+^{124}Sn reaction within the mid-rapidity region. Panels are labeled with the individual species shown.
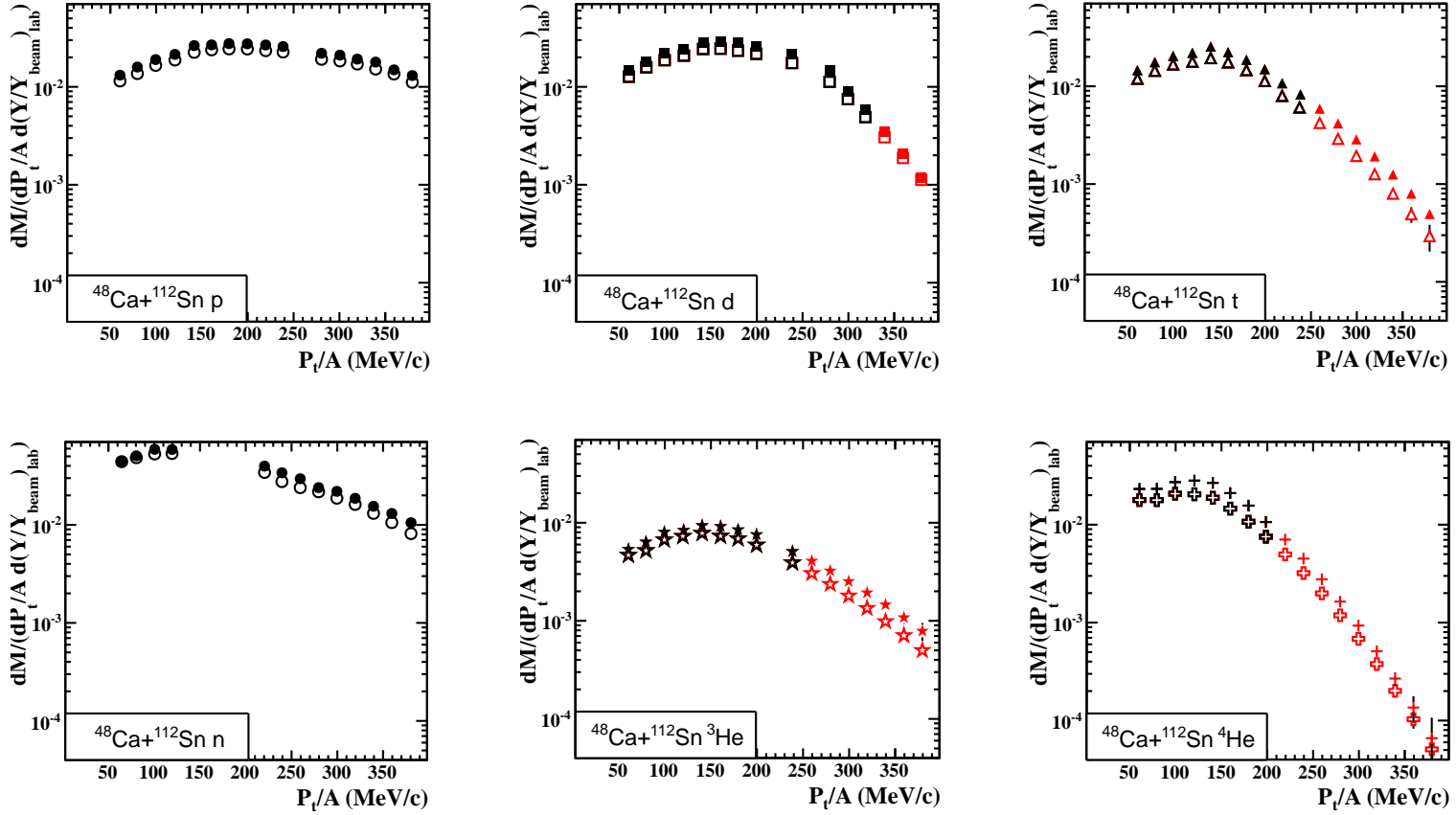
Figure 5.13: Free particle P_t/A spectra (black points) and extended spectra (red points) for the ^{48}Ca+^{112}Sn reaction within the mid-rapidity region. Panels are labeled with the individual species shown.

have roughly the correct order of magnitude for both centrality cuts and for both reactions. More importantly, the shapes of the spectra are very similar. Generally, the mid-peripheral spectra are underpredicted by calculations while central spectra are overpredicted.

For most of the comparisons, the difference between the experimental CI nucleon spectra and the calculations are bigger than the differences between the parameter sets. As the comparison of free experimental and predicted nucleon spectra in Figures 5.6 and 5.7 disagreed greatly, especially at low values of P_t/A, the much improved agreement here clearly demonstrates the strength of comparing CI nucleons.

5.5   Coalescence Invariant (CI) Particle Ratios

The CI nucleon isoscaling ratios, constructed as defined in Equation 1.7, are shown in Figure 5.16. The neutron isoscaling ratios, $R_{21}(n)$, are shown in the left panels and the proton isoscaling ratios, $R_{21}(p)$, are shown in the right panels. For all four panels, the CI ratios are shown as circles, with only the statistical errors displayed. In general, the data compare well to the calculations especially at larger values of P_t/A. However, there is little sensitivity within the models to either the symmetry energy strength or the effective mass splitting.

The CI n/p ratios as defined in Equation 1.6 are shown in Figure 5.17. The left panels show CI $R(n/p)$ for ^{48}Ca+^{124}Sn while ^{48}Ca+^{112}Sn CI data are shown in the right panels. The $R(n/p)$ values are slightly lower for the ^{48}Ca+^{112}Sn reaction, which one might expect from the lower starting N/Z value of the reaction. The empirical CI $R(n/p)$ data generally compare well to the calculated values across the entire P_t/A range.

In the range of P_t/A>200 MeV/c, the CI $R(n/p)$ are in good agreement with both SkM* and Gs Skyrme parameterizations, each of which use $m_n^* > m_p^*$. Below P_t/A=200 MeV/c, the
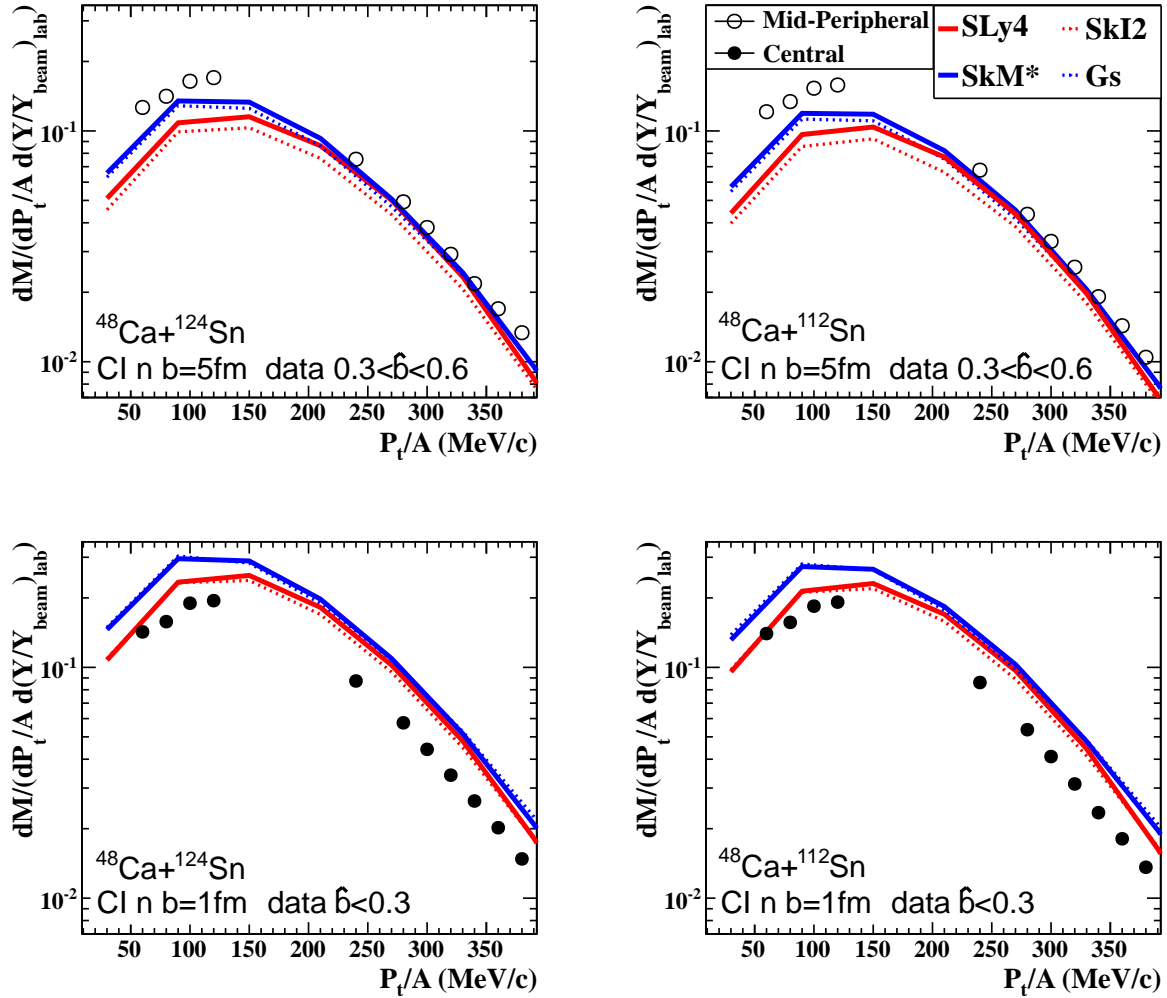
Figure 5.14: Experimental CI neutron P_t/A spectra are compared to the CI neutrons calculated in ImQMD-Sky for four different parameter sets. Left panels: ^{48}Ca+^{124}Sn. Right panels: ^{48}Ca+^{112}Sn. Upper panels: mid-peripheral collisions. Lower panels: central collisions.
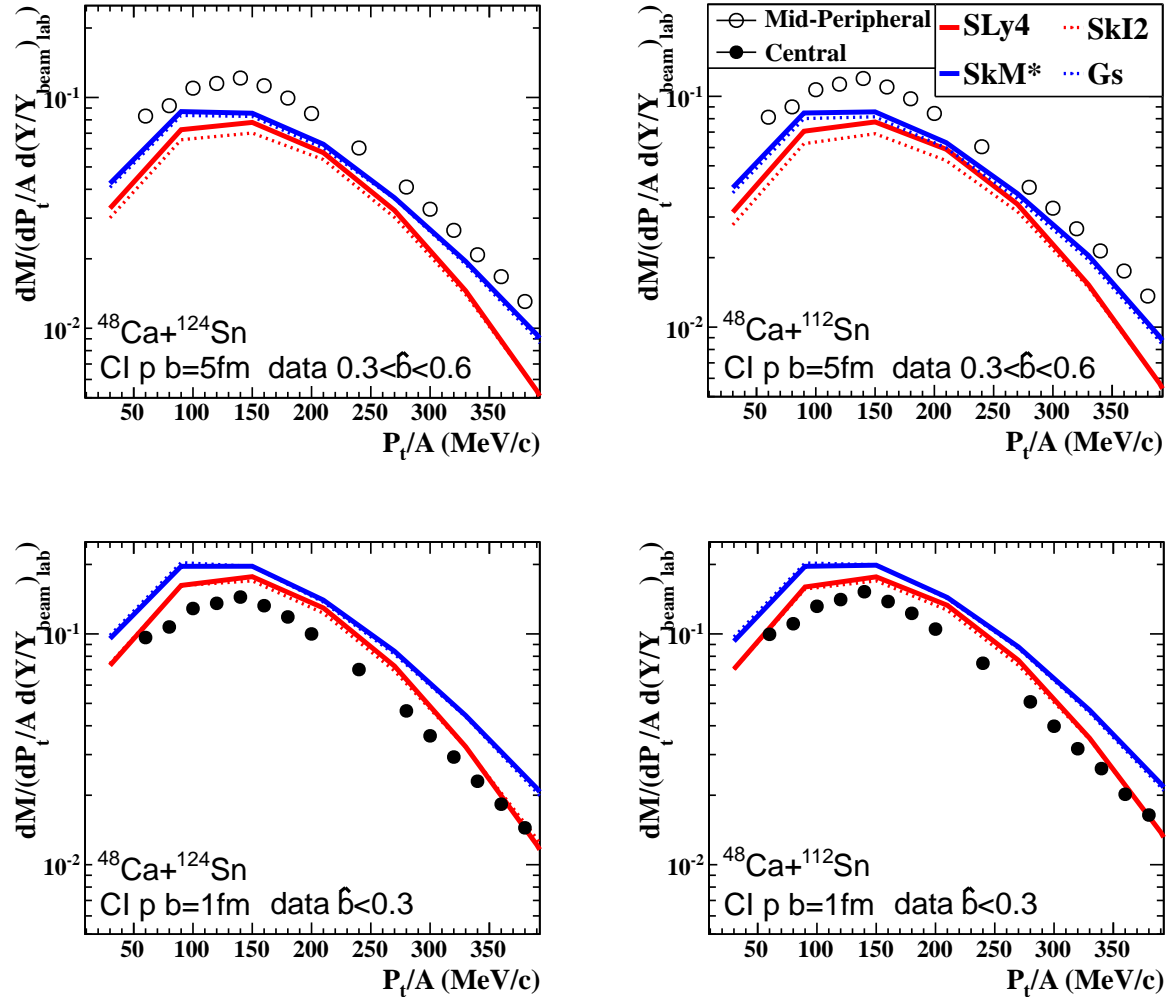
Figure 5.15: Experimental CI proton P_t/A spectra are compared to the CI protons calculated in ImQMD-Sky for four different parameter sets. Left panels: ^{48}Ca+^{124}Sn. Right panels: ^{48}Ca+^{112}Sn. Upper panels: mid-peripheral collisions. Lower panels: central collisions.
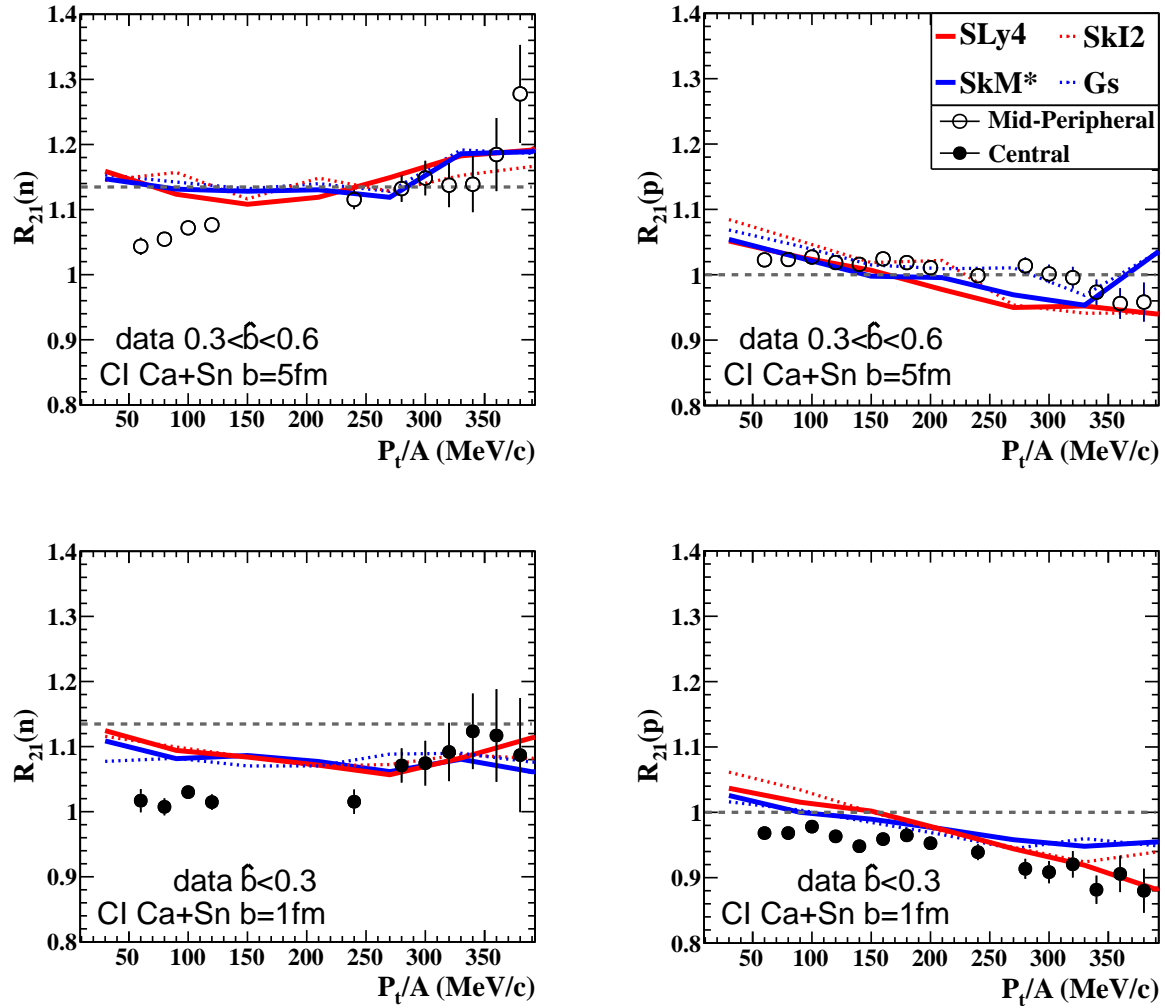
Figure 5.16: Isoscaling ratios of CI nucleons are shown as circular data points. ImQMD-Sky calculations are shown as lines. Left panels: neutron isoscaling ratios, $R_{21}(n)$. Right panels: proton isoscaling ratios, $R_{21}(p)$. Upper panels: mid-peripheral collisions. Lower panels: central collisions.
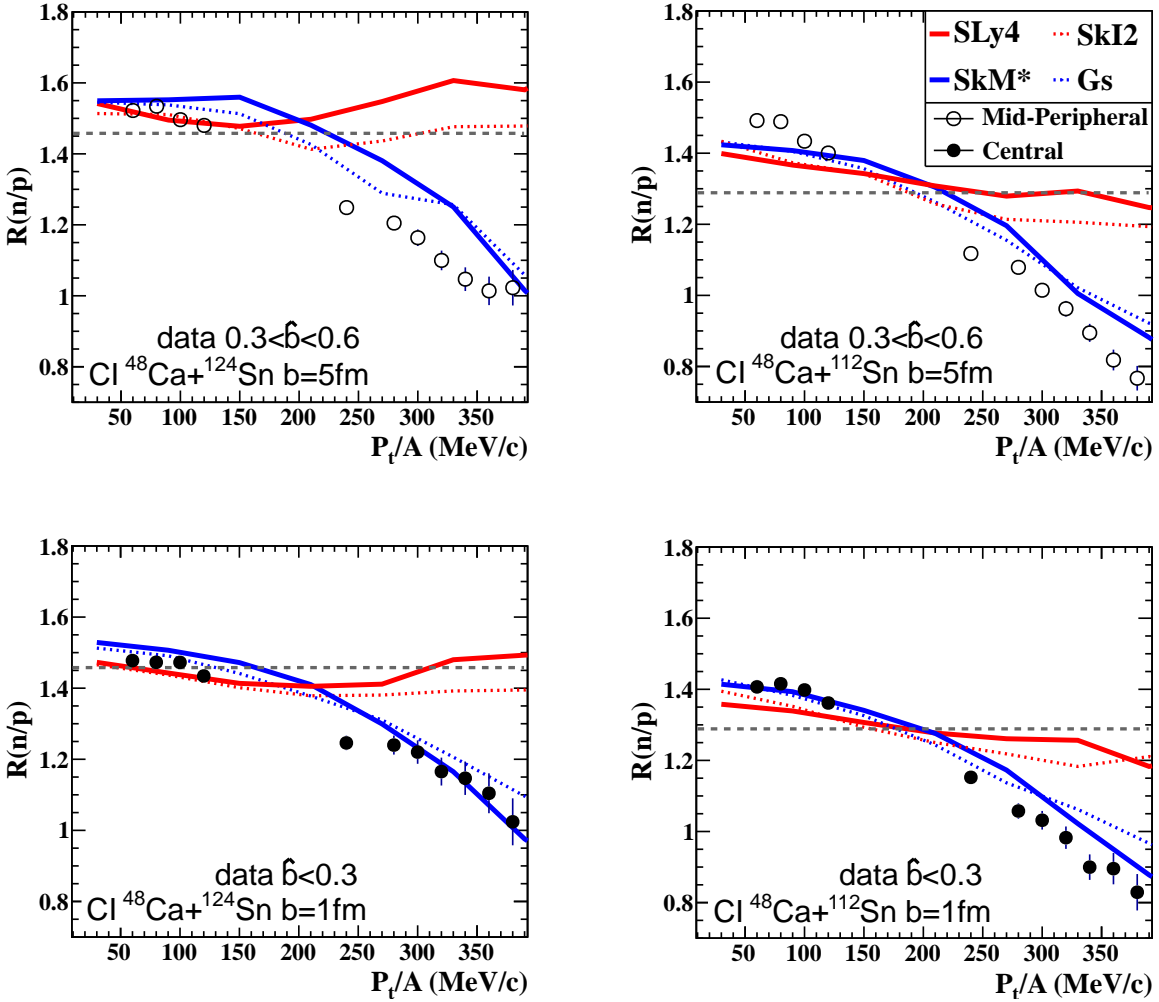
Figure 5.17: The n/p ratios from CI nucleons are shown as circular points for experimental data. ImQMD-Sky calculations are shown as lines. Left panels: $R(n/p)$, for ^{48}Ca+^{124}Sn. Right panels: $R(n/p)$ for ^{48}Ca+^{112}Sn. Upper panels: mid-peripheral collisions. Lower panels: central collisions.

experimental CI n/p ratios generally agree with all four calculations; this is in concordance with the findings in Ref [61], in which the sensitivity to L is suppressed for CI $R(n/p)$ at low energies or low momenta. Overall the CI $R(n/p)$ favor calculations with $m_n^* > m_p^*$. This is the opposite result as that seen in the companion Sn+Sn experiment, which concluded that $m_n^* < m_p^*$ [2,3]. A comparison between the two results is presented in Section 5.7.

Finally, the CI $DR(n/p)$ as defined in Equation 1.8 are shown in Figure 5.18 and again compare well to the calculations. However, as for the isoscaling ratios, the sensitivity within the models to either the symmetry energy strength or the effective mass splitting for $DR(n/p)$ is reduced compared to $R(n/p)$ as a result of the relative similarities between $R(n/p)$ for the neutron-rich and neutron-poor reactions. It is important to remember that the statistical errors of the ImQMD-Sky calculations are both not displayed on this Figure and quite large for the $DR(n/p)$: none of the calculations are excluded in the comparison at high P_t/A when the statistical errors are taken in account.

5.5.1 Systematic Errors of Ratios

The systematic errors discussed in Section 3.4 are carried through to the free and CI ratios presented here. For the isoscaling ratios, most of the systematic errors cancel since these errors are correlated. As an example, consider that the uncertainty in the DSSD detection efficiency introduces an upper systematic error of $+5\%$ to the charged particle spectra. If that silicon detection efficiency is actually 5% off, it would be off by 5% for both reactions. When constructing the free or CI $R_{21}(p)$, this extra factor of 1.05 cancels out on both sides. For the same reason, the $DR(n/p)$ tend to have low systematic errors, due to the correlation of those errors from the two isoscaling ratios used in their construction.

The systematic errors in the spectra tend to persist when taking $R(n/p)$, because the
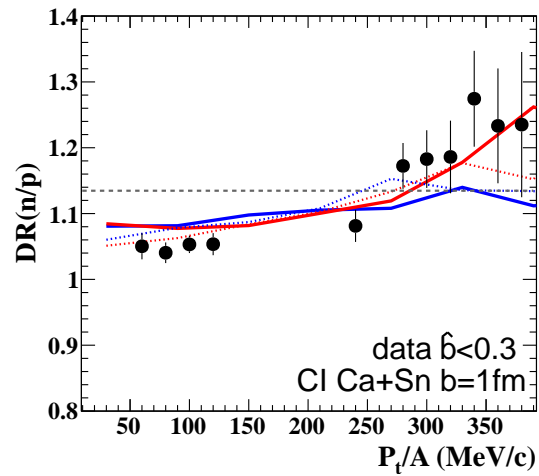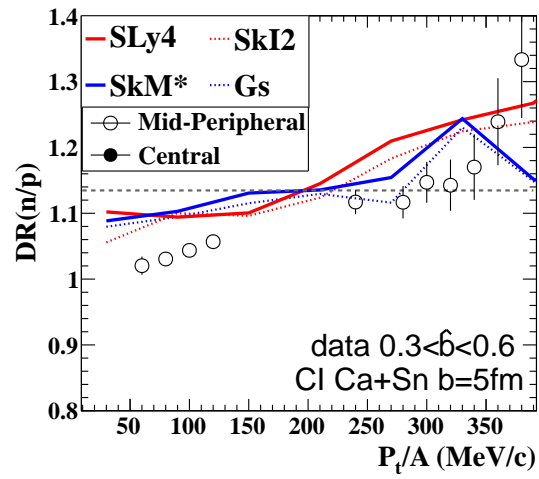
Figure 5.18: Double neutron to proton ratios, $DR(n/p)$ for Ca+Sn data. Experimental CI nucleon $DR(n/p)$ data are circular points. ImQMD-Sky calculations are shown as lines. Upper panel: mid-peripheral collisions. Lower panel: central collisions.

Table 5.1: Systematics of the free ratios calculated in this work.

Ratio	Centrality	Upper Limit Low P_t/A (%)	Lower Limit Low P_t/A (%)	Upper Limit High P_t/A (%)	Lower Limit High P_t/A (%)
$R_{21}(n)$	MP	0.12	0.16	0.01	0.02
	Cent	0.15	0.20	0.02	0.02
$R_{21}(p)$	MP	0	0	0	0
	Cent	0	0	0	0
$R_2(n/p)$	MP	11.3	11.3	12.2	16.4
	Cent	11.3	15.5	12.2	16.4
$R_1(n/p)$	MP	11.5	15.7	12.2	16.4
	Cent	11.5	15.7	12.2	16.4
$DR(n/p)$	MP	0.12	0.16	0.03	0.04
	Cent	0.15	0.20	0.02	0.02

Table 5.2: Systematics of the CI ratios calculated in this work.

Ratio	Centrality	Upper Limit Low P_t/A (%)	Lower Limit Low P_t/A (%)	Upper Limit High P_t/A (%)	Lower Limit High P_t/A (%)
$R_{21}(n)$	MP	2.2	0.20	2.1	0.19
	Cent	1.2	0.14	6.0	0.52
$R_{21}(p)$	MP	0	0	0	0
	Cent	0	0	0	0
$R_2(n/p)$	MP	0.11	4.0	4.1	9.2
	Cent	0.06	3.6	4.1	9.3
$R_1(n/p)$	MP	0.22	4.1	3.9	9.0
	Cent	0.01	3.7	3.8	8.9
$DR(n/p)$	MP	2.2	0.20	2.1	0.19
	Cent	1.2	0.14	6.0	0.52

systematic errors in the neutrons are not correlated with the charged particle systematic errors. When evaluating the effects of the systematic errors, the extreme cases are taken– that is, the upper systematic limit of $R(n/p)$ is found by dividing the upper limit of the neutron spectrum by the lower limit of the proton spectrum, thus attaining the maximal value of the $R(n/p)$ allowed within the systematic errors.

The upper and lower systematic errors calculated for the free and CI ratios are summarized in Tables 5.1 and 5.2.

5.6 Comparison to Isospin-Independent Cross Sections

To check the influence of different cross sections in the transport model, the experimental data are compared in this Section to calculations using the isospin-independent form of σ_{NN} as written in Equation 4.17. All the circular points in Figures 5.19, 5.20, and 5.21 are the same experimental CI data shown in Figures 5.16, 5.17, and 5.18 from Section 5.5, but the ImQMD-Sky calculations displayed in this Section only use the alternate, isospin-independent σ_{NN}.

The CI $R_{21}(x)$ calculated with isospin-independent cross sections are compared to CI experimental data in Figure 5.19. Removing the isospin-dependence of the cross sections did not change the calculated isoscaling ratios very much, as discussed in Section 4.7. The experimental data still agree with the predictions from this form of the calculations.

The CI n/p ratios as defined in Equation 1.6 are shown in Figure 5.20. The left panels show CI $R(n/p)$ for ^{48}Ca+^{124}Sn while ^{48}Ca+^{112}Sn CI $R(n/p)$ are shown in the right panels. In general, at high P_t/A the gap between the experimental observations and the calculated predictions is wider than what was observed in the comparisons to n/p ratios using isospin-dependent cross sections in Figure 5.17. Only the central ^{48}Ca+^{124}Sn experimental $R(n/p)$ (lower left panel) still lie as close to the calculations in the isospin-independent cross section calculations as for the isospin-dependent calculations.

Finally, the CI $DR(n/p)$ as defined in Equation 1.8 are shown in Figure 5.21. Again there is good agreement between measured and predicted values. However, as for the isoscaling ratios, there was little sensitivity in $DR(n/p)$ to the forms of the cross sections used.

Based primarily on the results from $R(n/p)$, the comparison of the experimental data to ImQMD-Sky calculations favor cross sections that are dependent on isospin.
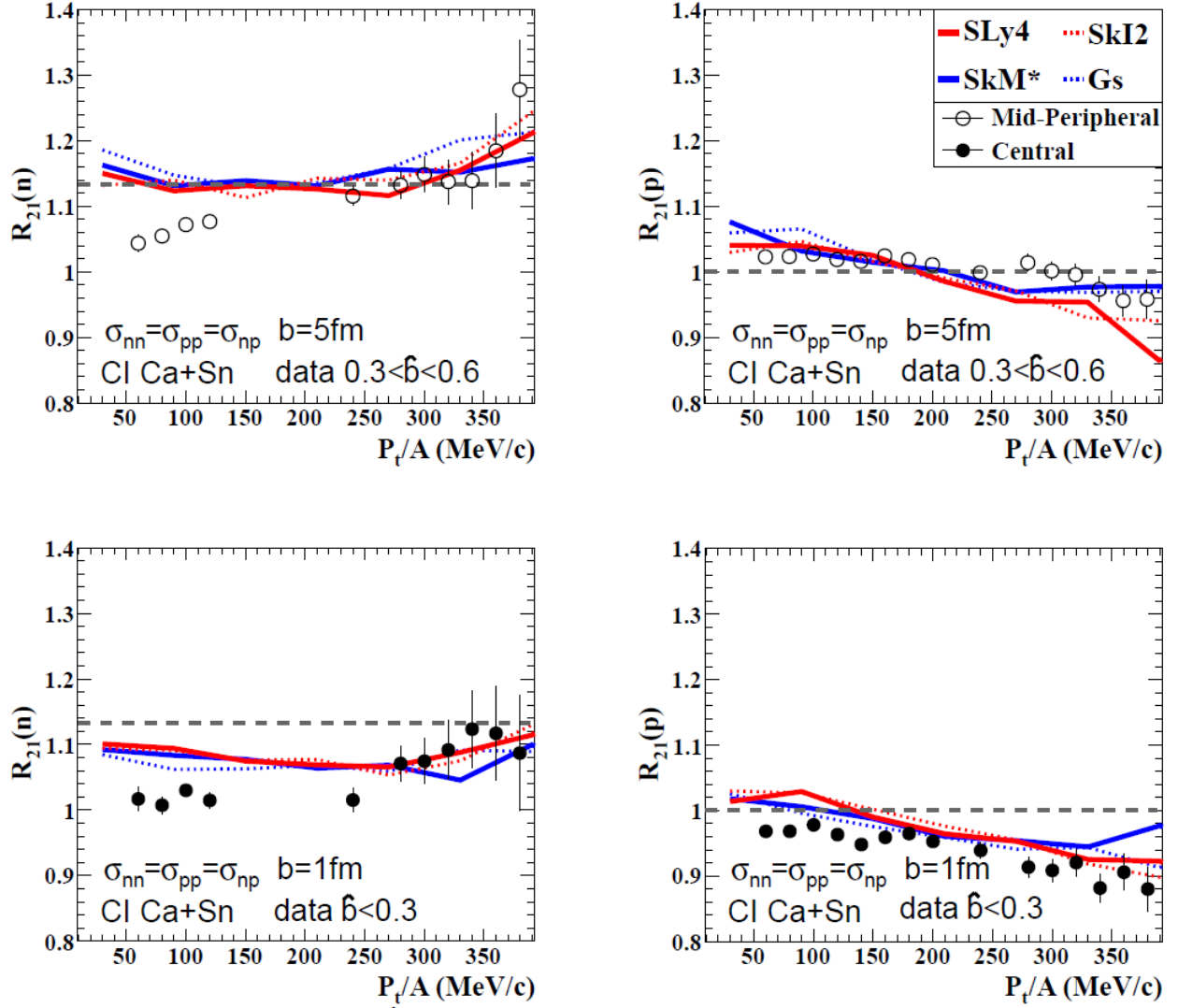
Figure 5.19: Isoscaling ratios of CI nucleons are shown as circular data points. ImQMD-Sky calculations using isospin-independent cross sections are shown as lines. Left panels: neutron isoscaling ratios, $R_{21}(n)$. Right panels: proton isoscaling ratios, $R_{21}(p)$. Upper panels: mid-peripheral collisions. Lower panels: central collisions.
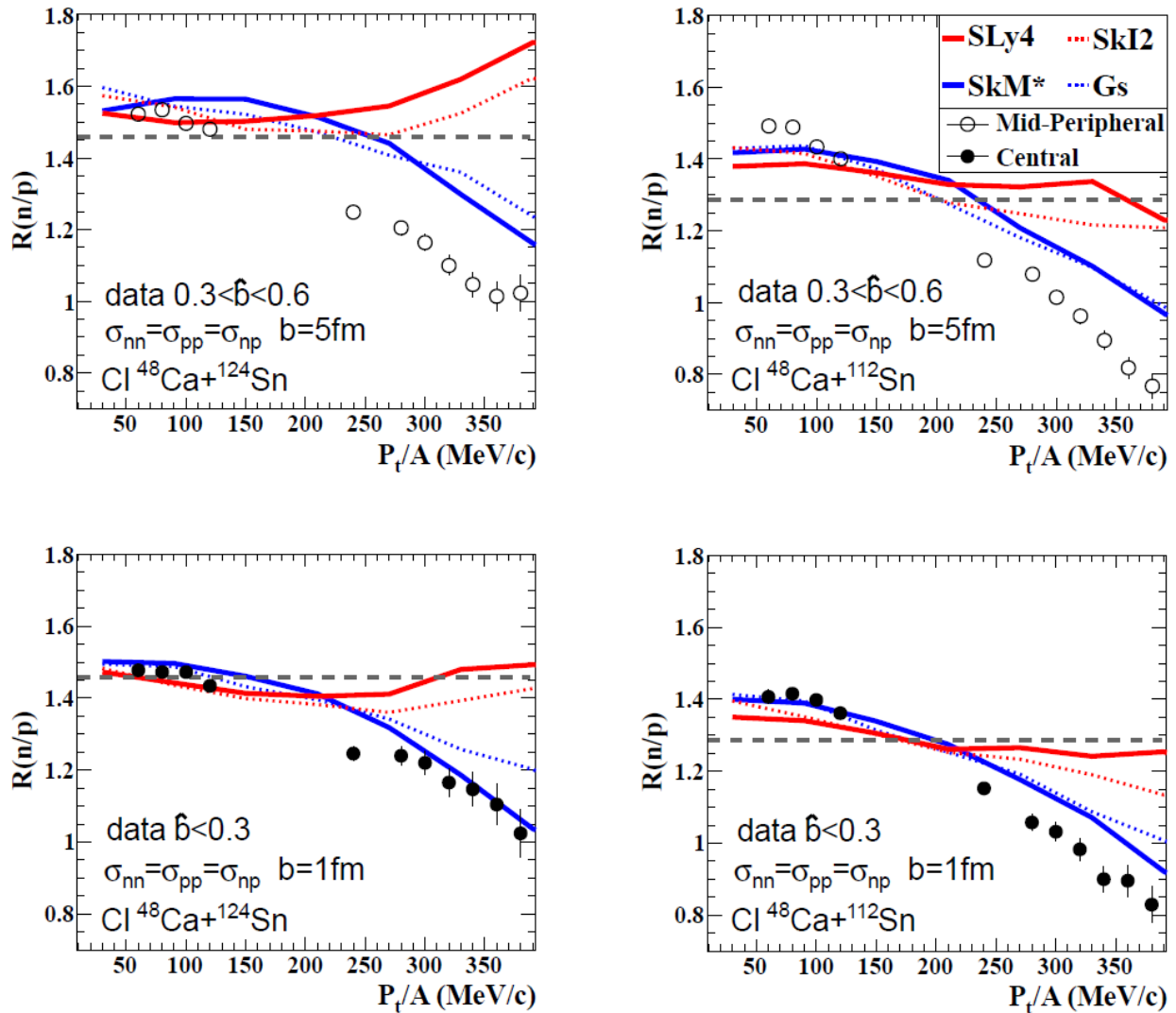
Figure 5.20: The n/p ratios from CI nucleons are shown as circular data points. ImQMD-Sky calculations using isospin-independent cross sections are shown as lines. Left panels: $R(n/p)$, for ^{48}Ca+^{124}Sn. Right panels: $R(n/p)$ for ^{48}Ca+^{112}Sn. Upper panels: mid-peripheral collisions. Lower panels: central collisions.
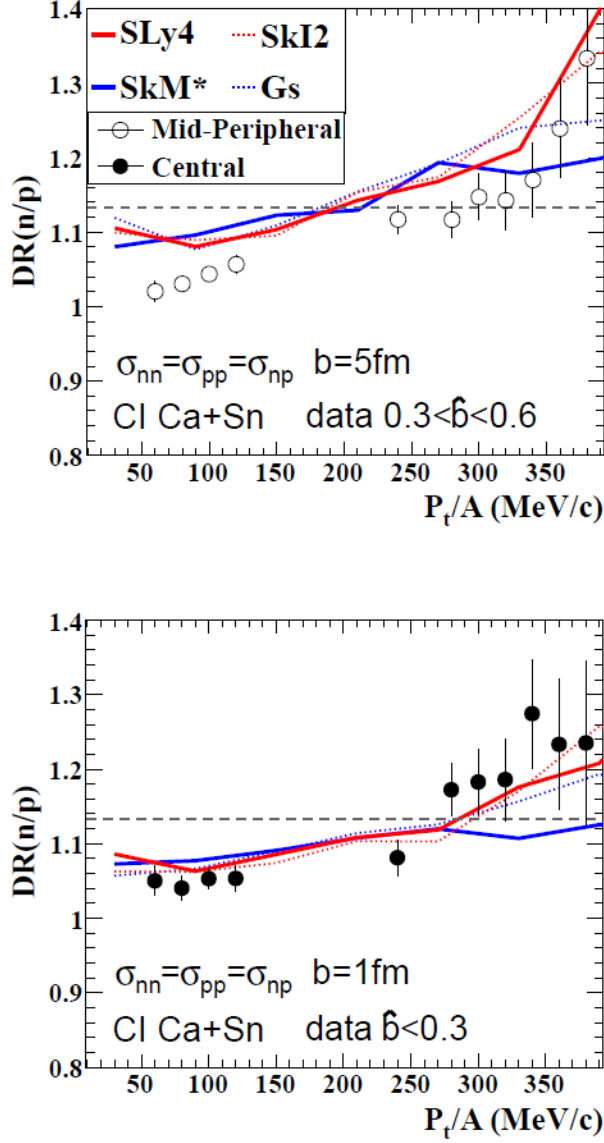
Figure 5.21: Double neutron to proton ratios, $DR(n/p)$ for Ca+Sn data. CI nucleon $DR(n/p)$ data are shown as circular data points. ImQMD-Sky calculations using isospin-independent cross sections are shown as lines. Upper panel: mid-peripheral collisions. Lower panel: central collisions.

5.7 Comparison to Symmetric Collisions

The experimental data from the companion experiment to this analysis, ^{124}Sn+^{124}Sn and ^{112}Sn+^{112}Sn at 120 AMeV as analyzed in Ref. [2] and [3], was re-examined using similar analysis cuts: spectra for all six particle species were constructed as P_t/A spectra using an analogous mid-rapidity cut from $0.40<(Y/Y_{beam})_{lab}<0.56$. These rapidity cuts are similar but not identical to the original analysis of E_{CM} spectra within $70°<\theta_{CM}<110°$. All calibrations and efficiencies are used from the original analyses, but the P_t/A spectra are constructed using the same procedure presented here for the experimental Ca+Sn at 140 AMeV data. As seen in Sections 5.3 and 5.5, the CI ratios make for the best comparison between the empirical data and the ImQMD-Sky predictions, so only Sn+Sn CI ratios are presented here. All Sn+Sn ImQMD-Sky calculations were analyzed within the same $0.45<(Y/Y_{beam})_{lab}<0.55$ mid-rapidity region as used for the Ca+Sn calculations. Only the standard isospin-dependent cross sections were used for these comparisons.

The isocaling ratios $R_{21}(n)$ and $R_{21}(p)$, where again the convention is followed that reaction 2 is the more neutron-rich reaction, ^{124}Sn+^{124}Sn, and reaction 1 is the less neutron-rich reaction, ^{112}Sn+^{112}Sn, are shown in Figure 5.22. $R_{21}(n)$ are shown in the left panels and $R_{21}(p)$ in the right panels. The empirical Sn+Sn CI $R_{21}(p)$ generally agree with the ImQMD-Sky calculations for this reaction system, although the calculations show little sensitivity to either the stiffness of the symmetry energy or the effective mass splitting, as observed for the Ca+Sn reaction calculations. The empirical Sn+Sn CI $R_{21}(n)$ lie below the calculations, but are relatively close for the central events (lower left panel).

The CI n/p ratios, as defined in Equation 1.6, are shown in Figure 5.23. The left panels show CI $R(n/p)$ for ^{124}Sn+^{124}Sn while ^{112}Sn+^{112}Sn CI data are shown in the right panels.
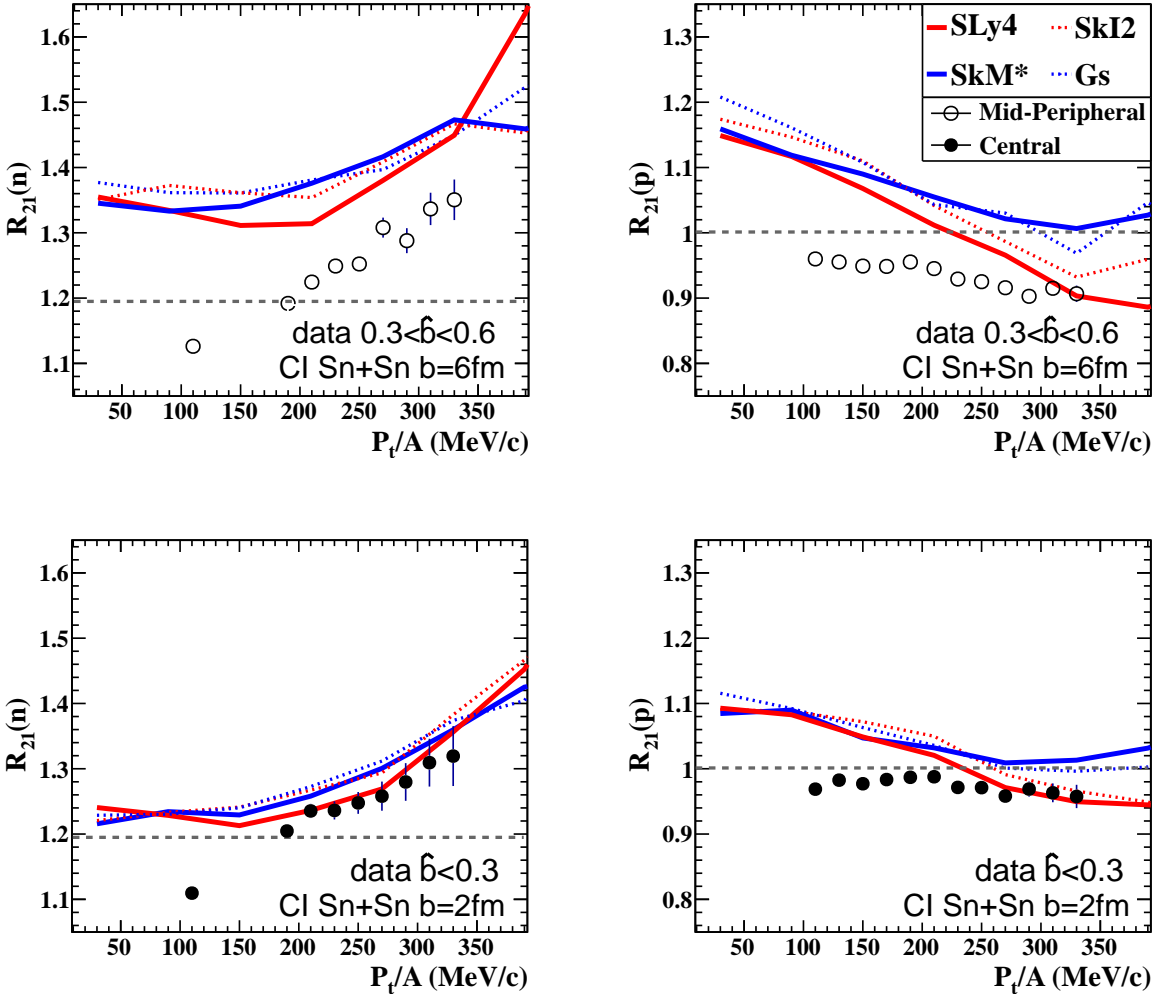
Figure 5.22: Isoscaling ratios of CI nucleons from the Sn+Sn at 120 AMeV experiment are shown as circular data points. ImQMD-Sky calculations are shown as lines. Left panels: neutron isoscaling ratios, $R_{21}(n)$. Right panels: proton isoscaling ratios, $R_{21}(p)$. Upper panels: mid-peripheral collisions. Lower panels: central collisions.
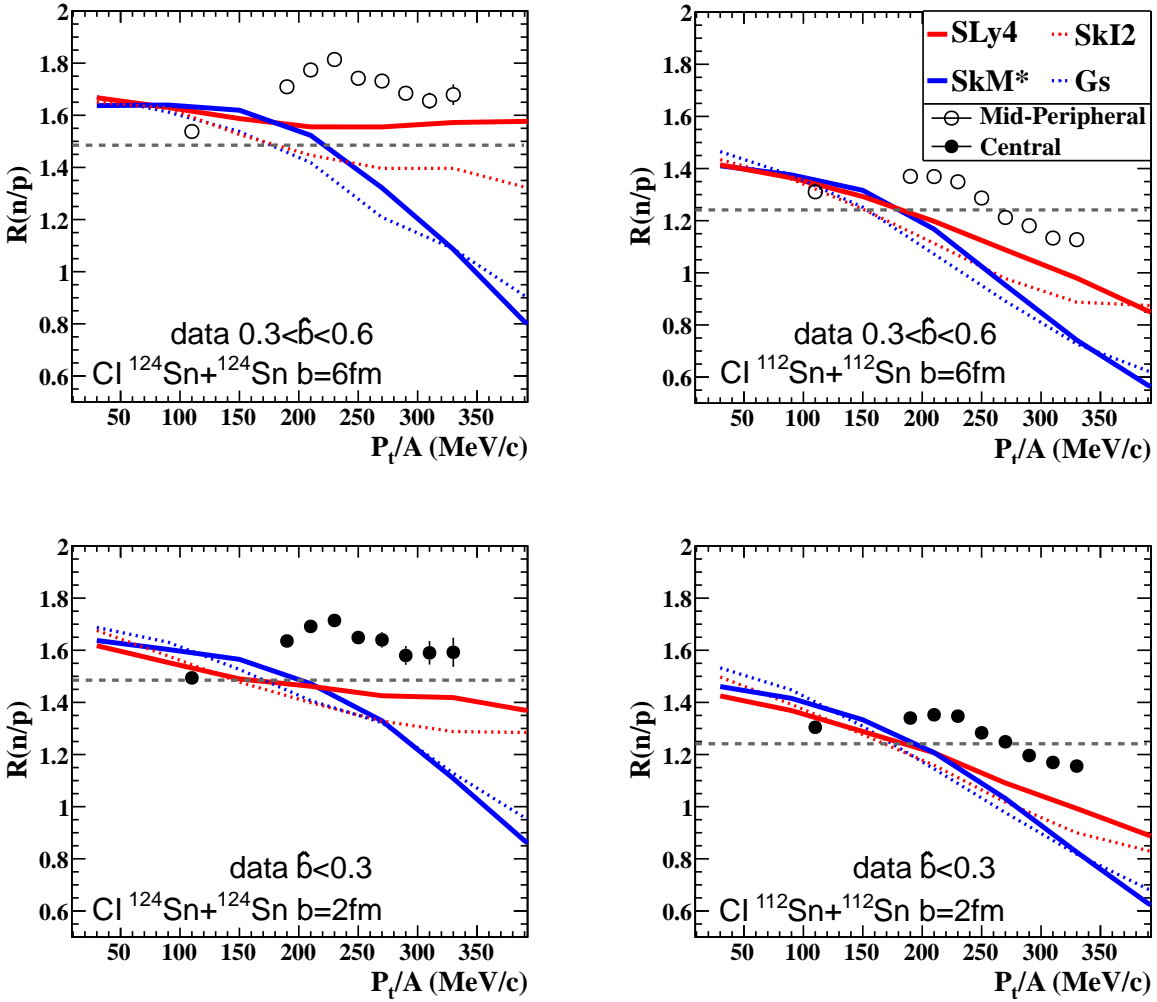
Figure 5.23: Single n/p ratios, $R(n/p)$, of CI nucleons Sn+Sn at 120 AMeV experiment are shown as circular data points. ImQMD-Sky calculations are shown as lines. Left panels: $R(n/p)$, for ^{124}Sn+^{124}Sn. Right panels: $R(n/p)$ for ^{112}Sn+^{112}Sn. Upper panels: mid-peripheral collisions. Lower panels: central collisions.

The $R(n/p)$ values are slightly lower for the ^{112}Sn+^{112}Sn reaction, which one might expect from the lower starting N/Z value of the reaction. As observed in the Ca+Sn calculations, ImQMD-Sky calculations exhibit a large sensitivity at high P_t/A to the effective mass splitting but little sensitivity at low P_t/A either to the slope of the symmetry energy, L, or to the effective mass splitting. The empirical CI $R(n/p)$ data generally lie above the ImQMD-Sky predictions especially in the range of $P_t/A{>}220$ MeV/c. At that P_t/A range, the CI $R(n/p)$ are closest to the SLy4 parameterization, which uses $m_n^* < m_p^*$ and a soft symmetry potential. This is the opposite conclusion from the Ca+Sn CI $R(n/p)$ data shown in Figure 5.17. A discussion of the possible causes of this opposite conclusion is presented later in this Section.

Finally, the Sn+Sn at 120 AMeV CI $DR(n/p)$ as defined in Equation 1.8 are shown in Figure 5.24 and again compare well to the calculations. However, as for the isoscaling ratios, there is little sensitivity within the models to either the symmetry energy strength or the effective mass splitting. As for the Ca+Sn calculations, there are large statistical errors for the predicted $DR(n/p)$, such that no Skyrme parameterization is excluded by the comparison to measured $DR(n/p)$. The original analysis found the $DR(n/p)$ to provide the best comparison between the empirical E$_{CM}$/A spectra and the ImQMD model calculations [2, 3], but it appears that within the mid-rapidity cut for P_t/A spectra, $R(n/p)$ allows for the best comparison between the empirical data and the Skyrme parameterizations.

As mentioned previously, comparing $R(n/p)$ for the empirical Ca+Sn CI data at 140 AMeV implies a better agreement with the Gs and SkM* Skyrme sets, which both use $m_n^* > m_p^*$. A similar comparison of empirical Sn+Sn CI data at 120 AMeV data to ImQMD-Sky calculations favors the Skyrme set SLy4, which uses $m_n^* < m_p^*$ and a soft symmetry potential, a conclusion that is consistent with the $DR(n/p)$ analysis of E_{CM}/A CI nucleons

156
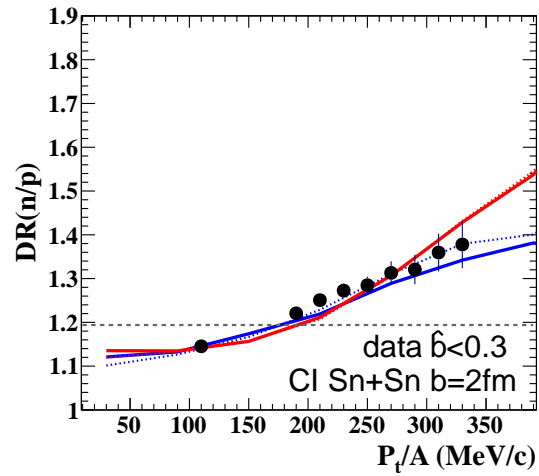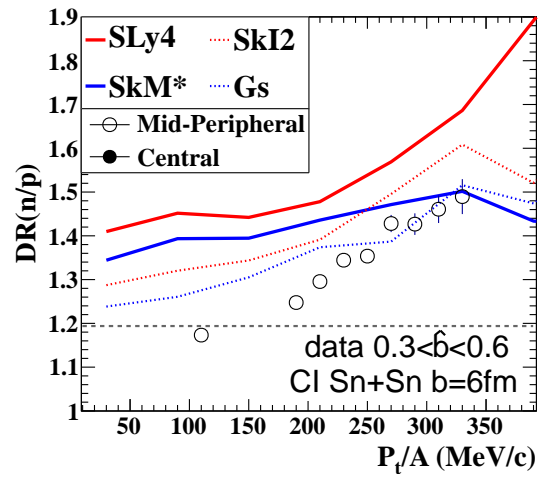
Figure 5.24: CI nucleon $DR(n/p)$ data from the Sn+Sn at 120 AMeV experiment are shown as circular data points. ImQMD-Sky calculations are shown as lines. Upper panel: mid-peripheral collisions. Lower panel: central collisions.
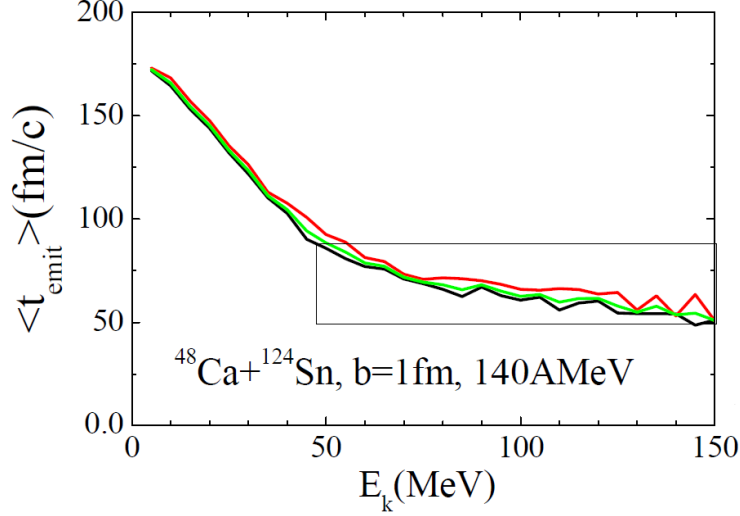
Figure 5.25: Average time of emittance for nucleons in the central (b=1 fm) ^{48}Ca+^{124}Sn reaction. Neutrons are represented by the black line, protons by the red line, and nucleons by the green line. A box is drawn around nucleons with emitted energy of E_{kin} >50 MeV to guide the eye.

but opposite to the Ca+Sn analysis presented here.

For a clue as to what may cause the discrepancy between the comparisons, nucleons that are emitted in the mid-rapidity region with E_{CM}>50 MeV (about P_t/A> 300 MeV/c) were tracked backwards through the time steps of the ImQMD-Sky calculations. For both the Ca+Sn at 140 AMeV beam energy and Sn+Sn at 120 AMeV beam energy reactions, the average time of emission for these high-energy, mid-rapidity nucleons is between 50-60 fm/c [60]; the average emission time is close to 50 fm/c for Ca+Sn and closer to 60 fm/c for Sn+Sn. The average emitted time for nucleons as a function of their final E_{CM} for the central (b=1 fm) ^{48}Ca+^{124}Sn reaction is shown in Figure 5.25.

The densities of emitted mid-rapidity nucleons were examined at the different time cuts for both Ca+Sn and Sn+Sn systems. These are effective local densities experienced by the nucleons at their time of emittance from the system [60]. The results for both Ca+Sn and Sn+Sn are shown in Figure 5.26. The mid-rapidity nucleons in the Ca+Sn reaction (upper
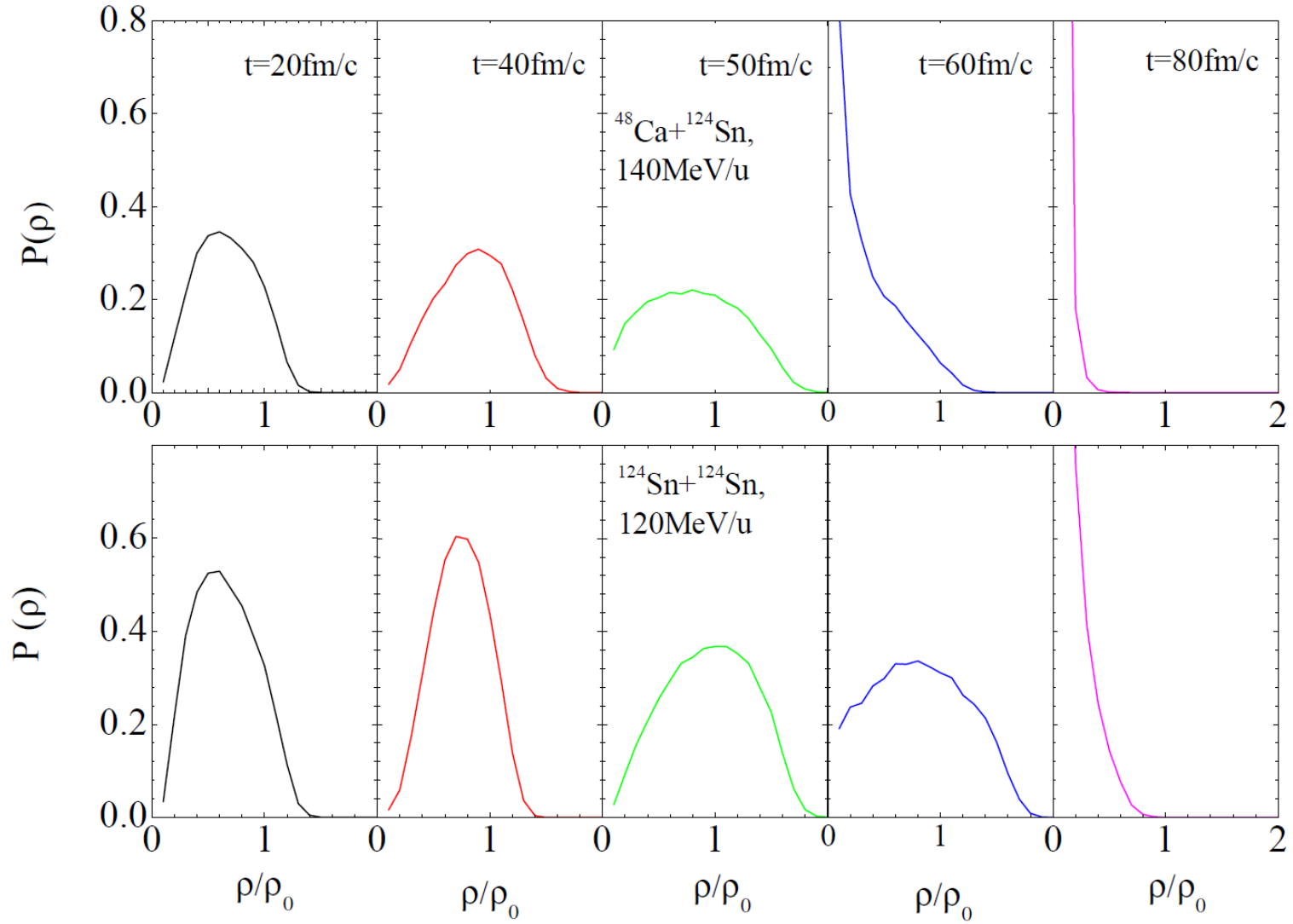
Figure 5.26: Density profiles for nucleons at different time cuts that are later emitted within the mid-rapidity cut. Upper: ^{48}Ca+^{124}Sn profiles. Lower: ^{124}Sn+^{124}Sn profiles.

panels) that are emitted near 50 fm/c come from density regions that are generally below saturation density, with an average density around $\rho/\rho_0 \approx 0.7$. The emitted mid-rapidity nucleons for the Sn+Sn reaction (lower panels) come from both the 50 fm/c and 60 fm/c time slices, so their local densities span regions that are on average just below ρ_0 but cover a wider range of densities from sub-saturation density to supra-saturation density. Just under half of the mid-rapidity nucleons emitted at t=50 fm/c in the Sn+Sn reaction come from $\rho > \rho_0$ [60].

As described in Ref. [1], the effective mass splitting could have its own density dependence. The effective mass splitting could widen with increasing density and might even "flip" at high momenta, which would lead to a "switching" in the effective mass splitting between sub- and supra-saturation densities. This effect has been observed in certain calculations, for example in a Relativistic Hartree-Fock approach in which $m_n^* > m_p^*$ at $\rho < 0.8\rho_0$ but $m_n^* < m_p^*$ for $\rho > 0.8\rho_0$ [62]. If a significant portion of an observable probes the high-density region, it could in effect be more influenced by the opposite effective mass splitting than the same observable constructed primarily from low-density data. This explanation would be consistent with the trend observed here between the observed effective mass splitting in the Ca+Sn data and the Sn+Sn data.

The ImQMD-Sky calculations used in this work allow for the effective mass splitting to increase with increasing density $\left(\frac{m}{m_n^*} - \frac{m}{m_p^*}\right) \propto \rho$, but does not include a momentum dependence, which could have an effect at play. The comparisons of experimental data analyzed here for Ca+Sn and previously for Sn+Sn suggest that a closer examination of the density and momentum dependencies of the nucleon effective mass splitting could yield interesting results.

Chapter 6

Conclusions

In this work, nucleons and light charged particles (LCPs) emitted from two reactions, ^{48}Ca+^{124}Sn and ^{48}Ca+^{112}Sn at incident energies of 140 AMeV, were analyzed and compared to predictions from transport models. The goals of the experiment were threefold: to improve the experimental constraints on the strength of the symmetry energy L, the nucleon effective mass splitting, $m_n^* \neq m_p^*$, and the in-medium nucleon cross sections σ_{NN}.

The LCPs were measured using LASSA detectors, which allowed for a precise determination of the energy, position, and isotope of the particles. The neutrons were measured in the NW Array, which provided TOF information to 1 ns that was then converted into the kinetic energy. The walls were placed far enough away from the reaction target that the angular resolution was less than 0.5°, but in order to have isotopic resolution for the neutrons, a set of scintillators was used to discriminate against charged particles.

Particle spectra were constructed in terms of the transverse momentum, P_t/A, to maximize the overlap of the LASSA and NW Array in the analysis. Charged particle multiplicities from the Miniball Array were used to select both central ($\hat{b}$<0.3) and mid-peripheral (0.3<$\hat{b}$<0.6) events. Only particles within a mid-rapidity cut, 0.44<$(Y/Y_{beam})_{lab}$<0.59 were analyzed, as ImQMD-Sky calculations predict the mid-rapidity region to correspond to the most overlap between the beam and target nuclei. The spectra were constructed as written in Equation 5.1.

Both free and coalescence invariant (CI) spectra were constructed; CI nucleons are often

used to compare between the experimental and calculation results because they allow for a more similar comparison, as the transport models have difficulty reproducing binding energies of fragments, leading to an overprediction of free nucleons and an underprediction of light fragments. By breaking up LCPs into their constituent nucleons in the analysis, this problem is minimized. For this work, ImQMD-Sky calculations were performed with four different Skyrme sets (Gs, SkI2, SLy4, and SkM*) that together include both soft (L=46 MeV) and stiff (L>90 MeV) symmetry strengths and both $m_n^* < m_p^*$ and $m_n^* > m_p^*$ effective mass splittings. The calculations were performed with standard isospin-dependent σ_{NN} derived from empirical free cross sections and repeated for isospin-independent σ_{NN} calculated as the weighted average of free cross sections.

For all sets of calculations, only one ratio constructed with free or CI nucleons showed sensitivity to L: the free $R(n/p)$ at low P_t/A. This momentum domain is where the experimental data do not compare well to calculations, partly due to a higher proportion of competing effects such as Coulomb effects and sequential decays. Only $R(n/p)$ at high P_t/A, for both free and CI nucleons, demonstrated a clear sensitivity either to the effective mass splitting or to the form of the in-medium cross sections employed by the calculations. The high-momentum $R(n/p)$ were therefore the best foundation to compare between empirical yields and ImQMD-Sky predictions. Although the calculated $R_{21}(n)$, $R_{21}(p)$, and $DR(n/p)$ did not demonstrate a sensitivity to any of the varied parameters in this analysis, the empirical data agreed well with the predictions, both the shape of the trends and the values, which instilled a confidence that the ImQMD-Sky calculations model the analyzed systems well. Likewise, even though the low P_t/A region of the CI $R(n/p)$ did not show sensitivity in the calculations to the Skyrme parameter set used, the empirical values lined up well with those predicted by the transport model.

At the high momentum region, around $P_t/A > 300$ MeV/c, the measured free and CI nucleons agreed better in both shape and value with the effective mass splitting $m_n^* > m_p^*$; this comparison holds for both reactions and both centrality cuts. When σ_{NN} were varied from the default isospin-dependent to the isospin-independent case, the calculated n/p ratios did not agree as well with the empirical CI nucleons except for the central ^{48}Ca+^{124}Sn $R(n/p)$. On the whole, the data better support the isospin-dependent forms of σ_{NN}.

The conclusion in this work, that calculations following $m_n^* > m_p^*$ better describe the measured CI nucleons, is opposite that found from the companion experiment examining ^{124}Sn+^{124}Sn and ^{112}Sn+^{112}Sn at incident energies of 120 AMeV, which found agreement with calculations using $m_n^* < m_p^*$ [2]. As that experimental analysis originally constructed free and CI spectra in terms of E_{CM}/A, the measured and simulated particles were reanalyzed in this work in terms of P_t/A. The new analysis for Sn+Sn data continues to support the calculations using $m_n^* < m_p^*$. The CI $R_{21}(x)$ and $DR(n/p)$ of P_t/A spectra from the previous Sn+Sn experiment also described the measured trends of the data well, while those ratios displayed different trends for the E_{CM}/A analysis [3]. It appears that P_t/A allows for a better matchup between experimental and calculated particles with this set of data. E_{CM}/A is generally believed to be a more robust observable within the calculations, since ImQMD-Sky simulates the colliding beam and target nuclei in the center of mass frame. However, since both the E_{CM}/A and P_t/A spectra for the Sn+Sn collisions agree with $m_n^* < m_p^*$, it appears that the disagreement with the conclusion from the Ca+Sn experiment lies not within the observable chosen but in the different physics between the two experiments.

It seems curious that the ImQMD-Sky calculations show a greater sensitivity to the effective mass splitting $m_n^* \neq m_p^*$ within $DR(n/p)$ constructed with E_{cm}/A spectra but $R(n/p)$ constructed with P_t/A spectra. Since this pattern was observed for both the symmetric

system (Sn+Sn) as well as the asymmetric system (Ca+Sn), it is possibly related to select-ing the beam-target overlap using $(Y/Y_{beam})_{lab} \sim 0.5$ analysis cut rather than a transverse $70° < \theta_{cm} < 110°$ cut. The two analysis cuts are quite similar for symmetric reactions: the θ_{cm} selection allows for the inclusion of more data at higher energies, creating a "triangular" cut in P_t/A or E_t/A vs. $(Y/Y_{beam})_{lab}$, while a $(Y/Y_{beam})_{lab}$ cut selects a more "rectangular" region in the same plot.

It is not surprising that the ImQMD-Sky calculations of Ca+Sn $R(n/p)$ showed only 5-20% sensitivity to the form of σ_{NN} used. Both the isospin-dependent and isospin-independent cases employed the same scaling from measured free cross sections, which was previously found to describe in-medium effects well [56]. It is reasonable that $R_{21}(x)$ would change little from one form of σ_{NN} to another, since the spectra from both reactions would be simi-larly affected by the change in the cross section; this limited effect applies to the $DR(n/p)$ as it is constructed from both $R_{21}(n)$ and $R_{21}(p)$. The largest sensitivity to σ_{NN} was expected to be displayed in the n/p ratios, since the initial N, Z, and N/Z compositions were very different for the beam and target nuclei; the expected sensitivity was shown in the calculated ratios. The empirical results agreed better with the isospin-dependent forms used.

6.1   Outlook

It would be interesting to study the ^{40}Ca+^{124}Sn and ^{40}Ca+^{112}Sn reactions as originally planned for the experiment. Ratios constructed using those reactions could be more sen-sitive to the form of σ_{NN} used in the calculation. This is especially true of ^{40}Ca+^{124}Sn which has the largest difference in isospin asymmetry between the beam (δ=0) and target (δ=1.48). The wider asymmetry difference probed using the ^{40}Ca beam could also poten-

tially increase the sensitivity to L within the constructed ratios. Based on the encouraging results from ^{48}Ca+Sn reactions examined in this work, experiments with a ^{40}Ca beam or other asymmetric reactions may be performed in the future for a greater constraint on σ_{NN}.

On the theory side, it may prove fruitful to examine different forms of the dependence on density in the effective mass splitting or to include a momentum-dependence. At present, the ImQMD-Sky approach varies the effective masses as $\left(\frac{m}{m_n^*} - \frac{m}{m_p^*}\right) \propto \rho$. Other studies suggest that the splitting may "switch" at high density. Further, a momentum dependence may be in effect, which could manifest in the different effects observed in this analysis for the asymmetric Ca+Sn reaction ($m_n^* > m_p^*$) and the symmetric Sn+Sn reaction ($m_n^* < m_p^*$).

It is curious that P_t/A ratios show the greatest sensitivity within $R(n/p)$ and the E_{CM}/A ratios demonstrated the greatest sensitivity in $DR(n/p)$. The mechanism behind this result could be examined by comparing the P_t/A and E_{CM}/A of calculated nucleons and LCPs. An in-depth examination of the analysis cuts may yield interesting results: perhaps the mid-rapidity cut used in this analysis to select the overlap region in the asymmetric reactions selects nucleons with fundamental differences from the transverse θ_{CM} cut typically used in symmetric reactions. It may be interesting to compare the density and momentum profiles of nucleons emitted within the two cuts.

In order to further constrain the symmetry energy, it may be necessary to examine the emission particles at suprasaturation density. Experiments of this type are planned using radioactive beams at the Radioactive Isotope Beam Factory (RIBF) and the Facility for Rare Isotope Beams (FRIB). It is predicted that charged pion ratios will demonstrate a high sensitivity to the density-dependence of the symmetry energy used in transport model calculations, which in turn will require a strong constraint on the nucleon effective masses.

BIBLIOGRAPHY

BIBLIOGRAPHY

[1] Yingxun Zhang, M.B. Tsang, Zhuxia Li, and Hang Liu. Constraints on nucleon effective mass splitting with heavy ion collisions. *Phys. Lett. B*, 732:186–190, 2014.

[2] Daniel David Schechtman Coupland. *Probing The Nuclear Symmetry Energy With Heavy Ion Collisions*. Ph.D. thesis, Michigan State University, 2013.

[3] Michael David Youngs. *Using Light Emitted Clusters as a Probe of the Symmetry Energy in the Nuclear Equation of State*. Ph.D. thesis, Michigan State University, 2013.

[4] Philip David Zecher. *Design Construction and Use of the Neutron Wall Array in Measuring the $^{8}Li(n\ \gamma)^{9}Li$ Astrophysics Reaction*. Ph.D. thesis, Michigan State University, 1996.

[5] P. D. Zecher. A large-area, position-sensitive neutron detector with neutron gamma-ray discrimination capabilities. *Nucl. Inst. Methods*, 401:329–344, 1997.

[6] E. Rutherford. Retardation of the alpha particle from radium in passing through matter. *Philosophical Magazine*, 12:134–146, 1906.

[7] J. Chadwick. The existence of a neutron. *Proc. Roy. Soc. A*, 136:692–708, 1932.

[8] W. Heisenberg. *Über den bau der atomkerne. *Zeitschr. f. Phys.*, 77:1–11, 1932.

[9] H. Yukawa. On the interaction of elementary particles. *Proc. Phys. Math. Soc. Japan*, 17, 1935.

[10] M. G. Mayer. On closed shells in nuclei. *Phys. Rev.*, 74:235–239, 1948.

[11] Otto Haxel, J. Hans D. Jensen, and Hans E. Suess. On the 'magic numbers' in nuclear structure. *Phys. Rev.*, 75:1766, 1949.

[12] M. Gell-Mann. A schematic model of baryons and mesons. *Phys. Let.*, 8:214–215, 1964.

[13] G. Zweig. An su3 model for strong interaction symmetry and its breaking. *CERN-TH*, 401, 1964.

[14] The Nuclear Science Advisory Committee. The frontiers of nuclear science: A long range plan. 2007.

[15] A.W. Steiner, M. Prakash, J.M. Lattimer, and P.J. Ellis. Isospin asymmetry in nuclei and neutron stars. *Physics Reports*, 411:325–375, 2005.

[16] James M. Lattimer. The nuclear equation of state and neutron star masses. *Annual Review of Nuclear and Particle Science*, 62:485–515, 2012.

[17] M. Lattimer and M. Prakash. Neutron star structure and the equation of state. *ApJ*, 550:426–442, March 2001.

[18] M. Gearheart, W.G. Newton, J. Hooker, and Bao-An Li. Upper limits on the observational effects of nuclear pasta in neutron stars. *Mon. Not. R. Astron. Soc.*, 418, 2011.

[19] Hans-Thomas Janka. Explosion mechanisms of core-collapse supernovae. *Annual Review of Nuclear and Particle Science*, 62:407–451, 2012.

[20] C. J. Horowitz, E. F. Brown, Y. Kim, W.G. Lynch, R. Michaels, A. Ono, J. Piekarewicz, M.B. Tsang, and H. H. Wolter. A way forward in the study of the symmetry energy: experiment, theory, and observation. *ArXiv:nucl-th*, 1401:5839, 2014.

[21] S. Typel and B. Alex Brown. Neutron radii and the neutron equation of state in relativistic models. *Phys. Rev. C*, 64:027302, Jun 2001.

[22] C. J. Horowitz and J. Piekarewicz. Neutron star structure and the neutron radius of ^{208}pb. *Phys. Rev. Lett.*, 86:5647–5650, Jun 2001.

[23] Lie-Wen Chen, Che Ming Ko, Bao-An Li, and Jun Xu. Density slope of the nuclear symmetry energy from the neutron skin thickness of heavy nuclei. *Phys. Rev. C*, 82:024321, Aug 2010.

[24] Luca Trippa, Gianluca Coló, and Enrico Vigezzi. Giant dipole resonance as aquantitative constraint on the symmetry energy. *Phys. Rev. C*, 77:061304, Jun 2008.

[25] A. Klimkiewicz, N. Paar, P. Adrich, M. Fallot, K. Boretzky, T. Aumann, D. Cortina-Gil, U. Datta Pramanik, Th.W. Elze, H. Emling, H. Geissel, M. Hellström, K. L. Jones, J. V. Kratz, R. Kulessa, C. Nociforo, R. Palit, H. Simon, G. Surówka, K. Sümmerer, D. Vretenar, and W. Walús. Nuclear symmetry energy and neutron skins derived from pygmy dipole resonances. *Phys. Rev. C*, 76:051603, Nov 2007.

[26] Andrea Carbone, Gianluca Coló, Angela Bracco, Li-Gang Cao, Pier Francesco Bortignon, Franco Camera, and Oliver Wieland. Constraints on the symmetry energy and neutron skins from pygmy resonances in ^{68}ni and ^{132}sn. *Phys. Rev. C*, 81:041301, Apr 2010.

[27] Horst Müller and Brian D. Serot. Phase transitions in warm, asymmetric nuclear matter. *Phys. Rev. C*, 52:2072–2091, Oct 1995.

[28] H. S. Xu, M. B. Tsang, T. X. Liu, X. D. Liu, W. G. Lynch, W. P. Tan, A. van der Molen, G. Verde, A. Wagner, H. F. Xi, C. K. Gelbke, L. Beaulieu, B. Davin, Y. Larochelle, T. Lefort, R. T. de Souza, R. Yanez, V. E. Viola, R. J. Charity, and L. G. Sobotka. Isospin fractionation in nuclear multifragmentation. *Phys. Rev. Lett.*, 85:716–719, Jul 2000.

[29] Jianmin Dong, Wei Zuo, and Jianzhong Gu. Origin of symmetry energy in finite nuclei and density dependence of nuclear matter symmetry energy from measured alpha-decay energies. *Phys. Rev. C*, 87:014303, 2013.

[30] M. A. Famiano, T. Liu, W. G. Lynch, M. Mocko, A. M. Rogers, M. B. Tsang, M. S.Wallace, R. J. Charity, S. Komarov, D. G. Sarantites, L. G. Sobotka, and G. Verde. Neutron and proton transverse emission ratio measurements and the density dependence of the asymmetry term of the nuclear equation of state. *Phys. Rev. Lett.*, 97:052701, Aug 2006.

[31] T. X. Liu, W. G. Lynch, M. B. Tsang, X. D. Liu, R. Shomin, W. P. Tan, G. Verde, A. Wagner, H. F. Xi, H. S. Xu, B. Davin, Y. Larochelle, R. T. de Souza, R. J. Charity, and L. G. Sobotka. Isospin diffusion observables in heavy-ion reactions. *Phys. Rev. C*, 76:034603, Sep 2007.

[32] S. R. Souza, M. B. Tsang, R. Donangelo, W. G. Lynch, and A. W. Steiner. Probing the symmetry energy from the nuclear isoscaling. *Phys. Rev. C*, 78:014605, Jul 2008.

[33] M. B. Tsang, C. K. Gelbke, X. D. Liu, W. G. Lynch, W. P. Tan, G. Verde, H. S. Xu, W. A. Friedman, R. Donangelo, S. R. Souza, C. B. Das, S. Das Gupta, and D. Zhabinsky. Isoscaling in statistical models. *Phys. Rev. C*, 64:054615, Oct 2001.

[34] M. B. Tsang and et.al. Isospin diffusion and the nuclear symmetry energy in heavy ion reactions. *Phys. Rev. Lett.*, 92:062701, 2004.

[35] Bao-An Li. Probing the high density behavior of the nuclear symmetry energy with high energy heavy-ion collisions. *Phys. Rev. Lett.*, 88:192701, Apr 2002.

[36] J. Aichelin. Quantum molecular dynamics. *Physics Reports*, 202:233–360, 1991.

[37] Z.Y. Sun et al. Isospin diffusion and equilibration for sn + sn collisions at e/a = 35 mev. *Phys. Rev. C*, 82:051603, 2010.

[38] Pavel Danielewicz. Determination of the mean-field momentum-dependence using elliptic flow. *Nuc. Phys. A*, 673:375, 2000.

[39] M Begemann-Blaich, WFJ M*ü*ller, and et al. Qmd simulation of multifragment production in heavy ion collisions at e/a= 600 mev. *Prog. Part. Nucl. Phys.*, 30:181–183, 1993.

[40] Yingxun Zhang, Pavel Danielewicz, Michael Famiano, Zhuxia Li, W.G. Lynch, and M.B. Tsang. The influence of cluster emission and the symmetry energy on neutron-proton spectral double ratios. *Phys. Lett. B*, 664:145–148, 2008.

[41] Ch. Hartnack and et al. Modelling the many-body dynamics of heavy ion collisions: Present status and future perspective. *ArXiv:nucl-th/9811015*, 1998.

[42] Japan Atomic Energy Agency. Particle and heavy ion transport code system. online, 2007. http://phits.jaea.go.jp/Overview.html.

[43] Norihiro Matsuda, Yosuke Iwamoto, Hiroshi Iwase, Yukio Sakamoto, Hiroshi Nakashima, and Koji Niitas. Benchmarking of phits on pion production for medium-energy physics. *Prog. in Nuc. Sci. and Tech*, 2:927–930, 2011.

[44] Daiki Satoh, Tatsuhiko Sato, Nobuhiro Shigyo, and Kenji Ishibashi. Scinful-qmd: Monte carlo based computer code to calculate response function and detection efficiency of a liquid organic scintillator for neutron energies up to 3 gev. *JAEA-Data/Code 2006-023*, Nov 2006.

[45] D.D.S. Coupland, M. Youngs, Z. Chajecki, W.G. Lynch, M.B. Tsang, Y.X. Zhang, M.A. Famiano, T.K. Ghosh, B. Giacherio, M.A. Kilburn, Jenny Lee, F. Lu, P. Russotto, A. Sanetullaev, R.H. Showalter, G. Verde, and J. Winkelbauer. Effective nucleon masses in compressed and expanding neutron-rich matter. *Science [in review]*, 2014.

[46] Lie-Wen Chen, Che Ming Ko, and Bao-An Li. Effects of momentum-dependent nuclear potential on two-nucleon correlation functions and light cluster production in intermediate energy heavy-ion collisions. *Phys. Rev. C*, 69:054606, Aug 2004.

[47] G. L Engel, M. Sadasivam, M. Nethi, J. M. Elson, L. G. Sobotka, and R. J. Charity. A multi-channel integrated circuit for use in low- and intermediate-energy nuclear

physics. *Nuclear Instruments and Methods in Physics Research Section A: Accelerators, Spectrometers, Detectors and Associated Equipment*, 573:418–426, 2007.

[48] Dave Sanderson. Private communication, 2009.

[49] O. B. Tarasov and D. Bazin. Radioactive beam production with in-flight separators. *Nuclear Instruments and Methods in Physics Research Section B: Beam Interactions with Materials and Atoms*, 266:4657–4664, 2008.

[50] Tianxiao Liu. *Isospin Dynamics and the Isospin Dependent EOS*. Ph.D. thesis, Michigan State University, 2005.

[51] Yingxun Zhang and Zhuxia Li. Elliptic flow and system size dependence of transition energies at intermediate energies. *Phys. Rev. C*, 74:014602, 2006.

[52] Isaac Vidaña, Constança Providência, Artur Polls, and Arnau Rios. Density dependence of the nuclear symmetry energy: A microscopic perspective. *Phys. Rev. C*, 80:045806, 2009.

[53] M. Dutra, O. Lourenço, J. S. Sá Martins, A. Delfino, J. R. Stone, and P. D. Stevenson. Skyrme interaction and nuclear matter constraints. *Phys. Rev. C*, 85:035201, 2012.

[54] K.A. Brueckner. Two-body forces and nuclear saturation. iii. details of the structure of the nucleus. *Phys. Rev.*, 97:1353–1366, Mar 1955.

[55] G.E. Brown, J.H. Gunn, and P. Gould. Effective mass in nuclei. *Nuclear Physics*, 46:598–606, 1963.

[56] Yingxun Zhang, DDS Coupland, Pavel Danielewicz, Zhuxia Li, Hang Liu, Fei Lu, W.G. Lynch, and M.B. Tsang. Influence of in-medium nn cross sections, symmetry potential, and impact parameter on isospin observables. *Phys. Rev. C*, 85:024602, 2012.

[57] J. Cugnon, D. L'Hôte, and J. Vandermeulen. Simple parametrization of cross-sections for nuclear transport studies up to the gev range. *Nucl. Inst. and Meth. in Phys. Res. B*, 111:215–220, 1996.

[58] Qianghua Wu, Yingxun Zhang, Zhuxia Li, Zhigang Xiao, Rensheng Wang, Ning Wang, and R. H. Showalter. Competition between coulomb and symmetry potential in semi-peripheral heavy ion collisions. *Phys. Rev. C*, 2015.

[59] T. X. Liu, W. G. Lynch, R. H. Showalter, M. B. Tsang, X. D. Liu, W. P. Tan, M. J. van Goethem, G. Verde, A. Wagner, H. F. Xi, H. S. Xu, M. A. Famiano, R. T. de Souza, V. E. Viola, R. J. Charity, and L. G. Sobotka. Isospin observables from fragment energy spectra. *Phys. Rev. C*, 86:024605, 2012.

[60] Y.X. Zhang. Private communication, 2014.

[61] Yingxun Zhang, M.B. Tsang, and Zhuxia Li. Sensitivity of skyrme interaction to hic observables. *[Preprint]*, 2015.

[62] Wen-Hui Long, Nguyen Van Giai, and Jie Meng. Density-dependent relativistic hartree-fock approach. *Phys. Lett. B*, 640:150–154, 2006.